

FABRICATION AND CHARACTERIZATION OF CARBON AND BORON
CARBIDE NANOSTRUCTURED MATERIALS

by

SARA REYNAUD

A dissertation submitted to the

Graduate School-New Brunswick

Rutgers, The State University of New Jersey

in partial fulfillment of the requirements

for the degree of

Doctor of Philosophy

Graduate Program in Materials Science and Engineering

written under the direction of

Professor Manish Chhowalla

and approved by

New Brunswick, New Jersey

October, 2010

ABSTRACT OF THE DISSERTATION

Fabrication and Characterization of Carbon and Boron Carbide Nanostructured Materials

By SARA REYNAUD

Dissertation Director: Professor Manish Chhowalla

Carbon is present in nature in a variety of allotropes and chemical compounds. Due to reduced dimensionality, nanostructured carbon materials, i.e. single walled carbon nanotubes (SWNTs), are characterized by unique physical and chemical properties. There is a potential for SWNTs use as biological probes and assists for tunable tissue growth in biomedical applications. However, the presumed cytotoxicity of SWNTs requires investigation of the risks of their incorporation into living systems.

Boron is not found in nature in elementary form. Boron based materials are chemically complex and exist in various polymorphic forms, i.e. boron carbide (BC). Because BC is a lightweight material with exceptional mechanical and elastic properties, it is the ideal candidate for armor and ballistic applications. However, practical use of BC as armor material is limited because of its anomalous glass-like behaviour at high velocity impacts, which has been linked to stress-induced structural instability in one of

BC polymorphs, B12(CCC). Theoretical calculations suggest that formation of B12(CCC) in BC could be suppressed by silicon doping.

In the first part of this thesis, biocompatibility of SWNTs is investigated. It is shown that under normal cell implantation conditions, the electrical conductivity of the SWNTs decreases due to an increase in structural disorder. This research suggests that SWNTs can be functionalized by protein and biological cells reducing the risk of cytotoxicity.

In the second part of this thesis, boron carbide nanostructured materials are synthesized and investigated. Radio frequency sputtering deposition technique is employed for fabrication of BC (Si free) and BC:Si thin films. Variation of plasma conditions and temperature are found to affect chemical composition, adhesion to the substrate and morphology of the films. It is shown that BC films are predominantly amorphous and a small addition of Si largely improves their mechanical properties. In addition, nanostructured BC compounds are fabricated by arc discharge technique using graphite or boron carbide electrodes submerged in liquid nitrogen, de-ionised water, or argon gas. Microscopic and spectroscopic investigation of the synthesized material confirms formation of various BC and carbon nanostructures. Specifically, arc discharge initiated in inert environment by applying low current leads to the formation of nanostructured BC without contaminants.

ACKNOWLEDGEMENTS

I am very thankful to my advisor, Professor Manish Chhowalla, for his teaching, support and encouragement during the three years of my Ph.D. studies. I am obliged to the Army Research Office and the National Science Foundation for providing financial support for this research. I also thank Professor Albano Cavaleiro of the University of Coimbra and Professor Ahmet Avci of Selçuk University, with whom I collaborated on magnetron sputtering and arc discharge experiments.

I am particularly grateful to my colleague Wojtek Tutak for giving me an opportunity to participate in his research project. I would also like to thank Dr. Steve Miller for all the time he spent with me over the TEM, Dr. Vladyslav Domnich for the insightful discussions on Raman spectroscopy and boron carbide, and Dr. Hisato Yamaguchi for many useful suggestions.

I would like to dedicate this thesis to my family. Their energy, love and support were very important to me during the last three years. This period was full of joy and happiness for the birth of my two girls and for sharing life with my loved ones.

TABLE OF CONTENTS

| | |
|---|------|
| ABSTRACT OF DISSERTATION..... | ii |
| ACKNOWLEDGEMENTS | iv |
| TABLE OF CONTENTS..... | v |
| LIST OF TABLES..... | viii |
| LIST OF FIGURES..... | ix |
| CHAPTER 1..... | 1 |
| STRUCTURE AND PROPERTIES OF SINGLE-WALLED CARBON NANOTUBES (SWNTs) | |
| 1.1 Atomic bonding and structure of SWNTs..... | 1 |
| 1.2 Electronic and optical properties of SWNTs..... | 5 |
| 1.3 Phonon structure and vibrational properties of SWNTs..... | 11 |
| 1.4 Mechanical properties of SWNTs..... | 14 |
| 1.5 Thermal properties of SWNTs..... | 16 |
| 1.6 Chemical properties and biocompatibility of SWNTs..... | 17 |
| CHAPTER 2..... | 22 |
| DEGRADATION OF SINGLE-WALLED CARBON NANOTUBES STRUCTURE BY LIVING OSTEOBLAST CELLS IN BIO-IMPLANTATION | |
| 2.1 Motivation and research outline..... | 22 |
| 2.2 Experimental approach..... | 23 |
| 2.3 Results and discussion..... | 27 |

| | |
|---|-----|
| CHAPTER 3..... | 38 |
| STRUCTURE AND PROPERTIES OF BORON CARBIDE | |
| 3.1 Boron carbide atomic structure and phase diagram..... | 38 |
| 3.2 Structural polytypism in boron carbide..... | 40 |
| 3.3 Vibrational properties of boron carbide and graphitic carbon..... | 42 |
| 3.4 Electronic and optical properties of boron carbide..... | 48 |
| 3.5 Mechanical and ballistic properties of boron carbide..... | 54 |
| CHAPTER 4..... | 65 |
| FABRICATION OF THIN FILMS USING MAGNETRON SPUTTERING | |
| 4.1 Vacuum science and impact on films properties..... | 65 |
| 4.2 Sputtering deposition technique..... | 70 |
| 4.3 Sputtering configurations..... | 73 |
| 4.4 Experimental goals and research outline..... | 76 |
| 4.5 Results and discussion..... | 78 |
| CHAPTER 5..... | 98 |
| SYNTHESIS OF NANOSTRUCTURES USING ARC DISCHARGE | |
| 5.1 Theory of the electric arc | 98 |
| 5.2 The arc discharge technique..... | 101 |
| 5.3 Arc between graphite electrodes..... | 105 |
| 5.4 Arc between substances other than carbon..... | 107 |
| 5.5 Experimental goals and outline..... | 109 |
| 5.6 Results and discussion..... | 111 |

| | |
|-----------------------------|-----|
| CHAPTER 6..... | 118 |
| CONCLUSIONS AND FUTURE WORK | |
| REFERENCES..... | 121 |
| CURRICULUM VITAE..... | 134 |

LIST OF TABLES

| | |
|---|----|
| Table 1.1. Mechanical properties of carbon nanotubes nanotubes [31] | 15 |
| Table 3.1. Mechanical properties of boron carbide [125]..... | 54 |

LIST OF FIGURES

| | |
|---|----|
| Figure 1.1..... | 2 |
| Bonding between carbon atoms: (a) sp^3 , (b) sp^2 , and (c) sp -hybridized orbitals. | |
| Figure 1.2..... | 2 |
| Arrangement of carbon atoms in (a) diamond, (b) graphite, and (c) nanotube structure. | |
| Figure 1.3..... | 3 |
| A nanotube (n,m) is formed by rolling a graphite sheet along the chiral vector $\mathbf{C} = n\mathbf{a}_1 + m\mathbf{a}_2$ on the graphite where \mathbf{a}_1 and \mathbf{a}_2 are graphite lattice vectors. The nanotube is also characterized by diameter $ \mathbf{C} $ and the chiral angle θ with respect to the zigzag axis ($\theta = 0$). | |
| Figure 1.4..... | 3 |
| Typical nanotubes obtained by rolling a graphite sheet: (a) zigzag ($n,0$); (b) armchair (m,m); and (c) chiral (n,m), where $n > m > 0$ by definition. | |
| Figure 1.5..... | 6 |
| Electronic band structure of a (10,10) metallic nanotube. HO – highest occupied band; LU – lowest unoccupied band. | |
| Figure 1.6..... | 8 |
| (a) Optical spectra of colloidal graphite and an SWNT rope (offset for clarity). (b) Electronic density of states for semiconducting (A, B) and metallic (C) nanotubes showing how A, B, and C features can be attributed to symmetric electronic transitions between the lowest subbands. | |
| Figure 1.7..... | 8 |
| Calculated electronic DOS of (10,10) and (11,8) metallic and (12,7) semiconducting nanotubes (Fermi level positioned at zero energy). | |
| Figure 1.8..... | 10 |
| Energies for symmetric transitions in SWNTs as a function of their diameter. | |
| Figure 1.9..... | 11 |

(a) Calculated phonon dispersion relations and (b) phonon density of states of a (10,10) metallic nanotube. The number of degrees of freedom is 120 and the number of distinct phonon branches is 66.

Figure 1.10.....13

A typical Raman spectrum of SWNT ropes showing three characteristic features: radial breathing modes (RBM) originating from tubes with different diameters, the *D*-band, and the split *G*-band.

Figure 2.1.....26

Cellular growth chart for the rat osteoblast MC3T3-E1 cells implanted on SWNT thin films. MTT colorimetric assay was applied to monitor primary osteoblastic cell viability. The cell culture reaches 100% confluency after about 5 days when the SWNT film is totally covered by the cells as fluorescent images show in the insert. The chart shows a regular behavior and normal growth rate of cells on SWNTs; data can be compared with viability of osteoblastic cells implanted on standard polystyrene for control. For the fluorescent images cells were stained using Calcein AM fluorescent dye (Invitrogen), 1 hour prior to rinsing with PBS. The cells were visualized under 10 X objective (Olympus) with 2.4 mm² field of view, on the areas marked with crossing lines. The plot is in logarithmic scale and error bars represent the standard error of the mean of 4 different samples.

Figure 2.2.....28

(a) Raman maps for the $I(D)/I(G)$ intensity ratio of SWNT films before and after cell implantation. (b) Typical Raman spectra of pristine SWNT films (black and blue lines), and SWNTs after 8 days (yellow line) and after 31 days (red line) of exposure to cells/media system show a time-increasing trend for the *D* band.

Figure 2.3.....30

(a) Sheet resistance of SWNTs exposed to cell-based system at variable time from cell implantation. Clear increase of sheet resistance in SWNT films is observed corresponding to increase in the exposure time to the cells. No significant increase in sheet resistance was observed for control samples (exposed to biological media only), but the increase due to the exposure to the cells was clearly observed for all samples after day 14. (b) Mean values of $I(D)/I(G)$ intensities ratio averaged on 36 points for each map in Fig. 2.2 (maps for day 0, 8 and 31 are shown) plotted versus exposure time. $I(D)/I(G)$ ratio increment is about 33% (within a 10-15% margin of error) after 31 days from cell implantation and the trend seems to become more evident as culture passes. A significant increase in $I(D)/I(G)$ ratio is clear only after day 14 indicating that a higher degree of disorder (creation of defects, vacancies,

formation of new covalent bonds via functionalization, etc.) has been introduced in the SWNT structure.

Figure 2.4.....31

(a) Raman *D* band position versus exposure time to the cells for the pristine SWNT film, SWNTs exposed to cell/biological media system and SWNTs exposed to proteins (dead cells) for 31 days. Variation in *D* band frequencies is not significant, values are scattered between 1307.5 and 1308.5 cm⁻¹ (experimental error is ±1 cm⁻¹). (b) Maps of SWNTs exposed to biological cells for 31 days show localized compressive (red) and tensional (yellow) stresses, indicative of the push-pull action of the living cells on the SWNT network.

Figure 2.5.....32

Raman signals ($\lambda_{\text{exc.}} = 633 \text{ nm}$) in the range of RBM mode (150-350 cm⁻¹) showing that both *m*-SWNT and *s*-SWNT are present in about the same ratio in the SWNT bundles after 31 days of cell exposure.

Figure 2.6.....34

FTIR spectra of the SWNT film as deposited (black line), SWNT film exposed to biological media only (dark green line), SWNT film exposed to proteins (purple line) and SWNT film used for implantation of living cells (red line). All data were collected after 1 day of exposure to the cell/biological media systems. Sharp peaks in the range (2320-2360 cm⁻¹) and (2850-2900 cm⁻¹) arise from the background.

Figure 2.7.....35

TEM images showing a superficial flake of the SWNT film used for cell implantation (the picture has been taken at day 15 from cells implantation). Close up view shows an entanglement of SWNTs and cells (bright areas). SWNT features (yellow circles) and evidence of SWNT uptake by the cells (dark spots inside the red circles) are also visible, indicating a good adhesion between growing cells and the SWNT substrate.

Figure 2.8.....36

High resolution TEM images of (a) pristine SWNT bundles, (b) SWNTs exposed for 15 days to biological media only used as control and (c) SWNTs exposed for 15 days to cell/biological media system. SWNT bundles used for cell implantation clearly show severe wall damages; the “sharkskin” surface indicates a slow degradation of the SWNTs with the exposure time. Localized mechanical stress induced by the push-pull action of the living cells and superficial covalent functionalization of SWNTs due to bio-chemical

interaction (cellular respiratory mechanism) are among the causes of such degradation.

| | |
|-----------------|----|
| Figure 3.1..... | 39 |
|-----------------|----|

Atomic structure of B_4C .

| | |
|-----------------|----|
| Figure 3.2..... | 39 |
|-----------------|----|

Boron-carbon phase diagram.

| | |
|-----------------|----|
| Figure 3.3..... | 41 |
|-----------------|----|

(a) Three structures showing the arrangement of icosahedra and chains corresponding to the stoichiometric polytypes $B_{11}C_p(C-B-C)$ and $B_{12}(C-C-C)$, respectively, and the most energetically favored non-stoichiometric polytype $B_{12}(CBC)$. (b) Gibbs energy versus relative abundance of the most significant polytypes. (c) Structure with segregated boron and carbon phase.

| | |
|-----------------|----|
| Figure 3.4..... | 44 |
|-----------------|----|

Raman spectra of single crystal B_4C , (0001) surface, taken at excitation wavelengths of 515, 633, and 780 nm.

| | |
|-----------------|----|
| Figure 3.5..... | 44 |
|-----------------|----|

Interpretation of the Raman spectrum of B_4C - (A) experimental spectrum, (B) theory for (a) $B_{12}(C-C-C)$, (b) polar $B_{11}C_p(C-B-C)$, and (c) equatorial $B_{11}C_e(C-B-C)$ configurations. Solid lines: E_g mode; dashed lines: A_{1g} mode.

| | |
|-----------------|----|
| Figure 3.6..... | 45 |
|-----------------|----|

Low frequency mode of B_4C , due to the torsion of the chain – atomic displacements of the Raman active modes observed at 481 cm^{-1} (rotation of the chain of about one axis perpendicular to the $[111]$ direction) and 535 cm^{-1} (librational mode of the icosahedra), and of the infrared active mode observed at $\sim 400\text{ cm}^{-1}$.

| | |
|-----------------|----|
| Figure 3.7..... | 47 |
|-----------------|----|

A typical Raman spectrum of amorphous/graphitic carbon showing characteristic D and G bands.

| | |
|-----------------|----|
| Figure 3.8..... | 47 |
|-----------------|----|

Carbon atoms motion in the (a) G and (b) D modes of vibration. Note that the G mode is due to the relative motion of sp^2 carbon atoms and it can be found in the chain as well.

| | |
|---|----|
| Figure 3.9..... | 51 |
| Energy band scheme of boron carbide based on optical absorption, luminescence and transport properties. Left ordinate, energies related to the valence band edge; right ordinate, energies related to the conduction band edge. Arrows indicate the direction of the measured transitions. | |
| Figure 3.10..... | 52 |
| Absorption coefficient versus photon energy in B ₄ C single crystal. | |
| Figure 3.11..... | 53 |
| Photoluminescence spectrum of B ₄ C single crystal at 290 K and 2.4 eV excitation energy. Squares, experimental results; thin solid line, averaged experimental results; bold solid line, recombination model of free excitons; bold dashed line, model for the transition of electrons between energy band and defect level. | |
| Figure 3.12..... | 55 |
| A typical dynamic response curve of a ceramic material showing plastic yielding and Hugoniot elastic limit. | |
| Figure 3.13..... | 56 |
| Representative shock compression profile in ceramic and schematic of brittle shear fracture process within the shock wave front. | |
| Figure 3.14..... | 56 |
| Shear stress τ_h and strength Y of boron carbide in the shocked state estimated from reshock and release experiments. | |
| Figure 3.15..... | 57 |
| Ballistic data on BC showing an abrupt drop in shear strength at impact pressures of 20-23 GPa. | |
| Figure 3.16..... | 58 |
| A boron carbide ballistic target that comminuted during impact (left) and a HR TEM image of a fragment produced by a ballistic test at impact pressure of 23.3 GPa (right). The lattice images on either side of the band correspond to the [1-101] direction of crystalline BC, and the loss of lattice fringes in the band indicates localized amorphization. | |
| Figure 3.17..... | 59 |

| | |
|--|----|
| (a) Plan view TEM micrograph of a 100 mN Berkovich indent; (b) a magnified image showing the amorphous bands along the (113) and (003) planes; (c,d) HR lattice images corresponding to the boxed area in (a,b). | |
| Figure 3.18..... | 60 |
| Raman spectra of (a) pristine single crystal $B_{4.3}C$; (b) indented single crystal; (c) indented hot-pressed polycrystalline sample; (d) scratch debris of a single crystal and (e) annealed scratch debris in air by using an argon ion laser with excitation wavelength of 514.5 nm. | |
| Figure 3.19..... | 61 |
| <i>In situ</i> Raman spectra of single crystal BC under quasi-hydrostatic compression during (a) loading and (b) unloading. (d) Raman spectrum of recovered material acquired from the marked region in (c). | |
| Figure 3.20..... | 61 |
| <i>In situ</i> Raman spectra of single crystal BC under quasi-uniaxial compression during (a) loading and (b) unloading. (c) Raman spectra of recovered material acquired from areas similar to the marked region in (d). | |
| Figure 3.21..... | 62 |
| First principles simulation of the stabilization of $B_{11}C(C-B-C)$ under hydrostatic and uniaxial compression. (a) Compressed volume vs. pressure. The square data represent the volume change with hydrostatic pressure, and the circle data correspond to the volume change with uniaxial stress along the C-B-C atomic chain. (b) Atomic configurations of the B_4C unit cell at various pressures corresponding to data points in (a). | |
| Figure 3.22..... | 63 |
| Diagrams of the steps proposed by Fanchini et al. required to transform $B_{11}C_p(C-B-C)$ into B12 and graphite at 10^{-4} GPa and 16 GPa. The transformation steps involve migration of C atom in the icosahedron from a polar to an equatorial site [$B_{11}C_p(C-B-C)$ to $B_{11}C_e(C-B-C)$]; migration of the B atom in the chain from the central to a boundary site [$B_{11}C_p(C-B-C)$ to $B_{11}C_e(B-C-C)$]; swapping of the equatorial icosahedral C atom with the boundary B atom in the chain [$B_{11}C_e(B-C-C)$ to $B_{12}(C-C-C)$]; coalescence of the obtained (CCC) chains along the (113) planes, through a rotation of their axis around the [001] direction. | |
| Figure 4.1..... | 67 |
| Density, mean free path, incidence rate, and monolayer formation versus pressure. | |

| | |
|---|----|
| Figure 4.2..... | 69 |
| Schematic of a film growth process. | |
| Figure 4.3..... | 69 |
| Effect of temperature and gas pressure on film microstructure. Porous structure (voids and crystallites), densely packed grains, columnar grain and recrystallized grain structure are observed. | |
| Figure 4.4..... | 71 |
| Schematic of energized plasma during sputtering (glow discharge). Upper insert shows a simplified model of film deposition. | |
| Figure 4.5..... | 77 |
| Gibbs free energy of the $B_{11}C_p(C-B-C)$ and $B_{12}(C-C-C)$ polytypes as a function of silicon atoms concentration. It can be observed that the difference in Gibbs free energy between the stable polytype, $B_{11}C_{(1-y,p)}Si_{(y,p)}(C-B-C)$ and the most energetically favored minority polytype, $B_{12}(C-Si_yC_{(1-y)}-C)$ increase with the silicon content. Hence, silicon-containing boron carbide is less affected by disorder than the undoped one. | |
| Figure 4.6..... | 79 |
| (a) Schematic of RF magnetron sputtering system belonging to University of Coimbra. Two RF power supplies are attached to the target and substrate respectively, two target positions are available and the sample holder disk is rotational. The sputtering chamber is connected with a mechanical and turbo pump able to achieve a ultra high vacuum (10^{-4} Torr). A metal resistance can be introduced as heater to sputter at high temperature. (b) Schematic of the RF magnetron sputtering system belonging to Rutgers University. Only one power supply is applied to the target, three targets are available, sample holder and shutter are both rotational. A simple heater was designed to perform high temperature deposition up to 500 °C. | |
| Figure 4.7..... | 80 |
| Set of sputtering deposition experiments performed at University of Coimbra. BC thin films were obtained by varying substrate bias from -30 to -170 V negative bias. Other experiments were carried out at zero bias but they were annealed at high temperature (up to 1000 °C) after deposition. Many films flaked off because of the weak adhesion between film and substrate. | |
| Figure 4.8..... | 81 |

| | |
|--|----|
| (a) Optical microscopy images of flaked BC film deposited at zero bias and 700 °C. (b) Raman spectra showing broad features from 200 to 1200 cm ⁻¹ , characteristic of <i>a</i> -BC. Data are in agreement with recent publications. | |
| Figure 4.9..... | 82 |
| Raman spectra for films deposited on grounded substrate at temperatures of 500, 700, 800, 900, 940 and 970 °C and boron carbide target material. | |
| Figure 4.10..... | 83 |
| (a) Optical images and (b) Raman spectra of films sputtered at different temperatures. Carbon <i>D</i> (1330 cm ⁻¹) and <i>G</i> (1580 cm ⁻¹) bands are observed. No crystalline BC was formed. No boron carbide features are observed but only Si peaks belonging to the substrate. | |
| Figure 4.11..... | 84 |
| Infrared spectra showing the transmission bands for the <i>α</i> -BC flakes. The enhanced bands at ~1100 cm ⁻¹ are probably related to the icosahedra modes, while the bands at 600 and 1440 cm ⁻¹ could be associated with the presence of the carbon bonds. | |
| Figure 4.12..... | 85 |
| SEM images of (a) unbiased sputtered <i>a</i> -BC, delaminating area leave discovered the Ti interlayer; (b) sputtered <i>a</i> -BC film deposited on Ti interlayer applying -170V substrate bias, the <i>a</i> -BC film has a strong adhesion with the silicon substrate and shows a nanogranular morphology. | |
| Figure 4.13..... | 87 |
| Raman spectroscopy on BC films sputtered on Ti interlayer by varying the negative substrate bias from 0 to -170 V. The unbiased film (in black) has flaked off and the remaining layer of material only shows the presence of free carbon. | |
| Figure 4.14..... | 88 |
| XRD pattern of a BC film sputtered on top of Ti interlayer. The film was sputtered at RT, applying a negative bias of -70 V. The TiO ₂ peaks are shifted by about 1-2 degrees demonstrating that the interlayer is experiencing residual tensile stress after deposition. The small peaks are related to the presence of boron, probably <i>β</i> -B, and graphitic carbon. | |
| Figure 4.15..... | 90 |

| | |
|---|-----|
| (a) Deposition rate and chemical composition of BC films as function of the negative bias. Results can be compared with literature data (Ref. [203]) in (c). (b) Hardness of deposited BC films as function of negative bias (SEM micrograph shown as an inset). | |
| Figure 4.16..... | 91 |
| (a) Hardness and atomic C/(C+B) ratio of the as deposited BC:Si films as a function of the silicon content. (b) Evolution of the hardness of BC:Si coatings as a function of annealing temperature in protective atmosphere. | |
| Figure 4.17..... | 92 |
| RF magnetron sputtering system belonging to Rutgers University: (a) external view, (b) open vacuum chamber, (c) close up view of target-substrate configuration, (d) designed heater. | |
| Figure 4.18..... | 93 |
| Set of sputtering deposition experiments run at Rutgers. BC thin films obtained by varying temperature are in the red box. | |
| Figure 4.19..... | 95 |
| Raman spectroscopy on films sputtered at (a) RT and 230 °C and (b) 415 °C. Films were deposited by using the sputtering system implemented in Fig. 4.17. Formation of boric acid and boron oxide has been detected due to poor vacuum conditions during deposition. | |
| Figure 5.1..... | 99 |
| Voltage versus current characteristic of low-density plasma discharge regimes without tips or edge. The point H at about 1 Amps indicate the inversion of the slope corresponding to the transition between glow and arc discharge. | |
| Figure 5.2..... | 102 |
| Linear fall in potential through the arc when ionization is produced in the gas between the two electrodes. | |
| Figure 5.3..... | 102 |
| Illustration of arc discharge between two carbon electrodes. The positive anode presents a concave bright part called crater (c); the negative cathode is usually pointed and is left in darkness. | |
| Figure 5.4..... | 104 |

| | |
|--|-----|
| (a) Conventional circuit for dc electrical discharges in tubes. (b) Stabilization of the electric arc due to the ballast resistor R_b (C is the stable operating point). | |
| Figure 5.5..... | 110 |
| Instrumental set up for the submerged arc discharge experiment: (a) schematic, (b) a photo of an actual setup. The boron carbide electrodes are obtained from hot pressed BC pieces, the ends of the electrodes are sharpened in order to promote the formation of the arc between them. The electrodes are submerged in liquid nitrogen/de-ionized water or inert gas and DC current is applied to them while the distance between the BC sharp points is slowly lowered until the anode touches the cathode to initiate an electric arc. | |
| Figure 5.6..... | 111 |
| A method based on specific gravity of the different nanostructures has been developed to self-separate the various types of nanostructures. | |
| Figure 5.7..... | 112 |
| Raman spectra of boron carbide soot obtained by submerged arc discharge between two graphitic electrodes. For the bottom part of the solution (black line), BC peaks already discussed in Chapter 4 are present. For the upper part of the solution (red line), larger amounts of carbon (D and G peaks) are detected. Peaks at $\sim 520\text{ cm}^{-1}$ and 900 cm^{-1} come from Si substrate. | |
| Figure 5.8..... | 113 |
| XRD spectra of boron carbide soot obtained by submerged arc discharge between two graphitic electrodes. BC peaks (squares) and C peaks (circles) indicate the presence of crystalline BC deposited on the bottom of the recipient and mostly graphitic carbon in the upper part of the beaker. | |
| Figure 5.9..... | 114 |
| SEM images of collected soot performed obtained at an accelerating voltage of 10 kV and a working distance of 6 mm. Different nanostructures were formed during the arc discharge in liquid nitrogen: (a) nanograins, (b,c) nanotubes, (d) nanoribbons, and (e) rigid nanorods. The image in the center shows a low magnification image. | |
| Figure 5.10..... | 115 |
| TEM and EELS analysis of soot particles: (a) low and (b) high resolution images of nanotubes; (c) a close-up view on the granular structure. | |
| Figure 5.11..... | 116 |

Raman spectra of boron carbide soot obtained by arc discharge between two B_4C electrodes submerged in DI water (red and green lines) and Ar gas (blue line). The spectrum of a B_4C electrode is also shown for reference (black line). Inset shows an optical image of the soot for a DI water submerged experiment.

CHAPTER 1.

STRUCTURE AND PROPERTIES OF SINGLE-WALLED CARBON NANOTUBES (SWNTs)

1.1 Atomic bonding and structure of SWNTs

Due to their particular electronic structure, carbon atoms allow various types of bonding that are responsible for formation of structures with different properties. Each carbon atom has six electrons, two of which fill the $1s$ orbital and do not contribute to bonding, while the remaining four electrons fill the $2s$ and $2p$ orbitals and can form the sp^3 , sp^2 , or sp hybridized bonds [1], as illustrated in Figure 1.1.

In diamond [1], the four valence electrons of each carbon atom occupy the sp^3 hybridized orbital and create four equivalent σ covalent bonds to connect four other carbon atoms in tetrahedral directions (Figure 1.2a). In graphite, three outer-shell electrons of each carbon atom occupy the planar sp^2 hybridized orbital to form three in-plane σ bonds with an out-of-plane π bond. This makes strongly bonded planar hexagonal networks of carbon atoms (graphite sheets) that are held together parallel to each other by weak van der Waals forces (Figure 1.2b).

A single walled carbon nanotube (SWNT) can be viewed as a hollow cylinder formed by rolling graphite sheets [2, 3] (Figure 1.2c). Bonding in SWNTs is essentially sp^2 . However, the circular curvature of the sheet leads to quantum confinement and $\sigma-\pi$ rehybridization in which three σ bonds are slightly out of plane; for compensation, the π orbital is more delocalized outside the tube. This bonding allows topological defects such as pentagons and heptagons to be incorporated into the hexagonal network to form

capped, bent, toroidal, and helical nanotubes whereas electrons will be localized in pentagons and heptagons because of redistribution of π electrons. The SWNT is called defect free if it is of only hexagonal network and defective if it also contains topological defects such as pentagons and heptagons, or other chemical and structural defects [4]. A group of coaxial SWNTs is called a multi-walled carbon nanotube (MWNT) [5].

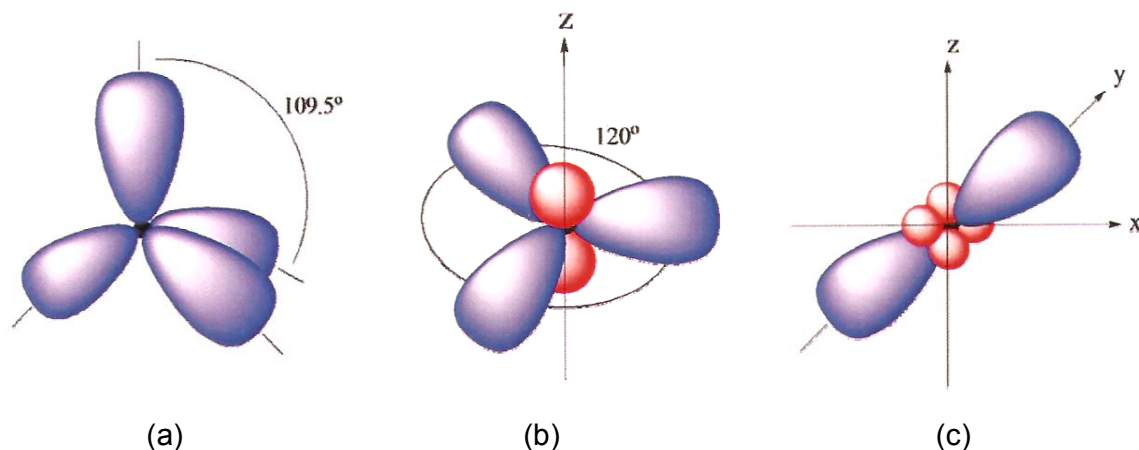


Figure 1.1. Bonding between carbon atoms: (a) sp^3 , (b) sp^2 , and (c) sp -hybridized orbitals.

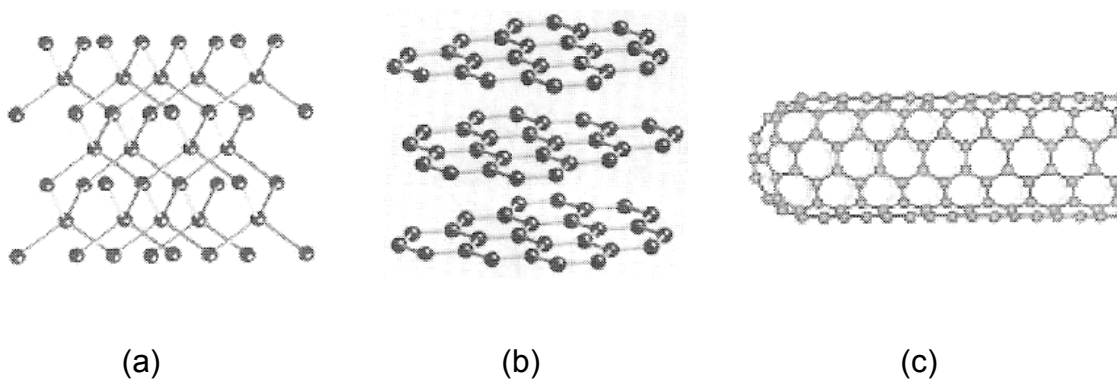


Figure 1.2. Arrangement of carbon atoms in (a) diamond, (b) graphite, and (c) nanotube structure.

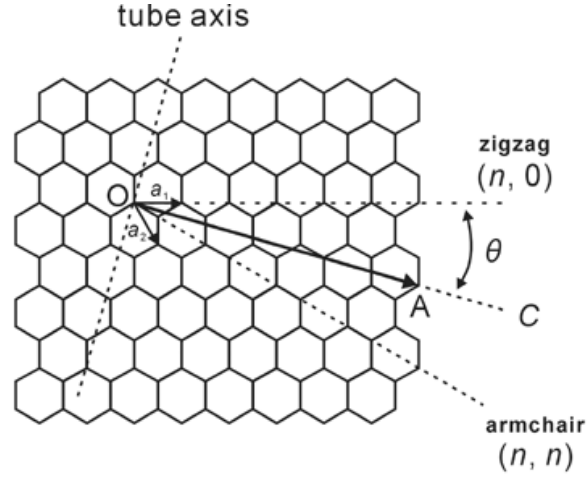


Figure 1.3. A nanotube (n,m) is formed by rolling a graphite sheet along the chiral vector $\mathbf{C} = n\mathbf{a}_1 + m\mathbf{a}_2$ on the graphite where \mathbf{a}_1 and \mathbf{a}_2 are graphite lattice vectors. The nanotube is also characterized by diameter $|\mathbf{C}|$ and the chiral angle θ with respect to the zigzag axis ($\theta = 0$).

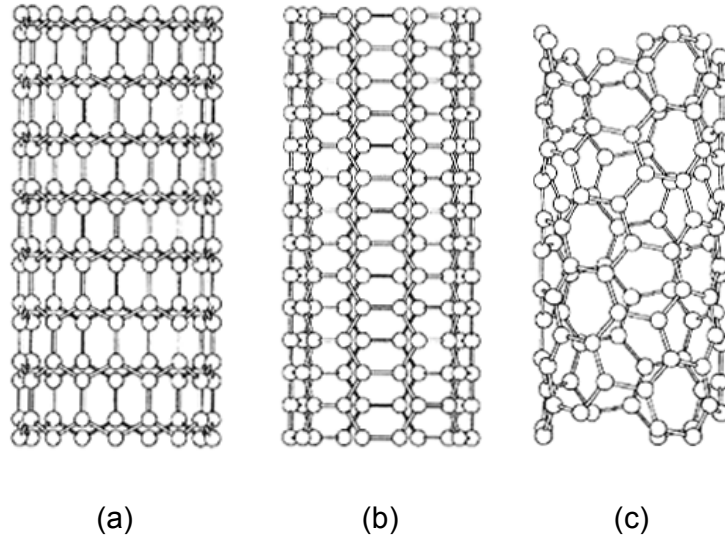


Figure 1.4. Typical nanotubes obtained by rolling a graphite sheet: (a) zigzag $(n,0)$; (b) armchair (m,m) ; and (c) chiral (n,m) , where $n > m > 0$ by definition.

The SWNT can be uniquely characterized by a vector \mathbf{C} in terms of a set of two integers (n,m) corresponding to graphite vectors \mathbf{a}_1 and \mathbf{a}_2 (Fig. 1.3) [6]:

$$\mathbf{C} = n\mathbf{a}_1 + m\mathbf{a}_2 \quad (1.1)$$

The SWNT is constructed by rolling up the graphite sheet such that the two end-points of the vector \mathbf{C} are superimposed. This tube is denoted as (n,m) tube with diameter given by

$$D = \frac{|\mathbf{C}|}{\pi} = \frac{a\sqrt{n^2 + nm + m^2}}{\pi} \quad (1.2)$$

where $a = |\mathbf{a}_1| = |\mathbf{a}_2|$ is lattice constant of graphite. The tubes with $m = n$ are commonly referred to as armchair tubes and $m = 0$ as zigzag tubes. Other tubes are generally called chiral tubes with the chiral angle, θ , defined as that between the vector \mathbf{C} and the zigzag direction \mathbf{a}_1 ,

$$\theta = \tan^{-1} \frac{m\sqrt{3}}{m + 2n} \quad (1.3)$$

Chiral angle θ ranges between 0° for zigzag ($m = 0$) and 30° for armchair ($m = n$) tubes. For convention, a condition that $n \geq m$ is always applied. Examples of zigzag, armchair, and chiral nanotubes are shown in Fig. 1.4.

The lattice constant and intertube spacing are required to generate a SWNT, SWNT bundle, and MWNT. These two parameters vary with tube diameter or in radial direction. The majority of experimental measurements and theoretical calculations suggest the average C-C bond length of $d_{cc} = 0.142$ nm (equivalent to $a = |\mathbf{a}_1| = |\mathbf{a}_2| = 0.246$ nm) and the average intertube spacing of $d_{tt} = 0.34$ nm [6]. Typically, experimentally observed SWNT diameter lays between 0.6 and 2.0 nm. Larger SWNTs tend to collapse unless they are supported by other forces or surrounded by neighboring tubes, as in MWNT. Typically, MWNT inside diameter is larger than 2 nm

and outside diameter is smaller than 100 nm. A SWNT rope is usually formed through a self-organization process in which van der Waals forces hold individual SWNTs together to form a triangular lattice with a constant (average intertube spacing) of 0.34 nm.

In addition to defect-free nanotubes, experimentally observed structures also include the capped and bent [7], branched [8], and helical [9] MWNTs, and the capped [10], bent [11], toroidal [12] SWNTs. In general, most SWNTs are defect-free whereas MWNTs are relatively more defective, containing either topological defects (pentagons and heptagons incorporated into the hexagonal network) or structural defects (discontinuous or cone-shaped walls or bamboo structure). Incorporation of defects will greatly affect nanotube properties; for example, the measured values of electrical and thermal conductivity and elastic modulus can vary as much as several orders of magnitude from sample to sample [4].

1.2 Electronic and optical properties of SWNTs

Due to their extremely small size and the highly symmetric structure, carbon nanotubes are characterized by quantum confinement effects leading to remarkable electronic, optical, and magnetic properties. In the simplest model [13, 14], the band structure of a nanotube derived from the dispersion relation of a graphite sheet with the wave vector $\mathbf{k} = (k_x, k_y)$ is expressed as follows:

$$E(k_x, k_y) = \pm \gamma \sqrt{1 + 4 \cos\left(\frac{\sqrt{3}}{2} k_x a\right) \cos\left(\frac{1}{2} k_y a\right) + 4 \cos^2\left(\frac{1}{2} k_y a\right)} \quad (1.4)$$

where $\gamma = 2.5 - 3.2$ eV is the nearest neighbor hopping parameter and $a = 0.246$ nm is lattice constant [4].

When the graphite sheet is rolled over to form a nanotube, a periodic boundary condition is imposed along the tube circumference or the **C** direction. This condition quantizes the two dimensional wave vector **k** along this direction. The **k** values satisfying the relation $\mathbf{k} \cdot \mathbf{C} = 2\pi q$ are allowed where q is an integer number. This leads to the following condition at which metallic conductance occurs (i.e., band gap closes):

$$(n - m) = 3q \quad (1.5)$$

This suggests that one third of the tubes are metallic and two thirds are semiconducting. A typical band structure of a metallic SWNT [15] is shown in Fig. 1.5.

The band gap of the semiconducting tube is given by

$$E_g = \frac{2d_{cc}\gamma}{D} \quad (1.6)$$

The above derivation does not consider the curvature effect or $\sigma-\pi$ rehybridization. This effect has been investigated using various approaches, including

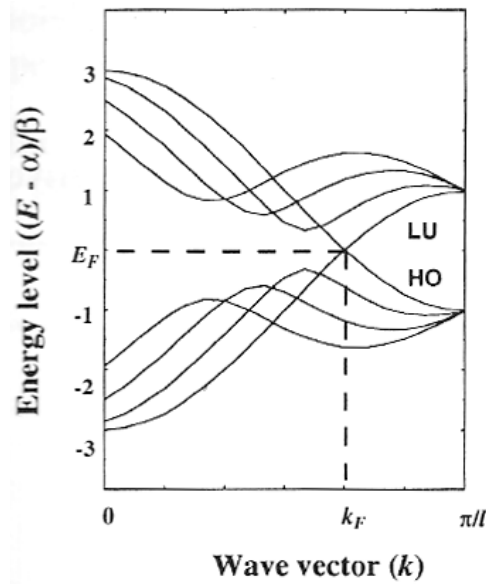


Figure 1.5. Electronic band structure of a (10,10) metallic nanotube [15]. HO – highest occupied band; LU – lowest unoccupied band.

first principles calculations [16-19]. It is found that $\sigma-\pi$ rehybridization can open up a small band gap (~ 0.02 eV) for smaller (< 1.5 nm) nonarmchair metallic tubes, but this effect is rapidly disappearing with the tube diameter. In principle, only armchair tubes are intrinsically metallic. However, for most discussions the metallization condition $(n-m)=3q$ and the band structure predicted from only the simplest π -orbital model have been accepted.

The nanotube is a one-dimensional conductor and has to be aligned between two electrodes for proper transport measurements. Due to $\sigma-\pi$ rehybridization, the π electron is more delocalized in a defect-free nanotube compared to graphite and therefore SWNTs should be characterized by lower electrical resistivity values. However, because SWNT ropes and MWNTs are often randomly oriented in the nanotube sheets, the actual measured resistivity values are much higher than those of graphite. Only when the measurements are carried out for the purified SWNT ropes or MWNTs aligned across four electrodes, the electrical resistivity of carbon nanotube sheets is consistently comparable with that of the highest quality graphite sheets ($0.4 \mu\Omega\cdot m$) [1, 20, 21].

Defect-free SWNTs offer direct band gap and well defined band and subband structure, which is ideal for optical and optoelectronic applications. A typical optical spectrum measured for a SWNT rope is shown in Fig. 1.6 with that for a graphite sample for comparison [22]. Three peaks for the SWNT ropes that cannot be observed in graphite are attributed to symmetric transitions between the lowest subbands in semiconducting (A and B) and metallic (C) tubes. The measured peak positions and intensity can be correlated with electronic structures or tube chirality (n,m) .

Optical and optoelectronic properties of SWNTs can be understood from their

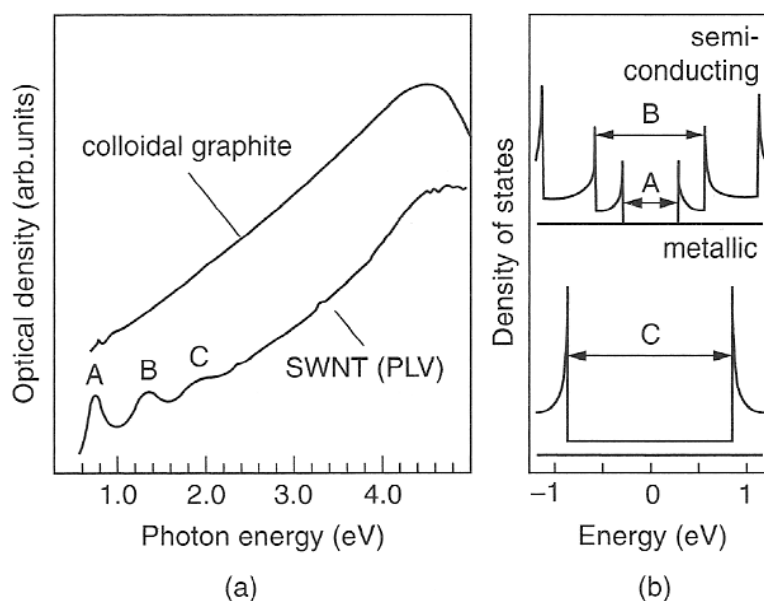


Figure 1.6. (a) Optical spectra of colloidal graphite and an SWNT rope (offset for clarity). (b) Electronic density of states for semiconducting (A, B) and metallic (C) nanotubes showing how A, B, and C features can be attributed to symmetric electronic transitions between the lowest subbands [22].

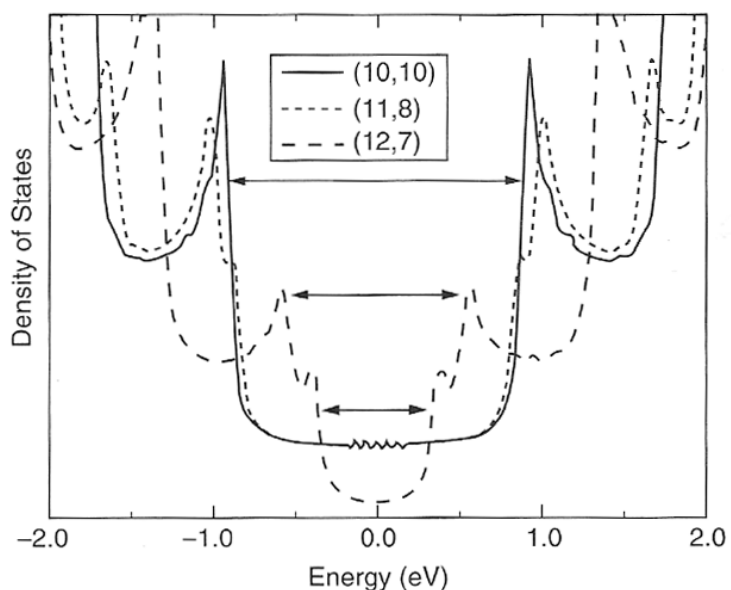


Figure 1.7. Calculated electronic DOS of (10,10) and (11,8) metallic and (12,7) semiconducting nanotubes [4].

electronic band structure or density of states (DOS). The one-dimensional DOS of a SWNT can be derived from that for graphite with the expression [4]

$$\rho(\varepsilon) = \frac{4}{l} \frac{2}{\sqrt{3}\gamma a} \sum_{m=-\infty}^{\infty} g(\varepsilon, \varepsilon_m), \quad (1.7)$$

where

$$g(\varepsilon, \varepsilon_m) = \frac{|\varepsilon|}{\sqrt{\varepsilon^2 - \varepsilon_m^2}} \quad \text{for} \quad |\varepsilon| > |\varepsilon_m|;$$

$$g(\varepsilon, \varepsilon_m) = 0 \quad \text{for} \quad |\varepsilon| < |\varepsilon_m|;$$

and

$$|\varepsilon_m| = \frac{|3q - n + m|\gamma a}{\sqrt{3}D}.$$

Calculated electronic DOS of metallic (10,10), (11,8) and semiconducting (12,7) nanotubes is shown in Fig. 1.7. The Fermi level is positioned to zero. The left- and right-hand sides to the Fermi level define valence and conductance band, respectively. The peak in DOS is called van Hove singularity. The optical transition occurs when electrons or holes are excited from one energy level to another, denoted by E_{pq} . The selection rules, $p = q$, for interband transitions that are symmetric with respect to the Fermi level require polarized light parallel to the tube axis, as shown by A, B, and C absorption features in Fig. 1.6. The energy corresponding to the symmetric transition $p = q$ for semiconducting (S) and metallic (M) tubes follows the relations with one p -orbital approximation:

$$E_{pp,S} = \frac{2pd_{cc}\gamma}{D} \quad \text{and} \quad E_{pp,M} = \frac{6pd_{cc}\gamma}{D}. \quad (1.8)$$

The number p ($p = 1, 2, \dots$) is used to denote the order of the valence and conduction bands symmetrically located with respect to the Fermi level; $p = 1$ defines the

band gap of a semiconducting tube. Thus, a map can be created taking possible values of p and D for metallic and semiconducting tubes, as shown in Fig. 1.8.

Also included in Fig. 1.8 is the tube curvature-induced $\sigma-\pi$ rehybridization effect with which only armchair tubes ($n = m$) are truly metallic whereas other tubes satisfying the relation $n - m = 3q$ are semi-metallic with a small band gap. Taking gap energy $E = 2.5$ eV for low bound and 3.0 eV for high bound, it follows from Fig. 1.8 that the wavelength ($= hc/E$) of a semiconducting tube will vary between 300 and 3000 nm. This suggests possible application of semiconducting nanotubes in optical and optoelectronic devices from UV lasers to IR detectors.

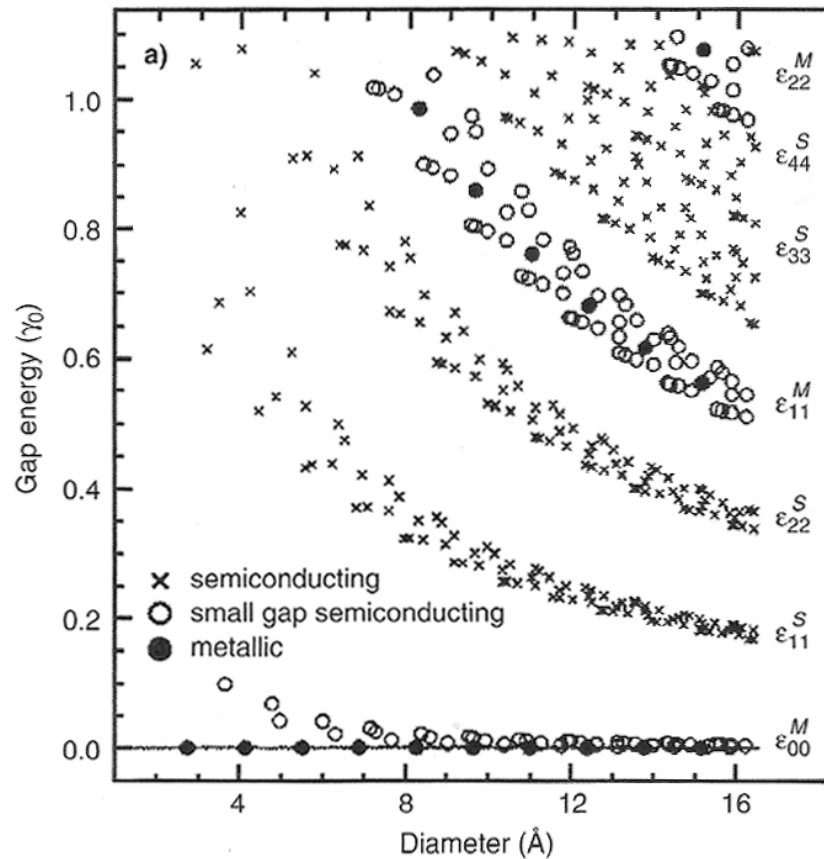


Figure 1.8. Energies for symmetric transitions in SWNTs as a function of their diameter [4].

1.3 Photon structure and vibrational properties of SWNTs

The phonon dispersion relations of SWNTs have been calculated using the tight binding molecular dynamic simulation methods, adopted for the SWNT geometry by scaling atomic force potential of a single graphite sheet [23, 24]. Fig. 1.9 shows the results obtained for the phonon dispersion relations $\omega(k)$ and the phonon density of states (PDOS) for two-dimensional graphite and a (10,10) nanotube. The PDOS for the (10,10) nanotube is close to that for 2D graphite, reflecting the zone-folded SWNT phonon dispersion.

As follows from Fig. 1.9, there are four acoustic modes in SWNTs. The lowest acoustic modes are the transverse acoustic (TA) modes, which are doubly degenerate, and have x and y displacements perpendicular to the SWNT z axis. The next acoustic mode is

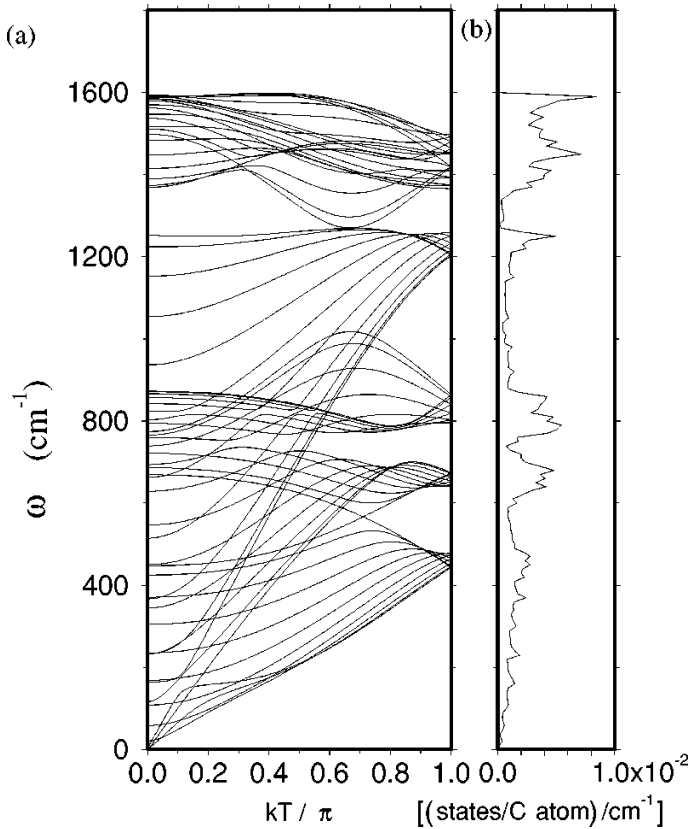


Figure 1.9. (a) Calculated phonon dispersion relations and (b) phonon density of states of a (10,10) metallic nanotube [24]. The number of degrees of freedom is 120 and the number of distinct phonon branches is 66.

the so-called twisting acoustic mode (TW), which has θ -dependent displacements in the SWNT surface [25]. The highest energy mode is the longitudinal acoustic (LA) mode whose displacements occur in the z direction.

The phonon dispersion relations of SWNTs are also characterized by a large number of optical modes (Fig. 1.9). The phonons with wave vector k inside the Brillouin zone are waves along the tube with wavelength $\lambda = 2\pi/k$. The zone-center ($k = 0$) phonons are atomic motions repeating in all unit cells along the tube. The atomic displacements for chiral tubes are not generally restricted to definite directions in space. However, the displacements for armchair and zigzag tubes can be classified as radial (R), circumferential (C), and axial (A).

The zone-center phonons of chiral tubes belong to the following symmetry species of point groups D_N [26]:

$$\Gamma = 3A_1 + 3A_2 + 3B_1 + 3B_2 + 6E_1 + 6E_2 + 6E_3 + \dots + 6E_{N/2-1}, \quad (1.9)$$

where modes $A_{1,2}$ and $B_{1,2}$ correspond to $l = 0$ and $N/2$, and modes E_i correspond to $l = i$. The E_i modes have $2l$ nodes around the tube circumference. The $A_{1,2}$ modes are nodeless and the $B_{1,2}$ ones have N nodes. Armchair and zigzag tubes have additional symmetry elements and the modes are classified by the irreducible representations of point group D_{2nh} .

Among the various zone-center phonons, some are infrared-active ($A_2 + 5E_1$ in chiral tubes, $3E_{1u}$ in armchair tubes, and $A_{2u} + 2E_{1u}$ in zigzag tubes), others are Raman-active ($3A_1 + 5E_1 + 6E_2$ in chiral tubes, $2A_{1g} + 2E_{1g} + 4E_{2g}$ in armchair tubes, and $2A_{1g} + 3E_{1g} + 3E_{2g}$ in zigzag tubes), and the rest are silent [26]. The A_{1g} , E_{1g} , and E_{2g} phonons are observed in the scattering configurations $(xx + yy, zz)$, (xz, yz) , and $(xx - yy, xy)$,

respectively, for z axis along the tube (following Porto notation, Ref. [27]).

A typical Raman spectrum of a SWNT rope is shown in Fig. 1.10. The largest Raman signal is observed for parallel scattering configuration and it originates from the following A_{1g} modes [28]:

- (i) one mode with a uniform radial atomic displacement (so-called radial breathing mode or RBM) with frequency following roughly the power law $230/d$ (in cm^{-1} ; d is the tube diameter in nm);
- (ii) one high-frequency mode of about 1580 cm^{-1} , which is purely circumferential in armchair tubes and purely axial in zigzag tubes (or two neither purely circumferential, nor purely axial modes in chiral tubes).

The Raman signal due to E_{1g} and E_{2g} phonons is usually very weak in SWNTs. Apart from lines due to single-phonon processes, bands arising from more complex processes are often observed in the Raman spectra. An example of such band is the so-

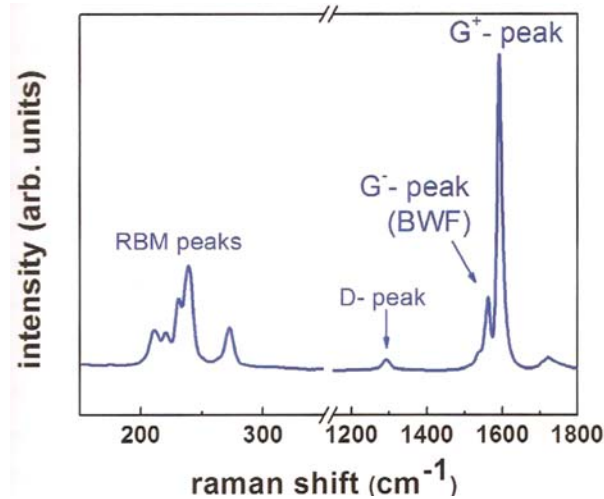


Figure 1.10. A typical Raman spectrum of SWNT ropes showing three characteristic features: radial breathing modes (RBM) originating from tubes with different diameters, the D -band, and the split G -band.

called D (for disorder) band which is due to the presence of impurities and defects in nanotubes (Fig. 1.10) and is characteristic for a wide range of carbon materials.

The Raman lines of the high-frequency A_{1g} modes of the different tubes are closely situated and modified by electron-phonon and electron-impurity interactions. The modeling of the latter ones also faces the problem of considering far enough neighbors in order to reproduce correctly the over-bending of the phonon branches of 2D graphite, from which these modes originate. On the other hand, the lines of the RBM modes in the measured spectra are often well-separated and can be used for structural characterization of the SWNT samples (Fig. 1.10). It has to be also noted that the Raman spectra of carbon nanotubes are usually measured under resonant conditions and nonresonant spectra are rarely observed because of the low signal.

1.4 Mechanical properties of SWNTs

Because σ bonding is the strongest existing in nature, a nanotube that is structured with all σ bonding is regarded as the ultimate fiber with the strength in its tube axis. Both experimental measurements and theoretical calculations agree that a nanotube is as stiff as or even stiffer than diamond with the highest Young's modulus and tensile strength [4]. The calculated mechanical properties of a (10,10) SWNT, an SWNT bundle, and MWNTs are shown in Table 1.1 together with similar data for graphite and steel. It should be noted that although the calculated data in Table 1.1 is in agreement with the experiments on average [29-31], experimental results show broad discrepancy, in particular for MWNTs, due to different amounts of defects present in MWNTs as artifacts of different growth approaches.

Table 1.1. Mechanical properties of carbon nanotubes [32].

| | Young's modulus (GPa) | Tensile strength (GPa) | Density (g/cm ³) |
|---------------------|--------------------------|---------------------------|---------------------------------|
| MWNT | 1200 | ~150 | 2.6 |
| SWNT | 1054 | 75 | 1.3 |
| SWNT bundle | 563 | ~150 | 1.3 |
| Diamond | 1220 | 90-225 | 3.5 |
| Graphite (in-plane) | 350 | 2.5 | 2.6 |
| Steel | 208 | 0.4 | 7.8 |

In general, various types of defect-free nanotubes are stronger than graphite. This is mainly because the axial component of σ bonding is greatly increased when a graphite sheet is rolled over to form a seamless cylindrical structure or an SWNT. Young's modulus is independent on tube chirality, but it does depend on tube diameter. The highest values for the Young's modulus are obtained from tube diameters of 1 and 2 nm, and are about 1 TPa. The mechanical properties of large tubes are approaching graphite, while the smaller tubes are less stable mechanically. When SWNTs of different diameters form a coaxial MWNT, the Young's modulus of the MWNT takes the highest value of an SWNT plus contributions from coaxial intertube coupling of van der Waals force. Therefore, the Young's modulus of MWNTs is higher than that of SWNTs, typically reaching 1.1 to 1.3 TPa. On the other hand, when many SWNTs are held together in a bundle or a rope, the weak van der Waals force induces a strong shearing among the packed SWNTs, decreasing Young's modulus of the bundle by as much as an order of magnitude [4].

The elastic response of a nanotube is also very remarkable. Most hard materials fail at strains of 1% or less due to the propagation of dislocations and defects. Both theory and experiment show that SWNTs can sustain up to 15% tensile strain before fracture [32]. Thus, the tensile strength of an individual nanotube can be as high as 150 GPa, assuming 1 TPa for Young's modulus. Such a high strain is attributed to an elastic buckling through which high stress is released. Elastic buckling also exists in twisting and bending deformation of nanotubes. All elastic deformation including tensile (stretching and compression), twisting, and bending in a nanotube is nonlinear, featured by elastic buckling of up to ~15% or even higher strain. This is another unique property of nanotubes, and such a high elastic strain for several deformation modes is originated from $\sigma-\pi$ rehybridization in SWNTs through which the high strain gets released.

1.5 Thermal properties of SWNTs

Because both graphite and diamond show extraordinary heat capacity and thermal conductivity, it is expected that carbon nanotubes have similar thermal properties. Indeed, experimental work confirms that at temperatures in excess of 100 K, specific heat of SWNTs, SWNT bundles, and MWNTs is close to that of graphite, or about 700 mJ/gK. However, due to quantum confinement effects at lower temperatures, heat capacity of carbon nanotubes decreases drastically and reaches only 0.3 mJ/gK for a (10,10) SWNT, ~0 mJ/gK for a SWNT bundle, and 2-10 mJ/gK for MWNTs [33, 34].

The thermal conductivity of both SWNTs and MWNTs should reflect the on-tube phonon structure, regardless of intertube coupling. Measurements of the thermal conductivity of the bulk samples show graphite-like behavior for MWNTs, but quite

different behavior for SWNTs, specifically a linear temperature dependence at low T , which is consistent with one-dimensional phonons. Both experimental and theoretical work established that thermal conductivity of SWNT bundles and MWNTs at room temperature varies from 1800 to 6000 W/mK, depending on the sample quality and tubes alignment [34, 35].

1.6 Chemical properties and biocompatibility of SWNTs

Small radius, large specific surface and $\sigma-\pi$ rehybridization make SWNTs very attractive in chemical and biological applications because of their strong sensitivity to chemical or environmental interactions. The chemical properties of interest include opening, wetting, filling, adsorption, charge transfer, doping, intercalation, etc.

The nanotubes end is more reactive than the sidewall because of the presence of pentagons or metallic catalysts occupying the opened ends and greater curvatures. Opening nanotubes ends has been achieved by vapor phase oxidation, plasma etching, and chemical reaction using acids such as HNO_3 . The opened end is typically terminated with a functional group [36-38].

SWNTs are hydrophobic and do not show wetting behavior for most aqueous solvents. It is reported that various organic solvents, HNO_3 , S, Cs, Rb, Se, and various oxides such as Pb and Bi_2O_3 can wet nanotubes [39-41]. A nanotube provides capillary pressure proportional to $1/D$. Therefore, these wetting agents can be driven to fill inside the nanotube by the capillary pressure. It should be also possible to fill non-wetting agents inside a nanotube by applying an external pressure that is higher than the capillary pressure.

Enhanced molecular adsorption and charge transfer can be expected for SWNTs. Strong adsorption and charge transfer of oxygen to SWNTs have been experimentally observed at room temperature. Theoretical calculations suggest that a number of gas molecules, such as $C_8N_2O_2Cl_2$, O_2 , C_6H_{12} , C_6H_6 , NO_2 , H_2O , NH_3 , CH_4 , CO_2 , N_2 , H_2 , and Ar can adsorb to various sites such as interstitial sites in the tube bundles, grooves above the gap between two neighboring tubes, nanopores inside a tube, and surfaces of a single tube [42-44]. In the charge transfer process, SWNTs can act as both donors and acceptors depending on the nature of the adsorbed molecule. Molecular adsorption provides a simple, noncovalent doping approach to turn SWNTs into p-type (with O_2 or H_2O adsorption) or n-type (with C_6H_{12}) semiconductors. On the other hand, intercalation of the alkali metals with nanotubes can be used to enhance metallic conductivity and intercalation of halogens to enhance electrochemical capability of SWNTs for charge transfer and storage [45-47].

The strong relationship between SWNTs electronic properties and their atomic structure and mechanical deformations makes them very attractive for developing extremely small sensors that are sensitive to the chemical, mechanical or physical environment [48]. Nowadays, there is a strong need for smaller, faster, cheaper and simpler biosensors able to extract more accurate and precise information from changes in biological processes [49]. When the size of the material approaches the size of the biomolecules (1-100nm), it directly interacts with the molecules. The reduction of the size of sensing and transducing elements makes it possible to detect down to single molecule. Sensing SWNT devices have already been fabricated for different applications [50-52]. Many studies have also reported complex hybrid nanostructures, and

heterogeneous assembly of biological molecules with SWNTs was used as a template for biomolecule assembly [53] or as conducting wires connecting biomolecules [54].

Carbon nanotubes may be considered a unique biomaterial. Owing to the increasing interest in tissue engineering, SWNTs can be used as powerful tool for monitoring and evaluating tissue growth [55]. There are mainly four areas that SWNTs can be used in:

- (i) Cell tracking and labeling [56]: the ability to track implanted cells in vivo and non-invasively would help in evaluating the viability of the engineered tissue and would also help in understanding of biodistribution and migration of transplanted cells. SWNTs possess many properties desirable for optical detection. For instance, SWNTs are characterized by optical transitions in the near infrared (NIR) region between 900 nm and 1300 nm; this is an important optical window because it minimizes interference problems such as tissue absorbing, scattered light, autofluorescence and photobleaching [57]. SWNTs display good photostability allowing long duration of tracking time. Moreover, the SWNTs hydrophobic nature permits them to remain in the cells during repeated cell divisions suggesting useful application for probing cell proliferation and stem-cell differentiation. More sophisticated methods can be introduced by modifying SWNTs with additional probes [58] or targeting agents.
- (ii) Sensing cellular behavior: the ability to monitor cellular physiology such as ion transport, enzyme/cofactor interactions, protein and metabolite secretion and cellular behavior such as matrix adhesion could help design better engineered

tissue. SWNTs could be used as contrast agent to monitor disease progress and therapy responses by detecting the change in relevant physiological parameters (i.e: pH, pO₂ and glucose levels). SWNTs are ideal nanosensors because of their large surface area that allows them to immobilize biological and chemical compounds (i.e: DNA and proteins) and their nanosize which permits the implantation of the probe without perturbing the system.

- (iii) Augmenting cellular behavior: controlling the production or delivery of tissue-inducing substances such as growth factor. SWNTs have already been used for pharmaceutical delivery [59, 60] and they could be used for delivery of genetic materials as well (i.e: DNA, RNA and bioactive proteins). The main advantage of using SWNTs for this application is that they can be heterogeneously functionalized.
- (iv) Matrix enhancement: the ability to reinforce the structural support used for the growth and development of engineered tissue. The commonly used biopolymers (i.e., PLGA and PLA) lack the necessary mechanical strength, in addition they are very difficult to functionalize. Mixing a small amount of SWNTs with the polymer, significant improvement in the mechanical strength of the composite scaffolds has been observed [61]. *In vitro* experiments demonstrated that SWNT can support the growth of different cell types such as muscle [62], fibroblasts, osteoblasts [63] and even neurons that can be grown on patterned arrays of carbon nanotubes creating neural networks [64] .

Although SWNTs appears to be a good substrate for cellular growth and an extremely powerful tool for biosensors, there is a debate in literature regarding the

cytotoxicity of SWNTs. Several in vitro studies reported necrosis and degeneration of human cells exposed to SWNTs [65], formation of granulomas and pulmonary inflammation [66]. On the other hand many experiments have shown that SWNT can support the growth of different cells such as smooth muscle [67], fibroblasts [62] and osteoblasts [63].

Any material of SWNT dimensions has the potential to be cytotoxic and even carcinogenic if it does not degrade quickly. New approaches are being developed to mitigate the potential cytotoxicity of SWNTs. For instance, it has been demonstrated that functionalized SWNTs are inert [68], also it has been found that SWNTs can be catalytically biodegraded by particular enzymes [69].

CHAPTER 2

DEGRADATION OF SINGLE-WALLED CARBON NANOTUBES STRUCTURE BY LIVING OSTEOBLAST CELLS IN BIO-IMPLANTATION

2.1 Motivation and research outline

Single-walled carbon nanotubes (SWNTs) combine unique electronic and optical properties with high mechanical strength and high thermal conductivity [70, 71]; for this reason over the last decades, scientists have been exploring SWNT for a variety of different applications [72-74]. Depending on their diameter and chirality, SWNTs are either one-dimensional metals or one-dimensional semiconductors suitable for fabrication of single electron transistors [75, 76] and field-effect transistors [77, 78]. Electronic devices based on SWNTs are promising for many other applications, ranging from molecular quantum wires [79] to electromechanical devices [80] and chemical/biological sensors [56, 81-84]. Recently, SWNTs have also received high attention in biomedical research as a potential substrate for cellular growth [55, 85-87]. However, the presumed cytotoxicity of SWNTs obliges scientists to investigate more on the effective risk of using SWNTs in living systems. Although some controversial studies and theories have been lately suggested [69, 88-90], it is generally accepted that chemical functionalization of the SWNT surface could mitigate the potential toxic effect associated with the nanotubes [55]. Recently, a detailed study showed total biodegradation of SWNTs in presence of human myeloperoxidase (hMPO), an enzyme known to be responsible for the degradation of implantable polymeric materials [69]. *In vitro* analysis confirmed that biodegraded SWNTs do not generate pulmonary inflammatory response that intact

SWNTs have shown to be responsible for. This finding reopens the debate about the use of nanotubes in biomedical applications.

At present, basic information about interactions between SWNTs and cells/biological media systems is missing. This study aims at establishing a correlation between the variations in fundamental properties, such as the electrical conductivity, and variations in structural characteristics of SWNT films exposed to specific conditions. Raman spectroscopy and Fourier transform infra-red spectroscopy (FTIR) are shown to be powerful tools for detailed analysis of the electronic changes of SWNT films engaged in implantation of living cells.

2.2 Experimental approach

Interaction of cells/biological media system with carbon nanotubes is expected to affect both their structure and their electronic properties via mechanical and/or chemical modifications. It has been already extensively shown by previous studies [91, 92] that after reaction of carbon nanotubes with host materials, dopants are intercalated either inside or between the tubes in the case of SWNTs, or in the inter-shell space in the case of multi-walled carbon nanotubes (MWNTs). Transformation of SWNTs due to electrochemical doping has been reported in many papers [93-96] and it has been explained for the first time by Chen *et al.* [95], who suggested a co-intercalation mechanism of large solvent molecules into the SWNT bundles and a side reaction at the electrode surface.

Changes in the electronic and phonon state of carbon nanotubes are easily detectable by the use of Raman spectroscopy. The presence of van Hove singularities in

the one dimensional joint density of electronic states (JDOS) of carbon nanotubes leads to a strong and unique electron-phonon coupling responsible for an unusual enhanced resonance Raman effect. A detailed study on the nature of the typical vibration modes observed for Raman scattering in SWNTs is discussed by Dresselhaus *et al.* [23, 97, 98]. The resonance Raman effect makes possible not only identification of vibrational and rotational modes of SWNT at a single nanotube scale but also determination of their structural properties such as diameter and chirality [99, 100] . It is not surprising, then, that today Raman spectroscopy is the most powerful and widely used tool for investigation of structural and electronic modifications of individual SWNTs [101]. Carbon materials are characterized by two strong first-order Raman features known as the *D* band (at $\sim 1250\text{-}1450\text{ cm}^{-1}$) and the *G* band ($1500\text{-}1605\text{ cm}^{-1}$). In particular, the *D* band is a dispersive band and its shape, peak width, intensity and position varies with the types of carbon and the particle size [102]. In SWNTs, the *D* band is related to sp^2 hybridized carbon and represents the breathing mode of each graphitic ring. Also, the *G* band is characteristic of the graphitic layers and in the Raman spectra of SWNTs it is a double feature corresponding to the tangential and radial vibrations of the carbons along the circumferential direction (G^-) and along the direction of the nanotube axis (G^+). Variations of the Raman signal in the spectral range of the *D* band provide information on the disorder state of the graphitic rings and the presence of induced defects in the nanotube skeleton. The *G* band is instead associated with the tangential modes and a shift of this band gives additional information about the C-C bond length and the Fermi energy rises in the tube structure [91].

An additional characteristic feature in the Raman spectra of SWNTs is the radial

breathing mode (RBM) associated with the in-phase vibrations of the carbon atoms in the radial direction. The RBM mode, which is strongly dependent on the diameter d and chirality (n,m) of SWNTs, makes it possible to detect the occurrence of selective reactions and/or transformations of metallic and semiconducting SWNTs by monitoring the changes in their corresponding Raman intensities (in the spectral range of 150-350 cm^{-1}) [81].

Further information on the vibrational state and the effect of cells on the SWNT films can be obtained by Fourier transform infra-red (FTIR) spectroscopy. This technique is particularly advantageous in identification of active chemical bonding and molecular structure of SWNTs, but it has much poorer spatial resolution compared to Raman and it is very sensitive to the amount of water and carbon dioxide present in the atmosphere. Finally, scanning (SEM) and transmission (TEM) electron microscopy techniques were employed to provide direct observation of the changes in SWNT as a result of interactions with cells/biological media.

Osteoblast precursor mouse MC3T3-E1 cells and purified SWNT bundles were used in this study. The SWNTs were purified and dispersed in water following the protocol reported by Xu *et al.* and Eda *et al.* [103, 104]. The SWNT suspension (35 mL) was deposited on 220 μm pore size filter mixed-cellulose ester membranes (MCE, Millipore) forming free standing SWNT films. The SWNT thin films (200-300 nm in thickness) were then placed on glass slides (Fisher Scientific) and successively cut into uniform circular samples ($d = 1.3\text{-}1.2$ cm). The obtained SWNT samples were finally dried in the oven and sterilized under UV light (254 nm) prior to living cells exposure.

MC3T3-E1 osteoblastic cells plated at 5000 cells/well were supplemented with

Eagle's minimal essential medium (α -MEM), 10% fetal bovine serum (FBS), 1% pen-strep bactericide (PS) at 37 °C for 21 days [105]. The osteoblast cells grown in presence of SWNTs did not show any apoptosis or uncontrolled cell proliferation. The growth chart in Fig. 2.1 indicates that the number of cells reaches the maximum plateau after 6 days in agreement with what is observed for cells implanted on standard polystyrene substrates [105]. Similarly, previous work [89] reported normal growth rates and unchanged morphologies of human epithelial-like cells incubated in the SWNT dispersion.

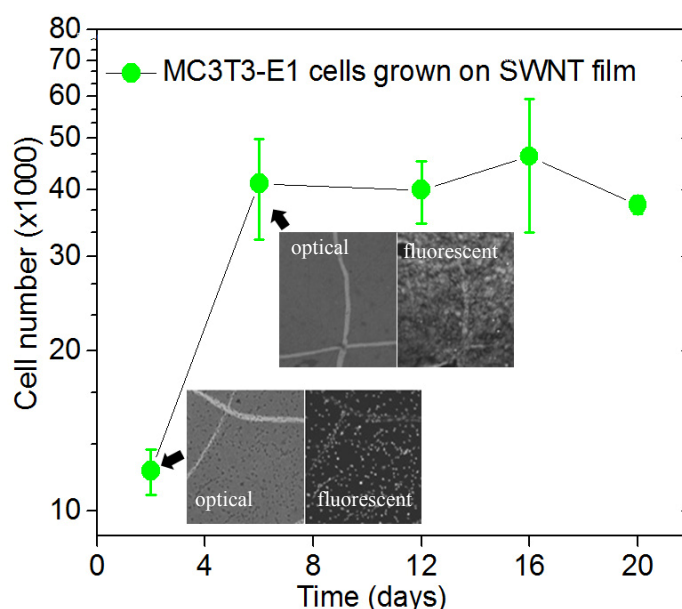


Figure 2.1. Cellular growth chart for the rat osteoblast MC3T3-E1 cells implanted on SWNT thin films. MTT colorimetric assay was applied to monitor primary osteoblastic cell viability. The cell culture reaches 100% confluency after about 5 days when the SWNT film is totally covered by the cells as fluorescent images show in the insert. The chart shows a regular behavior and normal growth rate of cells on SWNTs; data can be compared with viability of osteoblastic cells implanted on standard polystyrene for control. For the fluorescent images cells were stained using Calcein AM fluorescent dye (Invitrogen), 1 hour prior to rinsing with PBS. The cells were visualized under 10 X objective (Olympus) with 2.4 mm² field of view, on the areas marked with crossing lines. The plot is in logarithmic scale and error bars represent the standard error of the mean of 4 different samples.

In situ micro-Raman spectra were recorded at room temperature in a backscattering geometry under excitation wavelength of 633 nm using a Renishaw InVia Raman microspectrometer. Raman maps were collected by scanning with the laser a large area (200 x 200 μm) of an SWNT film before and after cell implantation; the collected spectra were then analyzed by Wire 2.0 software for peak fitting and mapping. Transmittance spectra ranging from 900 to 4000 cm^{-1} were acquired at normal incidence using a Perkin Elmer Lamda 20 FTIR spectrophotometer.

Electrical analysis of SWNTs exposed to cell-based system was carried out using an Agilent VEE Pro instrument. Silver ohmic contacts were attached to the SWNT films and the four-probe resistivity measurements were recorded by Van der Pauw method [106] applying a voltage sweep ramp.

TEM images were obtained using a Topcon 002B transmission electron microscope operating at 200 kV. Samples were prepared by dissolving the SWNT films in aqueous solutions at 1 wt.% of sodium dodecyl sulfate (SDS); the SWNT suspension was further subjected to gentle sonication for about 15 minutes and finally deposited by drop casting on holey carbon grids.

2.3 Results and discussion

Raman maps for the $I(D)/I(G)$ intensity ratio of SWNT films before and after cell implantation are shown in Fig. 2.2. The increasing intensity of the D peak with the exposure time of the SWNT films to the cells/media system suggests that a higher degree of structural disorder is present in the graphitic rings composing SWNTs. During the interaction between SWNTs and the cells/biological media system, it appears possible

that the SWNTs could have been damaged by the introduction of defects where carbon rings were broken, carbon atoms were missing and localized C=C bonds were created either by chemical processing or by mechanical stress induced by the push-pull action of the living cells. Furthermore, oxygen-containing groups might have been added to

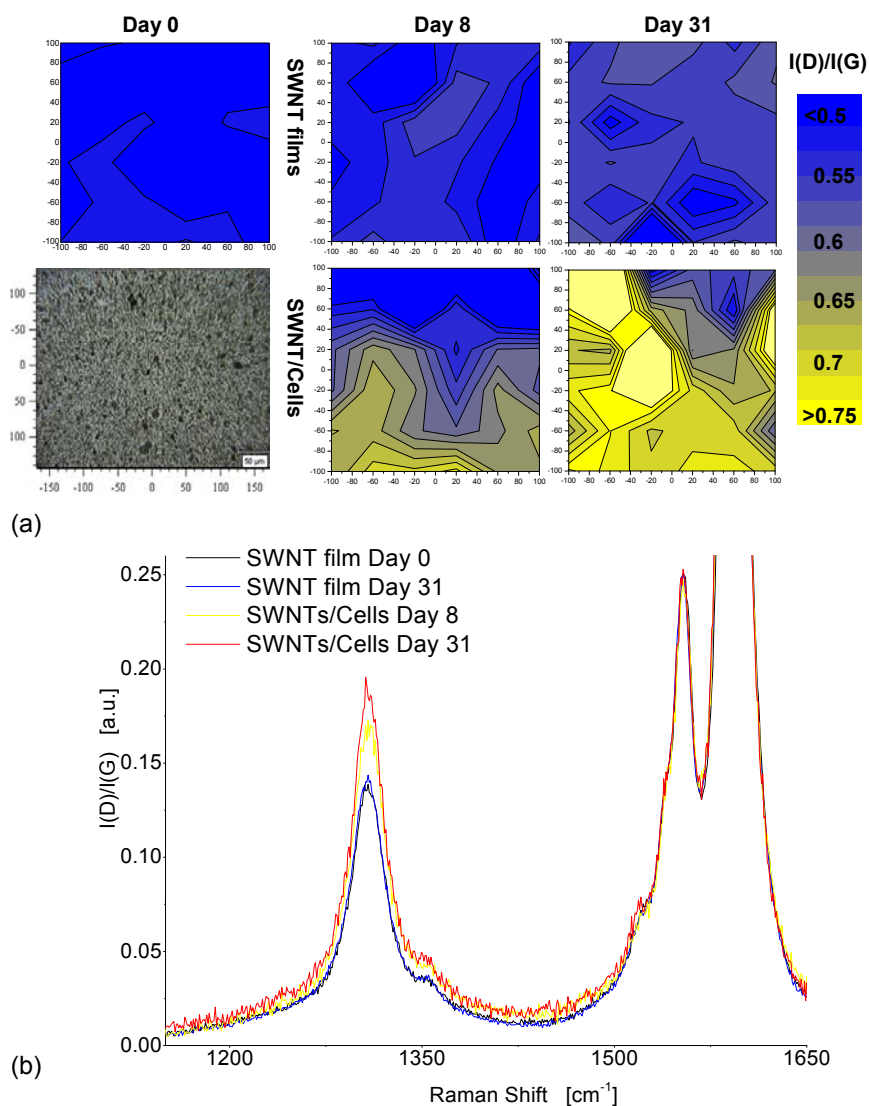


Figure 2.2. (a) Raman maps for the $I(D)/I(G)$ intensity ratio of SWNT films before and after cell implantation. (b) Typical Raman spectra of pristine SWNT films (black and blue lines), and SWNTs after 8 days (yellow line) and after 31 days (red line) of exposure to cells/media system show a time-increasing trend for the D band.

stabilize the wall defective structure leading to functionalization of the SWNTs with the formation of hydroxyl (OH) and carboxyl groups (COOH), in accordance with literature data [107]. The fact that the D peak is increasing in intensity but not changing its Lorentzian line shape suggests that structural disorder is introduced in the SWNT bundles without evident formation of amorphous carbon [108]. The intensity of the second-order overtone G^* band at $\sim 2600\text{ cm}^{-1}$, which is not disorder-induced, does not vary with exposure time (data not shown), confirming that amorphous carbon is not responsible for the increasing intensity of the D band.

It is well known that introduction of defects, such as vacancies, disorder, chemical modifications and bending in the SWNTs can lead to significant change in the electronic properties [109-113] due to the local destruction of the electron-hole symmetry of the π - π^* states, and to the formation of new structures in the densities of states such as tight-binding of the carbon π bands or quantum confinements (intratube quantum dots) etc. [114-118]. Similarly, *in situ* electrical measurements have revealed that the conductance of mechanically strained carbon nanotubes can significantly drop and theoretical simulations indicate that this effect is owing to the formation of local sp^3 bonds created during the mechanical deformation [80].

Conductivity measurements in Fig. 2.3 reveal a time-dependent increase in sheet resistance of the SWNT bundles exposed to cell implantation. Conversely, SWNT films exposed to biological media only did not significantly modify their resistance. The increasing rate of the sheet resistance with the exposure time of SWNTs to cells strongly suggests a “dynamic” interaction between living cells and SWNTs rather than merely mechanical attachment of the cells to the films. If the resistance increase were primarily

due to the simple attachment of the cells, it should have saturated after about 5 days, when the cell number reaches its maximum (cf. growth chart in Fig. 2.1) and the cells uniformly cover the SWNT substrate. In fact, an even steeper increase in resistance is observed at day 15 after the cell number saturation confirming a “dynamic” SWNTs-cells interaction.

By comparing the Raman analysis with the electrical results it is evident that the increasing trend of the intensities ratio $I(D)/I(G)$ with the exposure time correlates well

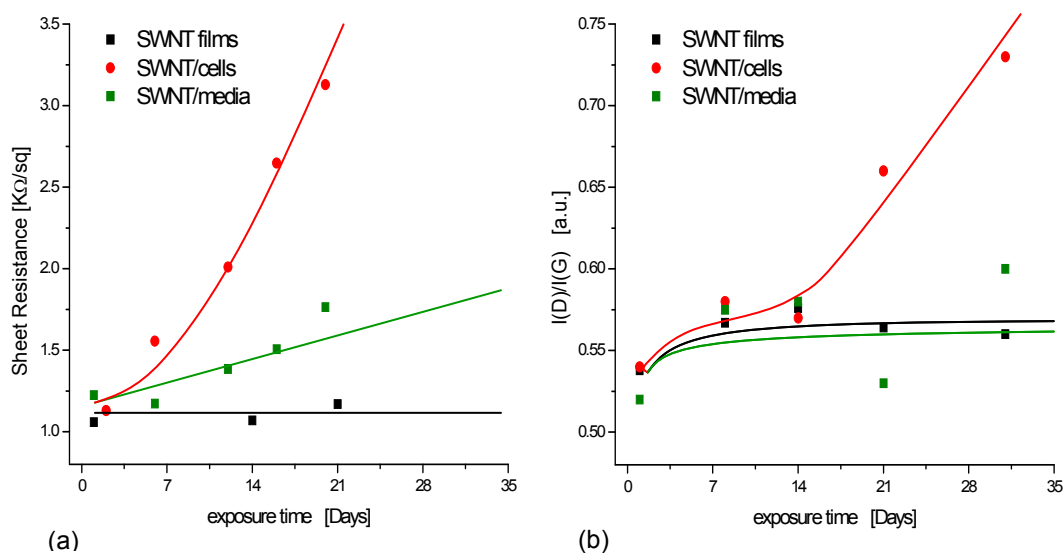


Figure 2.3. (a) Sheet resistance of SWNTs exposed to cell-based system at variable time from cell implantation. Clear increase of sheet resistance in SWNT films is observed corresponding to increase in the exposure time to the cells. No significant increase in sheet resistance was observed for control samples (exposed to biological media only), but the increase due to the exposure to the cells was clearly observed for all samples after day 14. (b) Mean values of $I(D)/I(G)$ intensities ratio averaged on 36 points for each map in Fig. 2.2 (maps for day 0, 8 and 31 are shown) plotted versus exposure time. $I(D)/I(G)$ ratio increment is about 33% (within a 10-15% margin of error) after 31 days from cell implantation and the trend seems to become more evident as culture passes. A significant increase in $I(D)/I(G)$ ratio is clear only after day 14 indicating that a higher degree of disorder (creation of defects, vacancies, formation of new covalent bonds via functionalization, etc.) has been introduced in the SWNT structure.

with the increment of sheet resistance. In both cases, SWNTs seem to significantly change their properties after about 15 days from cell implantation. However, tensional state induced by the living cells on the SWNTs should be taken into account because mechanical strains can also favor the formation of defects [112, 119] and induce the changes in electronic properties of SWNTs [80].

Frequency position of the characteristic Raman *D* band was recorded by mapping large areas of pristine SWNT film and SWNTs used for cell implantation; the averaged values were then plotted versus exposure time (Fig. 2.4a). Also, a control sample was prepared with a mix of proteins obtained by milling the living cells and depositing them on the SWNT substrate. Plot in Fig. 2.4a shows that the position of the *D* band did not significantly change (values range between 1307.5 and 1308.5 cm^{-1}) for the SWNTs exposed either to living cells or proteins (dead cells) for 31 days. Even if overall

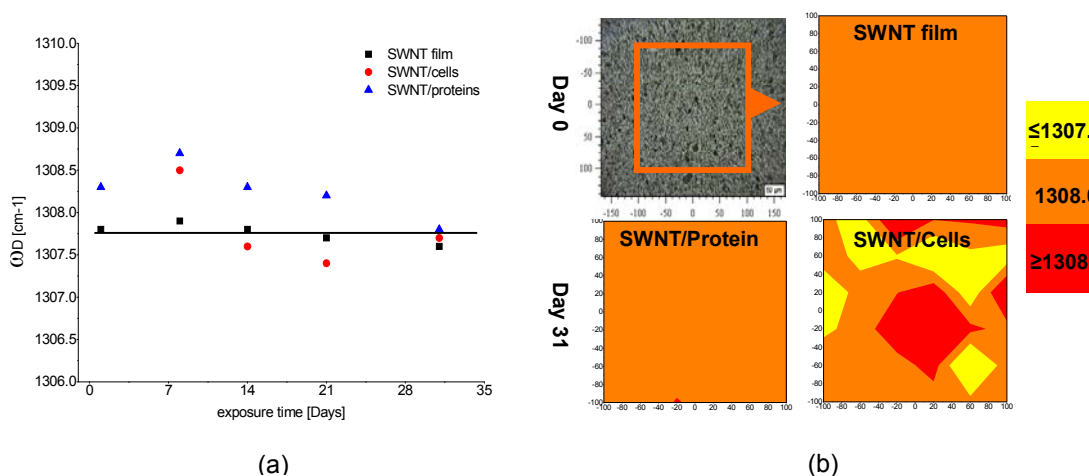


Figure 2.4. (a) Raman *D* band position versus exposure time to the cells for the pristine SWNT film, SWNTs exposed to cell/biological media system and SWNTs exposed to proteins (dead cells) for 31 days. Variation in *D* band frequencies is not significant, values are scattered between 1307.5 and 1308.5 cm^{-1} (experimental error is $\pm 1 \text{ cm}^{-1}$). (b) Maps of SWNTs exposed to biological cells for 31 days show localized compressive (red) and tensional (yellow) stresses, indicative of the push-pull action of the living cells on the SWNT network.

variations in vibrational frequencies were not observed, local tensional states for SWNTs exposed to living cells were detected by visualization of Raman mapping data (Fig. 2.4b). No change in *D* band position was observed for the SWNTs exposed to the proteins indicating that the SWNT network experiences weak tensional and compressive states due to the dynamic action of the cells (a push-pull mechanism owing to breathing, moving and growing of the cells). In any case, the physical interaction between SWNTs and cells does not affect the overall structure of the bundles which can easily release the weak tensional states when the cells are removed. In conclusion, it is reasonable to assume that the decrease in conductivity is mainly caused by the cell-induced disorder or chemical functionalization and not by significant mechanical stress imposed by the cells on the SWNT bundles.

In order to exclude the hypothesis of any possible selective reaction of metallic

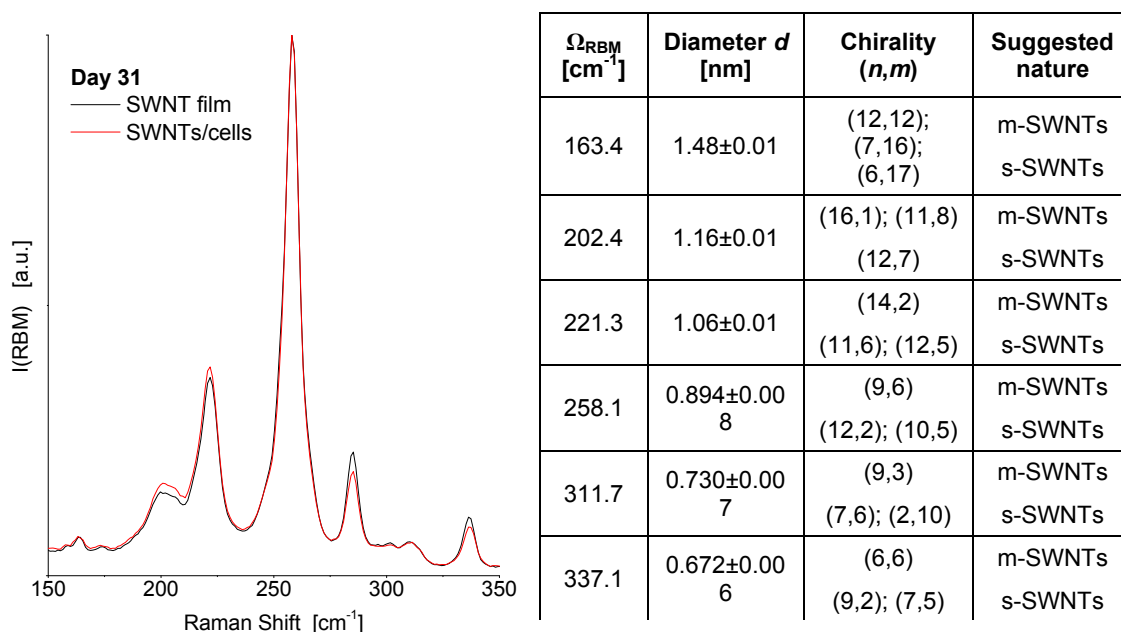


Figure 2.5. Raman signals ($\lambda_{\text{exc.}} = 633 \text{ nm}$) in the range of RBM mode (150-350 cm⁻¹) showing that both *m*-SWNT and *s*-SWNT are present in about the same ratio in the SWNT bundles after 31 days of cell exposure.

(*m*-SWNT) and/or semiconducting (*s*-SWNT) nanotubes engaged in the cell implantation, additional Raman spectra were collected in the range of the RBM mode. Previous investigation on chemical reactivity of SWNTs showed that *m*-SWNTs are more chemically reactive than *s*-SWNTs [81]. When selective reaction of *m*-SWNTs takes place, resistance will naturally increase because of selective elimination of conduction pathways through the *m*-SWNTs; concurrently a simultaneous increase in $I(D)/I(G)$ ratio and disappearance of the RBM bands related to *m*-SWNTs have been observed [81]. Figure 2.5 compares representative Raman spectra ranging from 150 to 350 cm^{-1} of pristine SWNTs with Raman spectra of the SWNT film exposed to the cell culture for 31 days. Diameter, chirality and suggested metallic nature of the SWNT were also calculated (inserted table in Fig. 2.5) according to the well known relationships [23, 97, 98]: $\omega_{RBM} = (214 \pm 2)/d + (18.7 \pm 2)$ and $(d\pi/a_0)^2 = n^2 + nm + m^2$, where d is the diameter of each individual SWNT, n and m are the indices of the nanotube chiralities and $a_0 = 0.2461$ nm. It appears clear from the matching overlap of the two spectra in Fig. 2.5 that no significant changes in the intensities of the RBM modes have occurred due to SWNTs-cells interaction indicating that both *m*-SWNTs and *s*-SWNTs remain in the same ratio and no selective reaction occurred during cell implantation.

A direct method to investigate the chemical transformation of SWNT films after exposure to the cell/biological media system is FTIR spectroscopy. The pristine SWNT film shown in Fig. 2.6 is characterized by very weak transmittance bands, however it is possible to distinguish a peak around 1640 cm^{-1} due to benzene derivative stretching related to the activated C=C modes [95] and a prominent broad band at 3430 cm^{-1} which is assigned to contributions from a variety of O-H stretching modes [95]. When the

SWNT film is exposed to the cell/biological media system, new peaks appear at 1087 cm^{-1} , 1423 cm^{-1} and 2046 cm^{-1} ; at the same time the transmission bands at 1640 cm^{-1} and 3430 cm^{-1} noticeably increase. The new absorption peak at 1087 cm^{-1} can be assigned to appearance of ortho-disubstituted benzene ring while the peak at 1423 cm^{-1} can be due to the formation of new covalent bonds of the type $\text{C}_{\text{aromatic}}\text{-CH}_3$ and $\text{C}_{\text{aromatic}}\text{-CN}$ [91]. The broad peak centered at 2046 cm^{-1} has been observed in many cases during the adsorption of CO on different porous materials and catalysts [120]. The dependence of the absorption properties and selectivity of the absorbents on the different pore structure and

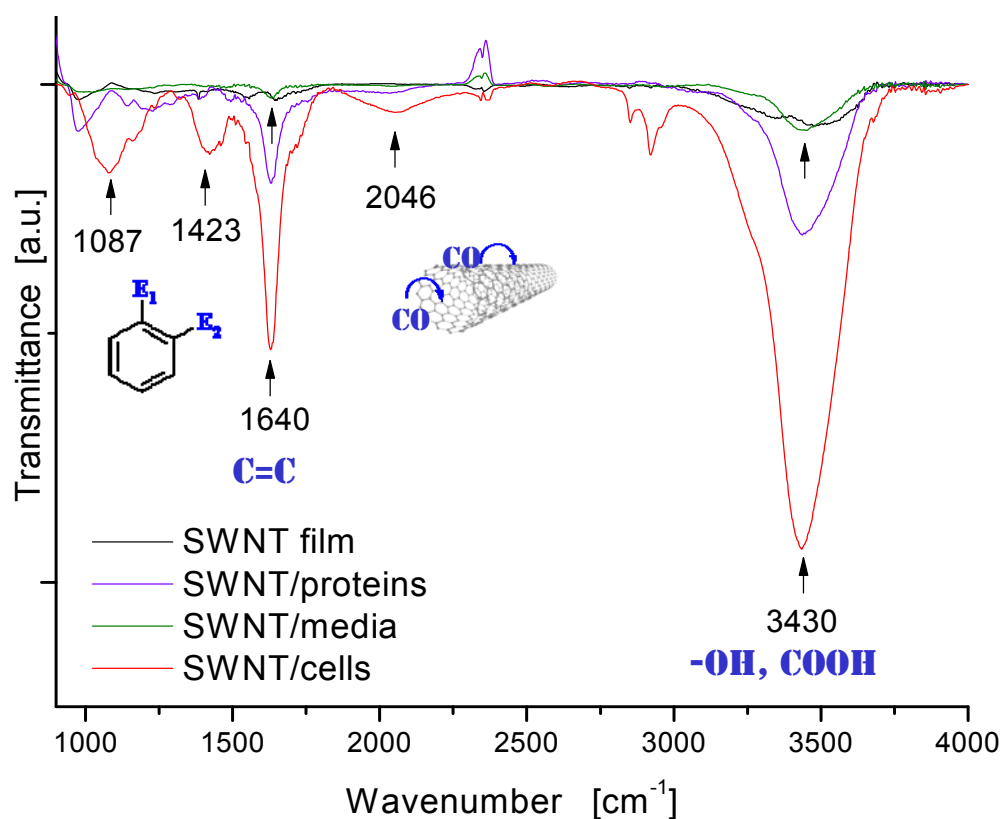


Figure 2.6. FTIR spectra of the SWNT film as deposited (black line), SWNT film exposed to biological media only (dark green line), SWNT film exposed to proteins (purple line) and SWNT film used for implantation of living cells (red line). All data were collected after 1 day of exposure to the cell/biological media systems. Sharp peaks in the range $(2320\text{-}2360\text{ cm}^{-1})$ and $(2850\text{-}2900\text{ cm}^{-1})$ arise from the background.

pore size distribution of the carbon nanotubes explains the broad shape of this new peak [95]. The increasing band at 3430 cm^{-1} can be explained by assuming that the defective points in the SWNT structure were passivated by hydroxyl (OH) and carboxyl (COOH) groups [107].

FTIR analysis indicates that a covalent functionalization of SWNTs has occurred within the first 24 hours after cell implantation due to the interaction of the films with the living cells. The effect of the biological medium used for culturing the biocells appears to be negligible (dark green line in Fig. 2.6) if compared with the variation of the bands for the SWNTs after cells implantation (red line in Fig. 2.6). Chemical reactions can take

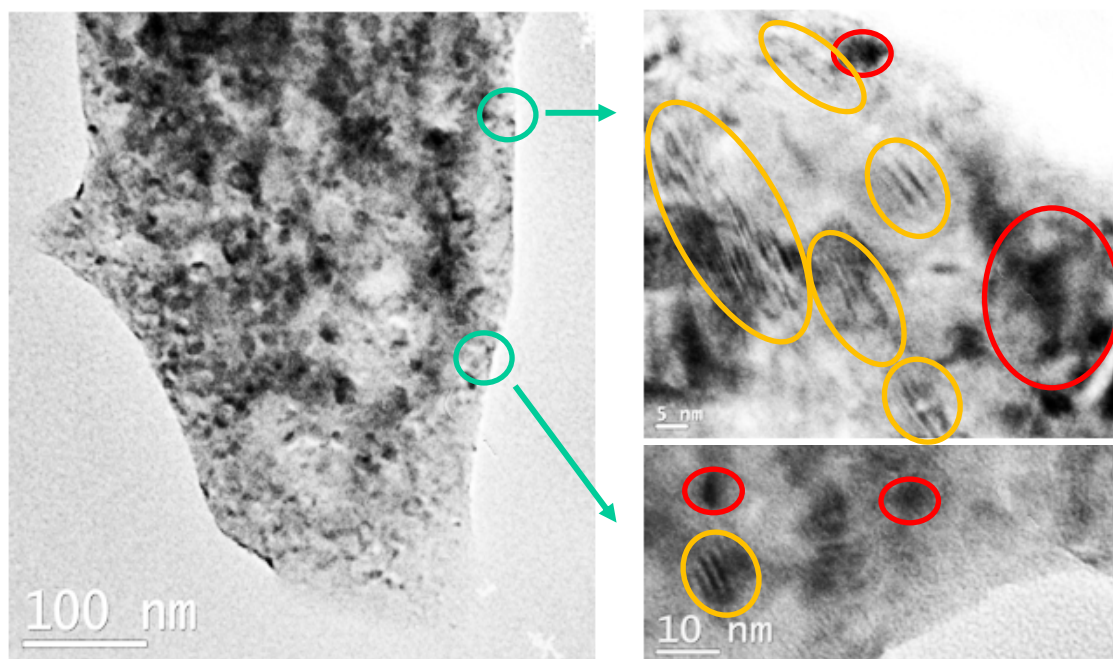


Figure 2.7. TEM images showing a superficial flake of the SWNT film used for cell implantation (the picture has been taken at day 15 from cells implantation). Close up view shows an entanglement of SWNTs and cells (bright areas). SWNT features (yellow circles) and evidence of SWNT uptake by the cells (dark spots inside the red circles) are also visible, indicating a good adhesion between growing cells and the SWNT substrate.

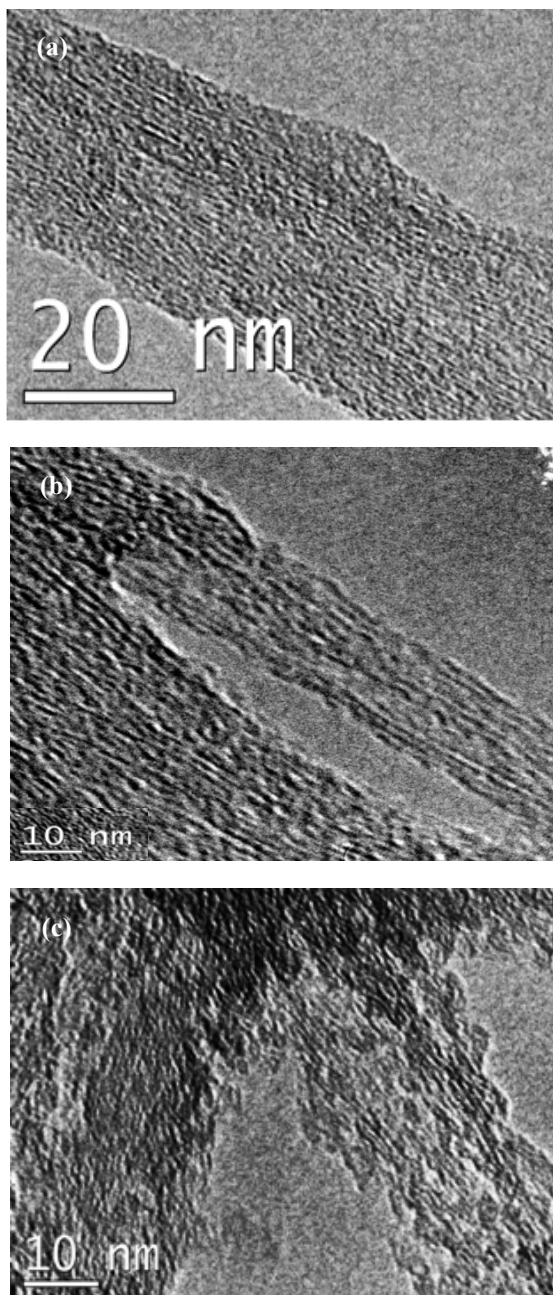


Figure 2.8. High resolution TEM images of (a) pristine SWNT bundles, (b) SWNTs exposed for 15 days to biological media only used as control and (c) SWNTs exposed for 15 days to cell/biological media system. SWNT bundles used for cell implantation clearly show severe wall damages; the “sharkskin” surface indicates a slow degradation of the SWNTs with the exposure time. Localized mechanical stress induced by the push-pull action of the living cells and superficial covalent functionalization of SWNTs due to bio-chemical interaction (cellular respiratory mechanism) are among the causes of such degradation.

place either on the sidewall or on the ends of the nanotubes involving mostly defect sites such as open ends, holes in the sidewall (missing carbon atoms), pentagon and heptagon irregularities in the hexagon graphite network, etc.

TEM images representative of the top layer of a SWNT film after cell implantation show a strong interaction between cells and SWNTs (Fig. 2.7) indicating a

good adherence and uptake of carbon nanotubes by cultured osteoblast cells. In the close up view in Fig. 2.7, SWNT bundles with diameters of 5-10 nm (marked with yellow circles in Fig. 2.7) are still visible behind the cells and the extracellular matrix (bright areas in Fig. 2.7). The red circles point at dense black mass of material with few structural features which represent SWNT uptake by the cells. Several studies [57, 89, 121] have already demonstrated carbon nanotubes uptake and transport inside the cells via a time-temperature dependent mechanism.

Higher resolution images of SWNT bundles dispersed and sonicated in aqueous SDS solution clearly show extensive damages to the sidewall of the SWNTs exposed to cell implantation for more than two weeks (Fig. 2.8c). The “sharkskin” wall surface is probably the effect of the strong biochemical and mechanical action of the living cells on the SWNTs skeleton, such as the citric acid cycle (Krebs cycle) involved in the cellular respiratory mechanism and the push-pull forces exercised by the cells during their movement and size growth. No structural changes were observed in control SWNT bundles exposed to the culture medium only; SWNT bundle walls in Fig. 2.8b appear smooth and straight, similar to the pristine SWNTs shown in Fig. 2.8a.

CHAPTER 3

STRUCTURE AND PROPERTIES OF BORON CARBIDE

Carbon-based structures are studied in much more detail compared to boron-based structures. Lately, there has been an increased scientific interest and a rapid development of novel $B_xC_yN_z$ hybrid materials [122]. Specifically, our research will focus on B_xC_y structures whose characteristics change with the ratio of constituents. We aim at the goal of better understanding the physics and chemistry of the B_xC_y hybrid material called boron carbide.

Boron carbide was discovered by chance in the process of fabrication of metal borides in the second half of the XIX century. It was synthesized for the first time in electrical furnace [123-125]. Since then, boron carbide has been synthesized by different fabrication procedures and from different starting materials, resulting in a wide range of compositions which lead to different mechanical and optical properties [126].

3.1 Boron carbide atomic structure and phase diagram

The crystallographic structure of boron carbide is very unique. An ideal crystal with B_4C stoichiometry would consist of an arrangement of distorted B12 icosahedra located at the nodes of a rhombohedral Bravais lattice ($R\bar{3}m$ space group, Fig. 3.1) [127]. This is a modification of the α boron structure which contains one B12 icosahedron per unit cell. The three atom C-C-C chains in the B_4C structure would link B12 icosahedra along the (111) rhombohedral axis [128]. Two different crystallographic sites exist in the B_4C structure called polar and equatorial sites. The six atoms forming the top and bottom

triangular faces of the icosahedron sit at the polar sites and are directly linked to atoms in neighboring icosahedra. The other six corners of the icosahedron form a hexagon in the

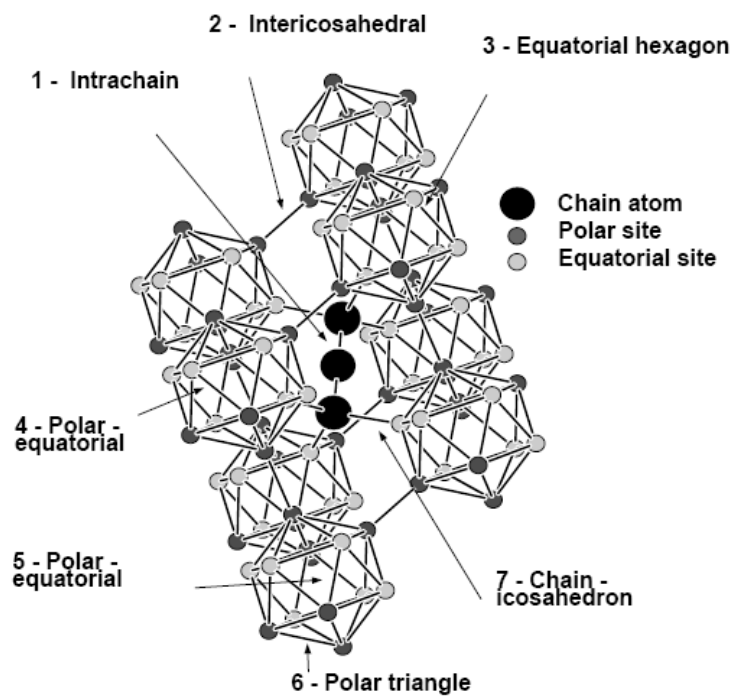


Figure 3.1. Atomic structure of B_4C .

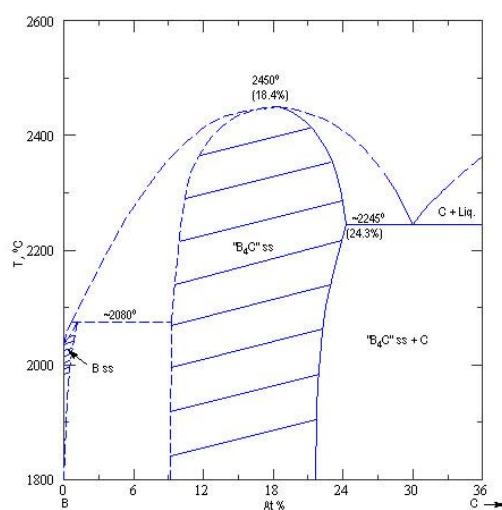


Figure 3.2. Boron-carbon phase diagram.

plane perpendicular to the [111] axis; their symmetry equivalent sites are called equatorial and are occupied by the remaining six atoms [129].

Boron carbide structure is stable up to very high temperatures within a large carbon concentrations range, from 8.8 to 20 at.% C, mainly due to the atomic similarity of boron and carbon atoms [126]. The phase diagram in Fig. 3.2 shows this wide phase homogeneity range. In addition, boron carbide melts congruently and forms a eutectic between carbon-rich compound and graphite at 26% C and 2400 °C. For the boron rich compounds, the existence of a peritectic transformation with a solid solution of carbon (<1 at.% C) in the β rhombohedral boron structure has been suggested [126].

3.2 Structural polytypism in boron carbide

Although the ideal B_4C crystal could be described by the $B_{12}(C-C-C)$ unit cell, the exact positions of the boron and carbon atoms in the B_4C structure have not been precisely determined [130]. Based on chemical analysis data and FTIR spectroscopy investigation [131], Kuhlmann *et al.* suggested that the carbon atoms are always available to substitute boron sites in the icosahedra leading to different structural elements (B_{12} and $B_{11}C$ icosahedra, C-B-C and C-B-B chains) in the boron carbide unit cell [132, 133], and even to chainless unit cells, depending on the C content.

In general, the stoichiometric formula of boron carbide can be written as

$$B_{12+n}C_{n-3} \quad (3.1)$$

where the position and the number n of the carbon and boron atoms in the icosahedra and the linear chain justify the existence of structural polytypism in BC.

The Gibbs free energy of boron carbide has been calculated to determine the

preferred sites for substitution and to understand the origin of the wide single phase region of the boron carbide [134]. More recent studies [129, 135] have shown that various BC polytypes most likely coexist at the same chemical composition and they are probably all thermodynamically stable.

Vast *et al.* [129] performed theoretical calculations for a single crystal B_4C structure considering only of three ordered configurations: the *chain* configuration, where all the icosahedra were constituted by boron atoms and the intericosahedral chain was C-C-C; the *polar* configuration and the *equatorial* configuration, where one of the boron atoms in the icosahedra was substituted by a carbon atom either in the polar ($B_{11}C_p$) or equatorial position ($B_{11}C_e$) and the three atom chain consequently was becoming C-B-C, inducing a small monoclinic distortion on the unit cells ($R\bar{3}m$ symmetry). Cells parameters were calculated within the density functional theory (DFT) and by minimizing the crystal energy with respect to the size, shape and degree of freedom of the

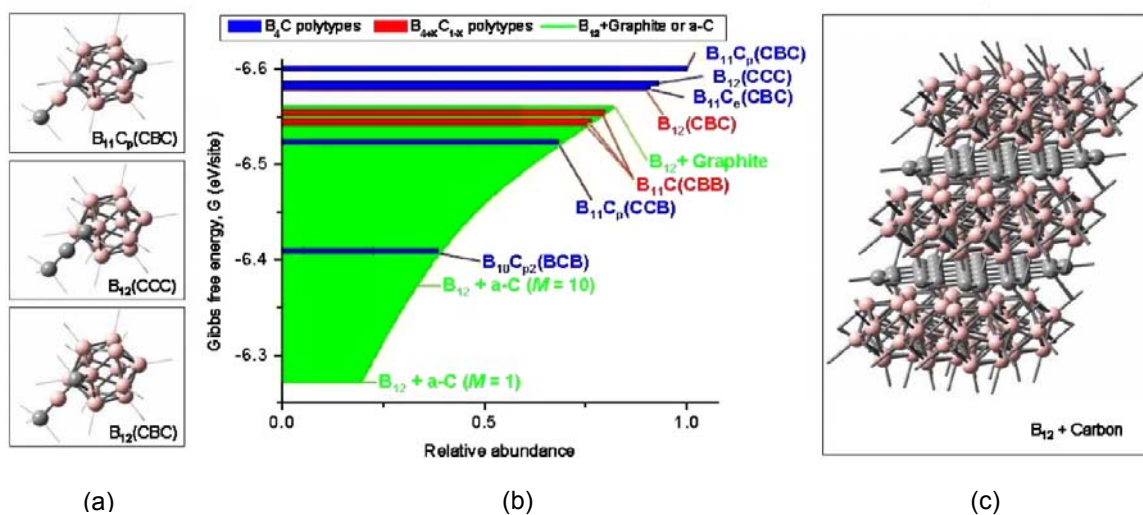


Figure 3.3. (a) Three structures showing the arrangement of icosahedra and chains corresponding to the stoichiometric polytypes $B_{11}C_p(C-B-C)$ and $B_{12}(C-C-C)$, respectively, and the most energetically favored non-stoichiometric polytype $B_{12}(CBC)$. (b) Gibbs energy versus relative abundance of the most significant polytypes. (c) Structure with segregated boron and carbon phase [135].

unit cell, but the bond lengths in polar and equatorial boron carbide were similar and it was not possible to discriminate between different configurations.

Fanchini *et al.* [135] performed Gibbs energy calculations for 20 different B_4C polytypes, showing that the most stable stoichiometric polytype is the polar $B11C_p(C-B-C)$. However, other polytypes, such as $B12(C-C-C)$, the non stoichiometric $B12(C-B-C)$, and a segregated structure consisting of boron icosahedra $B12$ and graphitic carbon, were also found to coexist within a disorder potential $\Delta V \approx 0.2$ eV (Fig. 3.3). Because the synthesis temperature of boron carbide ($T_s > 2000$ K) [136] involves kinetic energy ($k_B T_s$) comparable with the calculated energy range, the coexistence of the various boron carbide polytypes and the segregated boron-carbon phase is probably unavoidable.

3.3 Vibrational properties of boron carbide and graphitic carbon

The Raman spectra of boron carbides are characterized by a series of Raman bands extending from 200 to 1200 cm^{-1} [137-141]. In the literature, there are conflicting assignments [129, 138, 140, 142, 143] of the observed Raman peaks to vibrations of the principal structural elements in boron carbide, the icosahedra and the three-atom linear chains. It is generally accepted that the bands extending from 600 to 1200 cm^{-1} are mostly due to vibrations in the icosahedral units. However, the assignment of the low-frequency bands is highly dependant on the experimental conditions, in particular the quality of the samples and the excitation wavelength (energy) of the laser. The typical Raman spectra of single crystal B_4C as a function of excitation wavelength [141] are shown in Fig. 3.4.

The group of Tallant *et al* [137, 144] studied carbon isotope and carbon content dependencies of boron carbides using the 515 nm laser. They assign the two narrow

bands at $\sim 500\text{ cm}^{-1}$ to the vibrations within the soft C-B-C chains. The intensity of both bands diminishes progressively with the decrease in carbon content, which is attributed by the authors to the gradual replacement of C-B-C chains with C-B-B chains. At the same time, the two rather broad bands at $\sim 300\text{ cm}^{-1}$ decrease in intensity with decrease in C content, and a new narrow band at $\sim 375\text{ cm}^{-1}$ is appearing and becomes more pronounced in the low-carbon spectra, which the authors attribute to the appearance of B-B chains at very low carbon concentrations. Further, according to the authors, the dependency of the high-frequency bands on carbon isotope and carbon concentration suggests that carbon atoms are present within icosahedra at all compositions of boron carbides.

The group of Werheit *et al.* [143, 145-147] studied carbon isotope and carbon content dependencies of boron carbides using the 1070 nm laser. At this excitation wavelength, the two bands at $\sim 300\text{ cm}^{-1}$ become the primary feature of the Raman spectra (cf. the Raman spectrum acquired at 780 nm in Fig. 3.4). The authors assign these two bands to the librational modes (vibrations involving chain end atoms and the equatorial atoms of the icosahedra) in C-B-B and C-B-C chains, accordingly, based on an earlier model of Shirai *et al.* [142]. Although this assignment is arguable, the authors find that the intensity of the two bands at $\sim 300\text{ cm}^{-1}$ diminishes with decrease in the carbon content, in agreement with the observations of Tallant *et al.*

According to the first-principles calculations of Vast *et al.* [129], the two features at $\sim 300\text{ cm}^{-1}$ are not true Raman bands and are due to disorder-activated acoustic phonons. Indeed, the resonant nature of the two bands at $\sim 300\text{ cm}^{-1}$ is evident from the dependence of their intensity on excitation wavelength (Fig. 3.4). By comparison with the

experimental data, Vast *et al.* find that carbon substitutes boron in polar sites of the

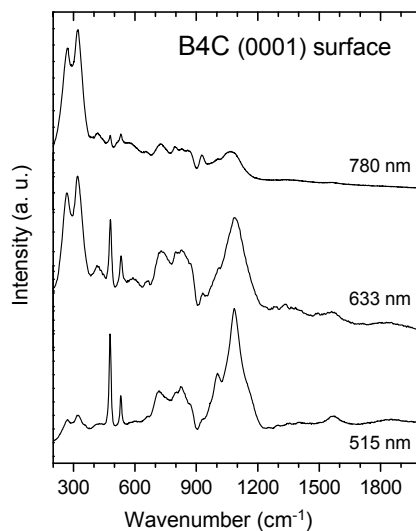


Figure 3.4. Raman spectra of single crystal B_4C , (0001) surface, taken at excitation wavelengths of 515, 633, and 780 nm [141].

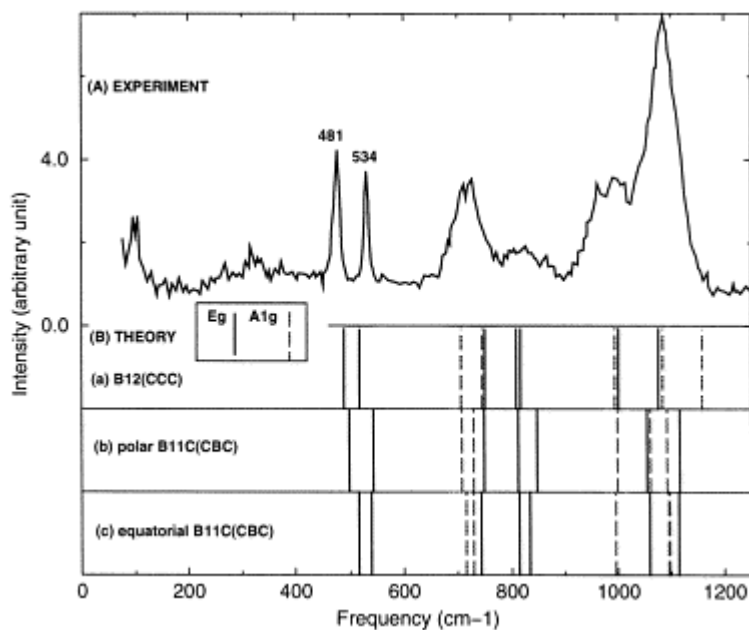


Figure 3.5. Interpretation of the Raman spectrum of B_4C - (A) experimental spectrum, (B) theory for (a) $B_{12}(C-C-C)$, (b) polar $B_{11}C_p(C-B-C)$, and (c) equatorial $B_{11}C_e(C-B-C)$ configurations. Solid lines: E_g mode; dashed lines: A_{1g} mode [129].

icosahedrons (Fig. 3.5). Further, the analysis of Vast *et al.* attributes the 498 cm^{-1} band to chain rotation perpendicular to the (0001) plane and the 542 cm^{-1} band to the librational mode of the icosahedron, as shown schematically in Fig. 3.6.

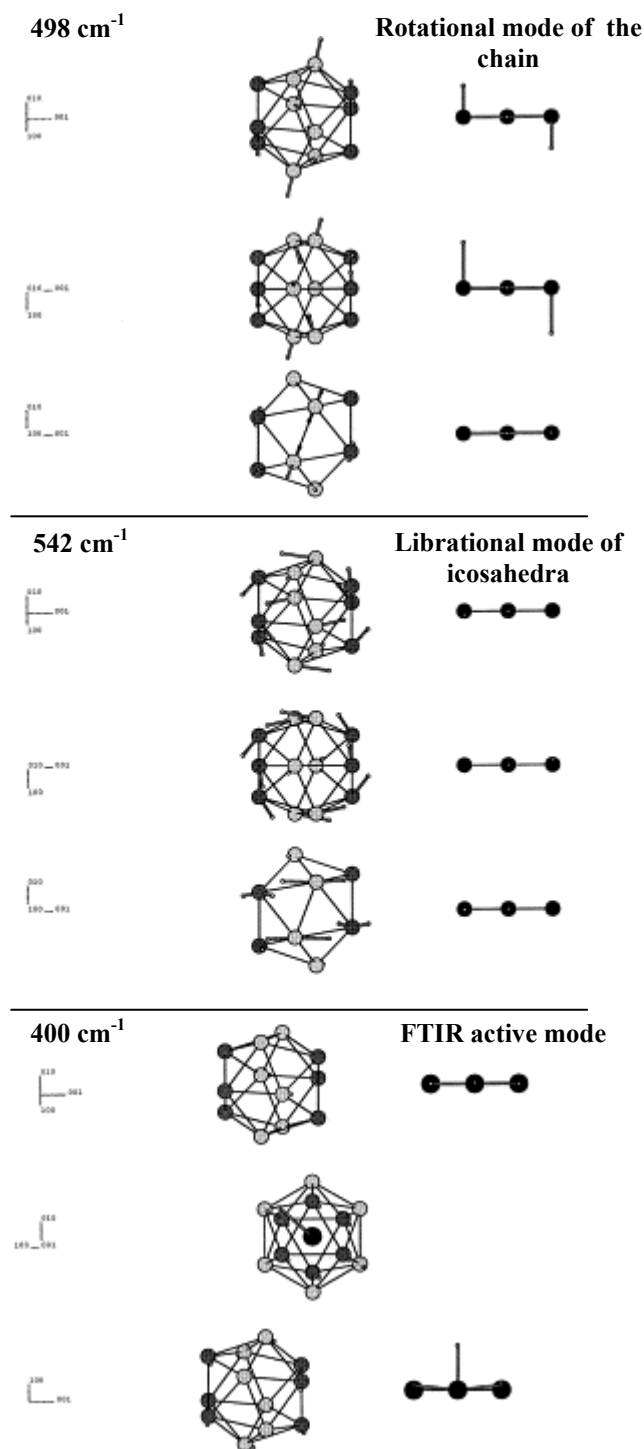


Figure 3.6. Low frequency mode of B_4C , due to the torsion of the chain – atomic displacements of the Raman active modes observed at 481 cm^{-1} (rotation of the chain of about one axis perpendicular to the $[111]$ direction) and 535 cm^{-1} (librational mode of the icosahedra), and of the infrared active mode observed at $\sim 400\text{ cm}^{-1}$.

The Raman spectrum of boron carbides at higher frequencies (from 600 to 1200 cm^{-1}) is characterized by a number broad peaks probably originated from the vibrations within the icosahedra [129, 137], however their nature is not very well understood yet. Correlation of theoretical and experimental results at higher frequencies becomes problematic due to the observed band broadening that might be attributed to structural disorder, twinning and stacking faults defects which are all present even in the single crystal [129].

The vibrational modes related to the carbon atoms are very important for analysis of free carbon present in the boron carbide. The nature of the Raman spectra of graphitic and amorphous carbon [148, 149] was theoretically investigated by Ferrari *et al.* [150]. A typical experimental Raman spectrum of amorphous carbon is shown in Fig. 3.7. According to literature, the graphite-like, also called tangential *G* band (1589 cm^{-1}), derives from the in-plane stretching vibration of the double C=C bonds (sp^2 carbon), and has E_{2g} symmetry. In the ideal case of a graphite single crystal (infinite graphitic domain), the *G* band is the only one to appear.

The disorder-induced *D* band ($\sim 1300\text{-}1360 \text{ cm}^{-1}$) is instead originated by the breathing vibrations of the aromatic 6-fold rings in finite graphitic domains (Fig. 3.8); it is forbidden in perfect graphite and only becomes active in presence of disorder. The mechanism responsible for the *D* band is the formation of an electron-hole pair caused by laser excitation and followed by one phonon emission. It has been proved that the *D* band always requires an elastic defect-related scattering process. It means that the *D* bands are observed in sp^2 carbons containing vacancies, impurities or other symmetry-breaking defects. In carbon materials, the *D* is known as the breathing mode of A_{1g} symmetry

involving a phonon near the K zone boundary. The *D* mode is dispersive because it is sensitive to the excitation laser energy E_{laser} .

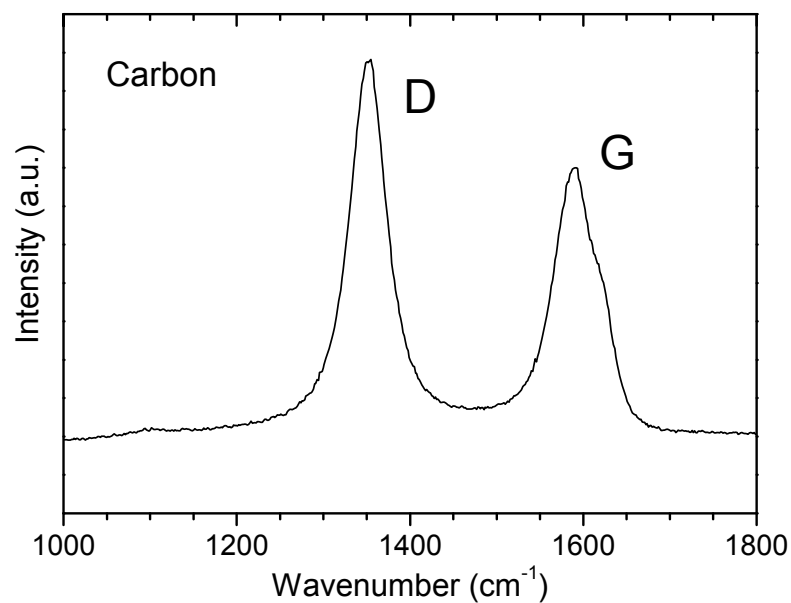


Figure 3.7. A typical Raman spectrum of amorphous/graphitic carbon showing characteristic *D* and *G* bands.

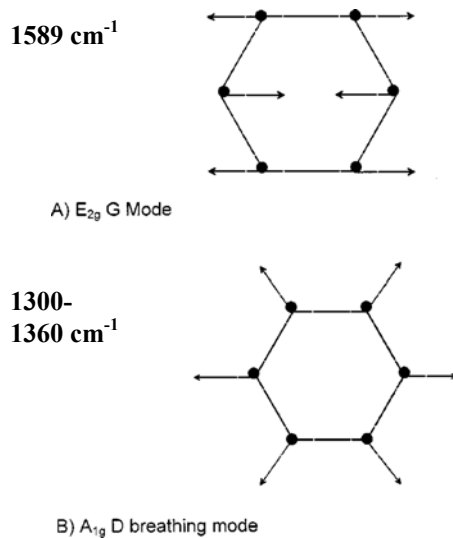


Figure 3.8. Carbon atoms motion in the (a) *G* and (b) *D* modes of vibration. Note that the *G* mode is due to the relative motion of sp^2 carbon atoms and it can be found in the chain as well.

Tuinstra and Koenig noted that the ratio of the intensity of the D band with respect to the G band varies inversely with the size of the graphitic clusters [151]:

$$\frac{I(D)}{I(G)} = \left(\frac{C(\lambda)}{L} \right) \quad L > 20 \text{ \AA} \quad \text{Tuinstra-Koenig} \quad (3.2)$$

$$\frac{I(D)}{I(G)} = \left(\frac{C(\lambda)}{L} \right)^{1/2} \quad L < 20 \text{ \AA} \quad \text{Ferrari and Robertson} \quad (3.3)$$

where the constant $C(\lambda)$ depends on the excitation wavelength (e.g., $C(515.5 \text{ nm}) = 40 \text{ \AA}$) and L is the diameter of the sp^2 domain. Tuinstra-Koenig relationship is suitable for micro- and nano-crystalline graphite-like clusters larger than 20 \AA . More recently, Ferrari *et al.* [150] corrected this relationship for the smallest value of L taking in consideration that the D band is controlled by an increasing electron confinement at smaller L values.

It is interesting to note that the D band strength indicates disorder in a graphitic structure because it is proportional to the probability of finding 6-fold rings in the cluster, and instead in amorphous carbon the development of the D band indicates order, exactly opposite to the case of graphite.

3.4 Electronic and optical properties of boron carbide

Boron carbide, in comparison with other ceramic materials, possesses good electrical conductivity. The specific electrical resistance is of the same magnitude as that of silicon carbide and graphite ($0.1\text{-}10 \text{ Ohm}\cdot\text{cm}$). The electrical conductivity is highly dependant on the purity level; higher resistance must be expected for a very pure boron carbide. On the other hand, the electrical conductivity increases with temperature because of the semiconducting nature of boron carbide. The thermal excitation at higher temperatures can cause electrons to leave the upper-most filled band and enter the conduction band.

Already in 1953 Lagrenaudie established that boron carbide was a *p*-type semiconductor and estimated its band gap around 1.64 eV [152], much smaller than that for other semiconductor ceramic, i.e., SiC, which has a band gap of about 3 eV, and also showing an order of magnitude better conductivity than SiC. Moreover, boron carbide seems to become an intrinsic semiconductor at 1000 °C [126] and it can be used as high temperature semiconductor due to its extremely high melting point (2500 °C).

The relatively small band gap in BC is closely correlated with the boron to carbon ratio [153] and can be further reduced by doping with foreign element such as Al and Si. The electrical conductivity, similar to the density and the other properties, is dependent on the boron-carbon ratio; in particular, the dependence is not linear; electrical resistance decreases until it reaches a minimum at 5 at.% C and increases substantially thereafter until it reaches a maximum at 25 at.% C [126].

Finally, boron carbide has a very high degree of chemical inertness which allows its use in electronic devices intended for harsh chemical environment [126].

The unusual nature of boron carbide electrical properties is still not fully understood. Emin's group [154] explained the temperature dependence of boron carbide conductivity, its thermally activated Hall mobility and its unexpectedly large Seebeck coefficient ($\sim 200 \mu\text{V/K}$ at 300 K) by a bipolaronic hole conductivity model, where the charge carriers (namely the holes) form small polarons and move through the material by phonon-assisted hopping. A bipolaron is formed when a pair of electrons is added from the three-atom chain to the boron rich icosahedra completing the filling of the internal bonding and contracting the icosahedra. Such hops were suggested to be among carbon atoms in inequivalent sites both in the chain and in the icosahedra of the hypothesized

boron carbon structure described above.

However, more recently, other hypotheses supported by theoretical models and experimental data [155, 156] have been proposed, questioning the validity of the bipolaronic mechanism theory. It has long been suspected that the varying carbon concentration in boron carbides has an electronic origin. A detailed quantum chemical investigation of the structure and bonding of the boron carbide has been presented by Balakrishnarajan *et al.* [155], who analyzed the nature of the molecular orbitals corresponding to the B₁₂ icosahedra and the C-B-C chain in the most symmetric structure B₁₂(C-B-C) and the interaction among them, and studied the effect on the bonding of adding or removing an electron from the unit cell. Theoretical calculation showed that the addition of electrons expands the unit cell, elongating and weakening all the bonds. In particular the carbon atoms tend to change hybridization from sp^2 to sp^3 as the total molecular charge increases (from B₁₁C₂¹⁺ to B₁₁C₂¹⁻) [155]. Finally, Balakrishnarajan *et al.* studied how the bonding nature changes by varying carbon content, concluding that the partial substitution of carbon by boron atoms creates an inevitable disorder because it is entropically favored. The localization of the electronic states arising from the B/C disorder leads to the semiconducting nature of boron carbide throughout its entire compositional range [155, 157].

Further, Werheit reviewed the major part of the experimental evidence that contradicts Emin's theory on the conductivity mechanism in boron carbide based on the formation of bipolarons [156]. In particular, the fundamental assumption for the bipolaron hypothesis has been disproved and a new energy band scheme has been proposed (Fig. 3.9) based mostly on the optical observations that were able to confirm

experimental conductivity measurements. Werheit demonstrated [156] that the intrinsic structural defects in the boron carbide generate split-off valence states in the band gap, which exactly compensate the electron deficiency calculated for the hypothetical structural formula $B_{12}(C-B-C)$. However, in the real boron carbide structure close to the carbon-rich limit of the homogeneity range, certain compensation by structural defects takes place as well. Accordingly, after the valence band of these compounds has been completely filled by electrons coming from the $B_{11}C$ icosahedra as donors, a certain portion of excess electrons remains available for occupying acceptor sites in the band gap. These electrons are responsible for the hopping type conductivity. In addition to the hopping vacancy, Werheit considered also the Drude-type free carriers as responsible for the conductivity in boron carbide, and he also noted the possibility of the formation of

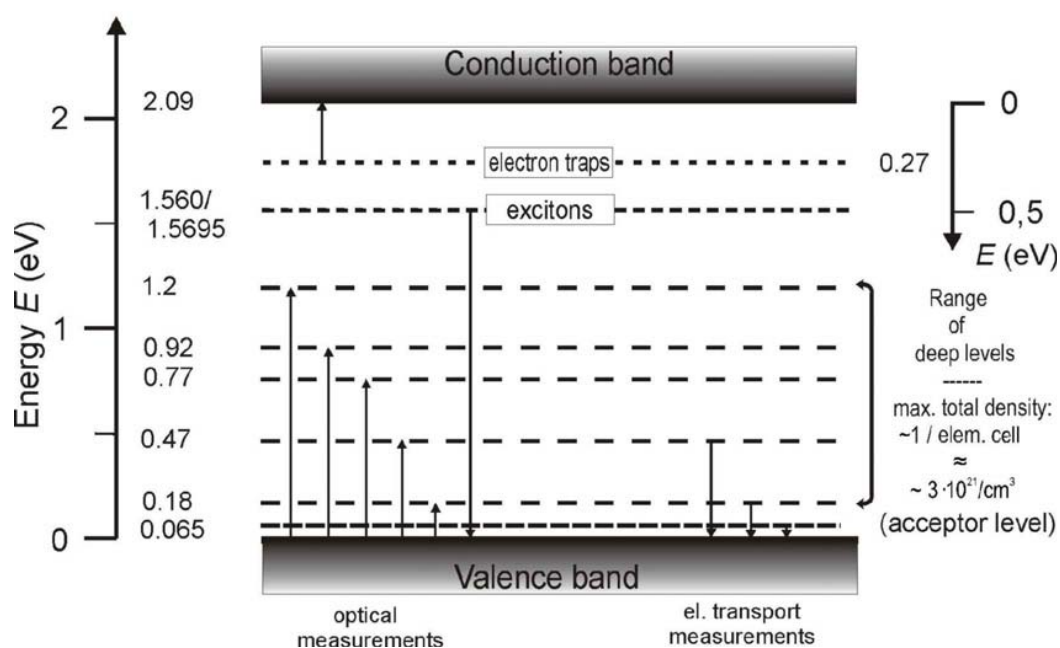


Figure 3.9. Energy band scheme of boron carbide based on optical absorption, luminescence and transport properties [156]. Left ordinate, energies related to the valence band edge; right ordinate, energies related to the conduction band edge. Arrows indicate the direction of the measured transitions.

excitons associated with the B atom in the C-B-C chain which would slightly change the binding energies.

The electronic transport mechanisms discussed above determine optical properties of boron carbide. In particular, the optical absorption of BC in the range of electronic transitions is very high. Figure 3.10 shows the absorption spectrum measured on a $B_{4.3}C$ single crystal by Werheit *et al.* [147]. Using decomposition of the absorption edge according to the theories of electronic transitions, two nondirect transitions (between a localized level in the band gap and a band) can be identified in BC, $E(1) = 0.76$ eV and $E(2) = 0.93$ eV. Further, four absorption bands have been identified below the absorption edge, specifically at 0.59, 0.65, 0.68, and 0.73 eV, most of which can be attributed to electronic transitions between localized levels above the valence band edge in the band scheme of BC shown in Fig. 3.9.

The comparison of the absorption coefficients in the low-absorption range below the absorption edge (technical boron carbide, $\alpha \approx 400$ cm⁻¹ [158]; hot-pressed dense

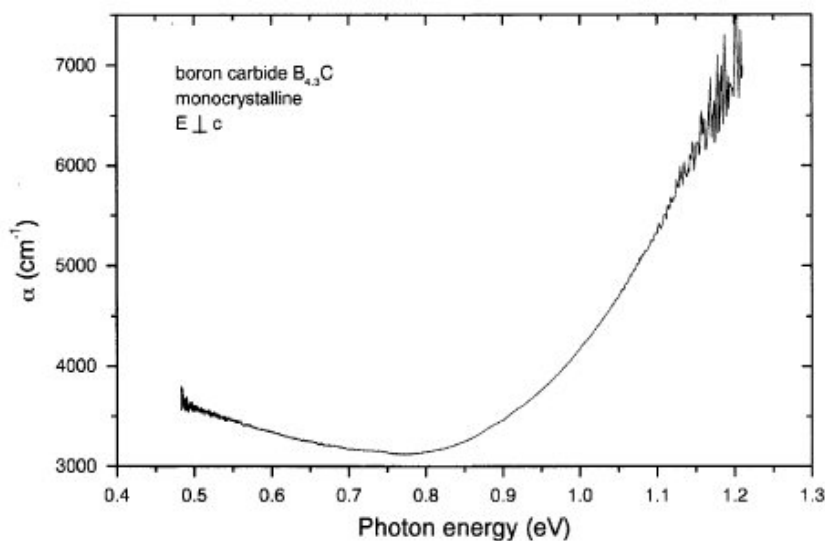


Figure 3.10. Absorption coefficient versus photon energy in $B_{4.3}C$ single crystal [147].

$B_{4.3}C$, $\alpha \approx 1300 \text{ cm}^{-1}$ [159]; high quality single crystal $B_{4.3}C$, $\alpha \approx 400 \text{ cm}^{-1}$ [147]) suggests that absorption increases with increasing structural perfection. Because absorption in BC is increasing toward lower energies, it can be attributed to the absorption of charge carriers, which usually increases with decreasing imperfections in the solid.

The photoluminescence spectrum of $B_{4.3}C$ single crystal, excited with an Ar-ion laser at 2.4 eV, is shown in Fig. 3.11. A distinct maximum in photoluminescence of boron carbide, identified at 1.563 eV, has been attributed to the indirect-allowed recombination of free excitons [160, 161].

Hardness was also found to be correlated with the stoichiometry [162] and bonding properties in BC, such as localization and delocalization, ionicity and covalence of the bonds and electron density in inter-atomic region [156]. In particular, higher

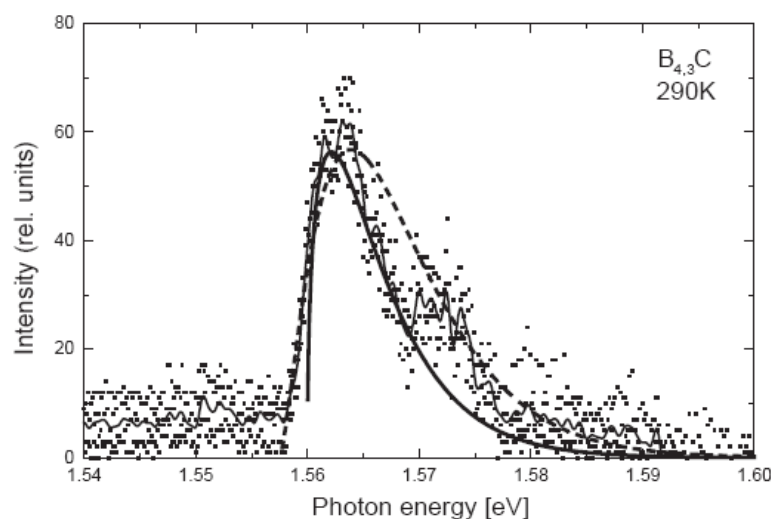


Figure 3.11. Photoluminescence spectrum of $B_{4.3}C$ single crystal at 290 K and 2.4 eV excitation energy [160]. Squares, experimental results; thin solid line, averaged experimental results; bold solid line, recombination model of free excitons; bold dashed line, model for the transition of electrons between energy band and defect level.

hardness is associated with more localized covalent bonds and higher inter-atomic electron density. There are four important bond types in boron carbide: (i) the highly delocalized intra-icosahedra sp^2 bonds, (ii) the π bonds originated by the inter-icosahedron sp hybrids, (iii) the double resonant bond with π characteristic in the three-atom chain ($C=B-C \leftrightarrow C-B=C$), and (iv) the bond between the C atom in the chain and the B atom in the icosahedra at the equatorial positions. It is important to note for future consideration that the incorporation of various dopants can dramatically affect the bonding and impact the physical properties of BC.

3.5 Mechanical and ballistic properties of boron carbide

There is considerable interest in the application of boron carbide as lightweight armor [163] due to its exceptional hardness, outstanding elastic modulus and low specific gravity (Table 3.1) [164, 165]. Mechanical testing under various loading conditions has been performed on boron carbide over the past 25 years [166, 167]. From the ballistic viewpoint, of particular interest is the response of BC to shock loading [168, 169].

A key parameter that determines the strength of a ceramic under shock loading is the Hugoniot elastic limit (HEL) [170]. The Hugoniot elastic limit corresponds to the maximum uniaxial dynamic stress that the material can withstand elastically. By definition,

$$\sigma_{HEL} = \frac{(1 - \nu_0)}{(1 - \nu_0)} Y \quad (\text{HEL}) \quad (3.4)$$

Table 3.1. Mechanical properties of boron carbide [126].

| Knoop hardness (GPa) | Wear resistance (a.u.) | Strength (MPa) | Toughness K_{Ic} (MPa $\cdot\sqrt{m}$) | Young's modulus (GPa) | Poisson ratio | Shear modulus (GPa) | Thermal shock resistance |
|----------------------|------------------------|----------------|---|-----------------------|---------------|---------------------|--------------------------|
| 29-35 | 0.4-0.422 | 300-500 | 2.9-3.7 | 360-460 | 0.17 | 158-188 | 210-260° |

where ν_0 is the Poisson's ratio and Y is the yield strength. The pressure experienced by the material can be expressed as $P=(\sigma_L+2\sigma_p)/3$, where σ_L and σ_p are respectively the longitudinal and transverse components of the stress tensor of a longitudinal shock wave propagating along the axis of the ceramic specimen. The dynamic response of a typical ceramic, with characteristic plastic yielding and HEL points, is shown schematically in Fig. 3.12.

Extensive analysis of shock profiles in different ceramic specimens such as Al_2O_3 , SiC and B_4C has been conducted by Grady [170]. Figure 3.13 shows a schematic representation of a reasonable physical model of the shear fracture process within the shock front of a ceramic under compressive stress. First, the specimen is subjected to a quick elastic shock reaching rapidly the HEL (in the high-strength ceramic, elastic stress of 2-20 GPa is reached with only 2-5% of shear strain), then, during the failure ramp the material quickly changes its elastic volumetric compressibility and finally, if premature failure does not occur, a drastic inelastic shear deformation and shear fracture growth begins.

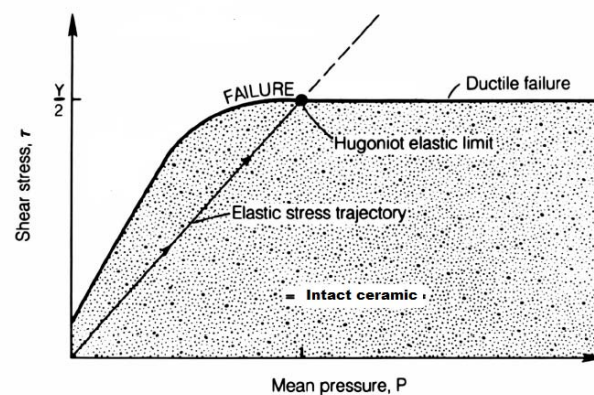


Figure 3.12. A typical dynamic response curve of a ceramic material showing plastic yielding and Hugoniot elastic limit.

Laboratory experiments reveal that the performance of boron carbide at high

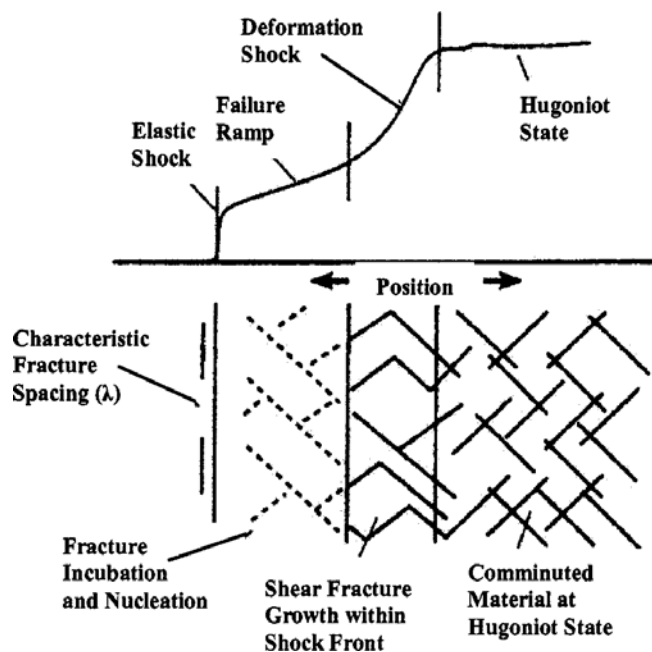


Figure 3.13. Representative shock compression profile in ceramic and schematic of brittle shear fracture process within the shock wave front.

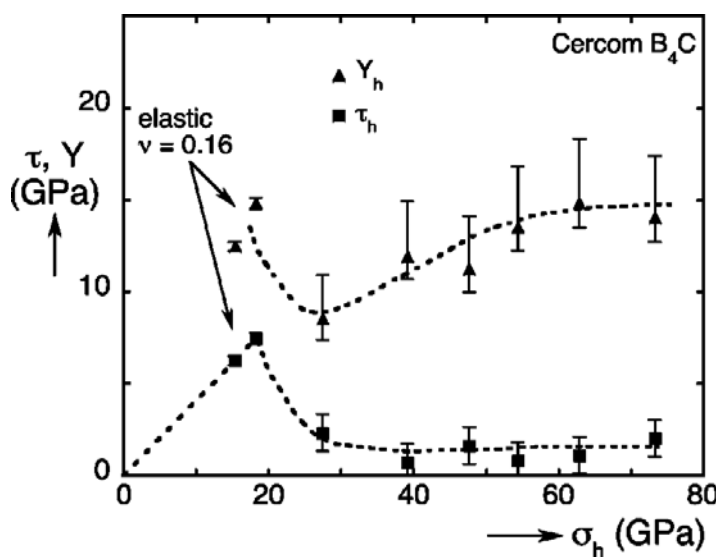


Figure 3.14. Shear stress τ_h and strength Y of boron carbide in the shocked state estimated from reshock and release experiments [171].

velocity and high pressure impacts is much lower than expected if one takes into account excellent static mechanical properties of BC (Table 3.1). The shear stress τ_h and shear strength Y of boron carbide in the shocked state are shown in Fig. 3.14 [171]. In contrast to a similar relationship in a typical ceramic material (cf. Fig. 3.12), the shear stress and strength in BC fall off rapidly above HEL, indicating premature failure of the material as the shock stress reaches a threshold value of 20-25 GPa. An identical abrupt drop in the shear strength of boron carbide at impact pressures of 20-23 GPa has been reported in ballistic testing, as illustrated in Fig. 3.15 [172].

The damage mechanism responsible for such failure has been assessed by Chen *et al.* [93]. High resolution transmission electron microscopy (HR TEM) analysis of BC

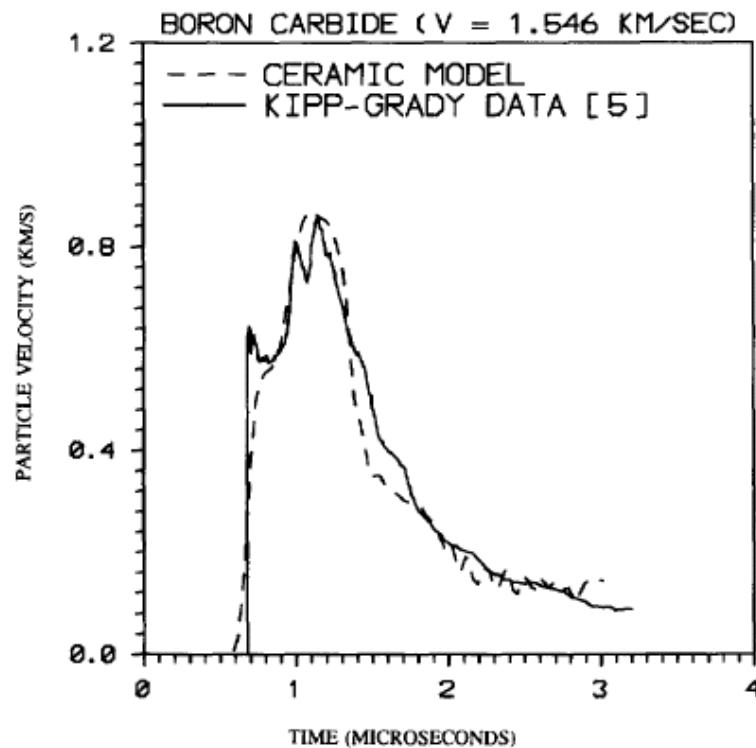


Figure 3.15. Ballistic data on BC showing an abrupt drop in shear strength at impact pressures of 20-23 GPa [172].

ballistic targets subjected to supercritical impact velocities and pressures (in excess of 20-23 GPa) revealed the formation of 2-3 nm wide intragranular amorphous bands that occur parallel to specific crystallographic planes and contiguously with apparent cleaved fracture surfaces (Fig. 3.16). At subcritical impacts, the amorphous bands were never observed; instead a relatively high density of stacking faults and microtwins suggested plastic deformation of the material under shock loading [93].

Pressure-induced amorphization of boron carbide has been previously reported in indentation [141, 173, 174] and scratching [173, 175] experiments. Figure 3.17 shows an example of a TEM observation of nanoscale amorphous bands and even larger amorphous areas within a Berkovich indentation in single crystal $B_{4.3}C$. This is corroborated by extensive Raman data collected on indented, scratched, and shock loaded boron carbide samples [173], as illustrated in Fig. 3.18. The main feature of the Raman spectra of amorphous BC is the appearance of high-frequency bands at 1330, 1520, and 1810 cm^{-1} . Spectral position of the 1330 and 1520 cm^{-1} bands and the dispersive

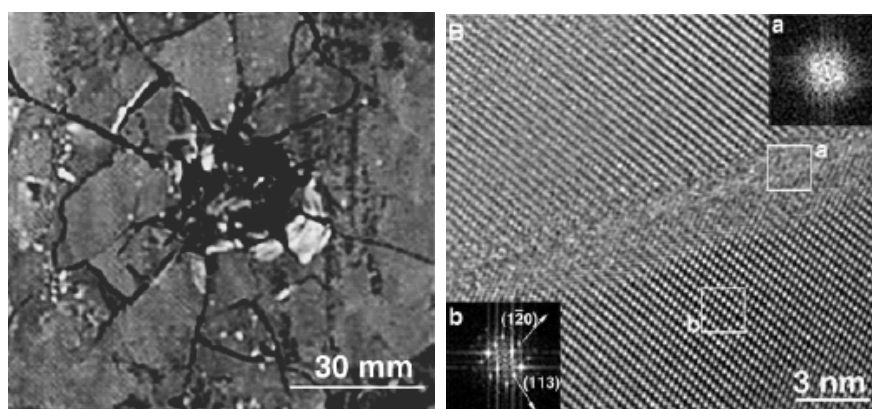


Figure 3.16. A boron carbide ballistic target that comminuted during impact (left) and a HR TEM image of a fragment produced by a ballistic test at impact pressure of 23.3 GPa (right) [93]. The lattice images on either side of the band correspond to the [1-101] direction of crystalline BC, and the loss of lattice fringes in the band indicates localized amorphization.

character of the 1330 cm^{-1} band [141], all suggest the similarity of these bands to, respectively, the *D* and the *G* band of carbon. Indeed, analysis of the temperature effect on the Raman spectra of indentations in BC [174] implied that amorphization of boron carbide may be mainly accomplished through the structural change of C–B–C chains, with the small amount of boron in the chains residing in the aromatic rings by substituting carbon, and the B₁₁C icosahedra remaining intact [176].

Until very recently, there were no confirmed reports on a high pressure phase transformation in boron carbide under compression in high pressure cells. A 2009 work

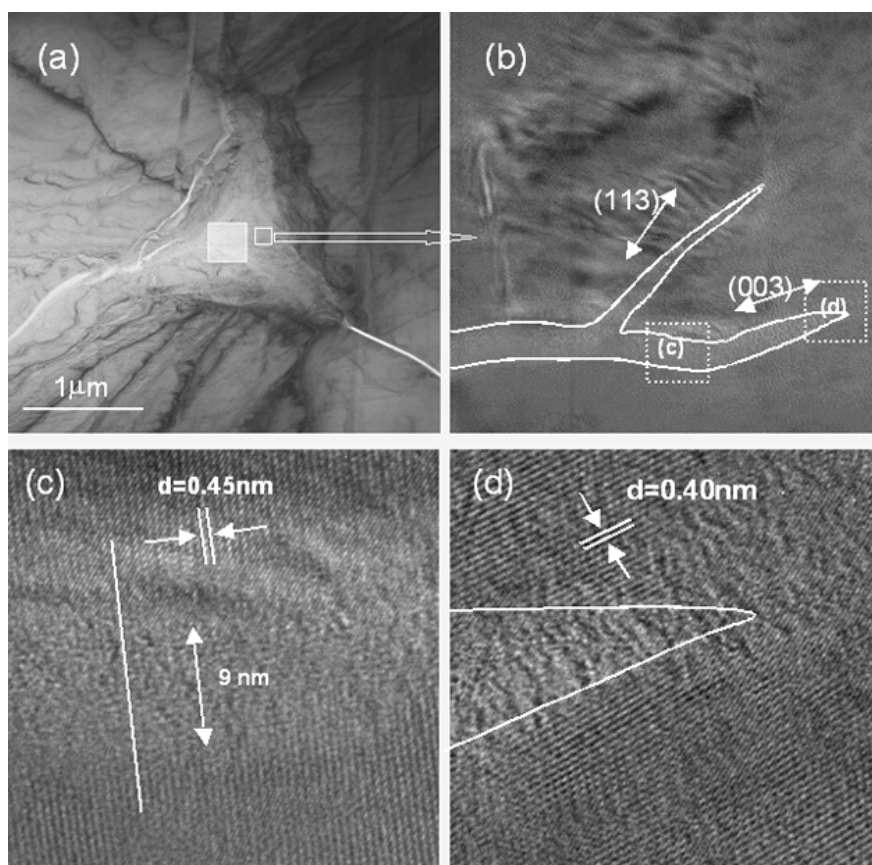


Figure 3.17. (a) Plan view TEM micrograph of a 100 mN Berkovich indent; (b) a magnified image showing the amorphous bands along the (113) and (003) planes; (c,d) HR lattice images corresponding to the boxed area in (a,b) [173].

of Yan *et al.* [177] addresses this issue. A complete set of experiments using quasi-hydrostatic and non-hydrostatic compression up to 50 GPa and subsequent depressurization were conducted on a boron carbide single crystal, and in situ Raman spectroscopy was engaged to detect possible high pressure phase transformations. It has been observed that the BC under quasi-hydrostatic condition remains perfect single crystal without visible surface relief and cracks. In situ and postmortem Raman did not detect any evident amorphization either during loading or unloading (Fig. 3.19). The results were significantly different when the single crystal was loaded and unloaded under highly non-hydrostatic pressure. In this case, the pressurized sample was found to break into a number of smaller fragments. Evident cracks, surface relief and shear bands with thin edges could be observed by optical microscopy (Fig. 3.20).

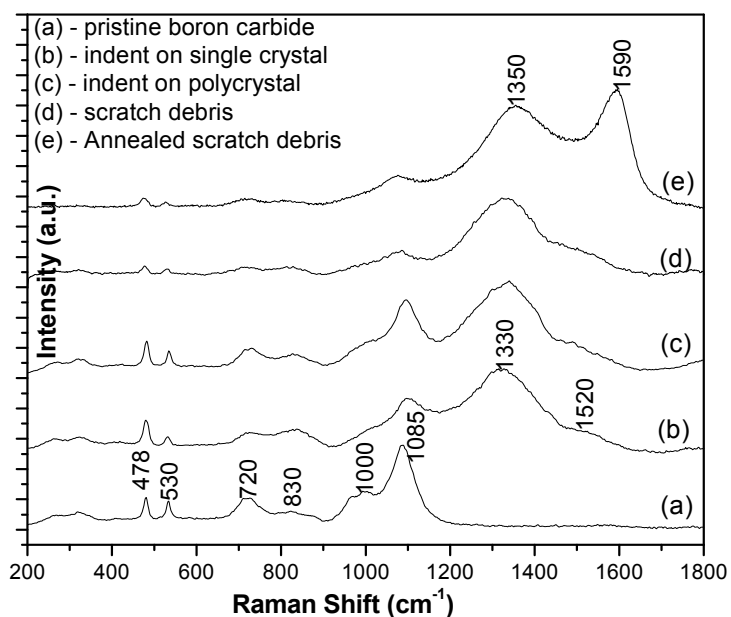


Figure 3.18. Raman spectra of (a) pristine single crystal $B_{4.3}C$; (b) indented single crystal; (c) indented hot-pressed polycrystalline sample; (d) scratch debris of a single crystal and (e) annealed scratch debris in air by using an argon ion laser with excitation wavelength of 514.5 nm [173].

This experiment indicates that non-hydrostatic stresses have by far a larger effect

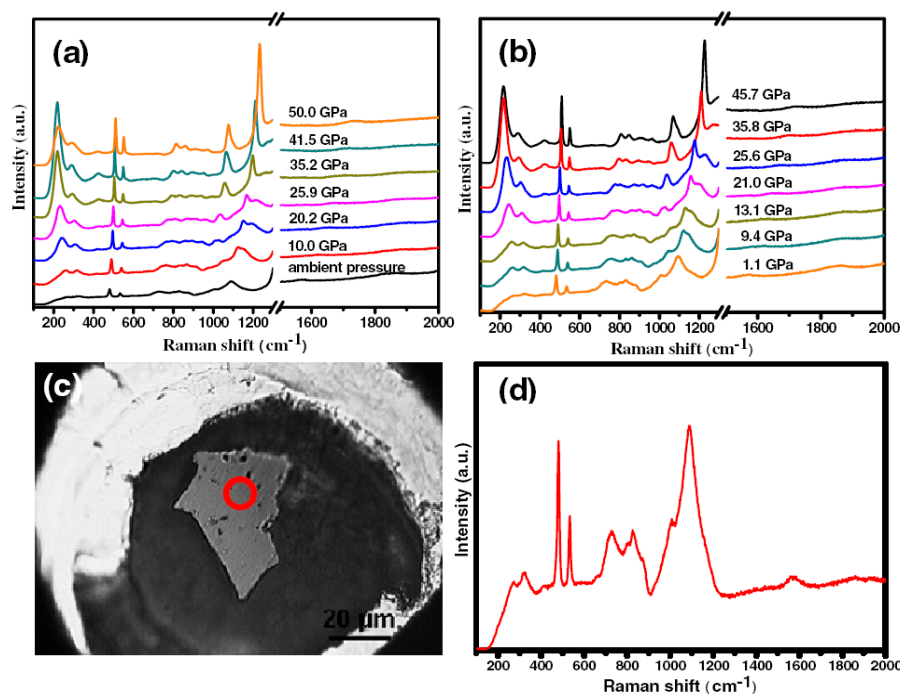


Figure 3.19. *In situ* Raman spectra of single crystal BC under quasi-hydrostatic compression during (a) loading and (b) unloading. (d) Raman spectrum of recovered material acquired from the marked region in (c).

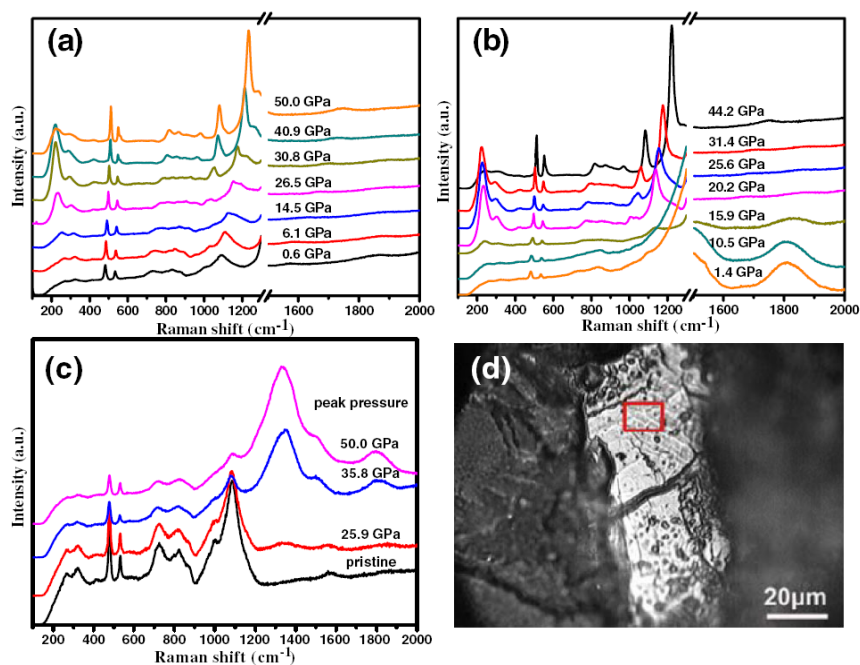


Figure 3.20. *In situ* Raman spectra of single crystal BC under quasi-uniaxial compression during (a) loading and (b) unloading. (c) Raman spectra of recovered material acquired from areas similar to the marked region in (d) [177].

on the elastic stability of boron carbide at high pressure. In particular, amorphous phase formation was detected by in situ Raman only during depressurization of uniaxially loaded samples (shift of the bands at about 1320 and 1500 cm^{-1} and formation of a new band at 1800 cm^{-1}). Theoretical simulations [177] indicated a drastic volume change of the hypothetical unit cell at destabilization pressure of 19 GPa (consistent with the HEL of 15-20 GPa) due to the bending of the C-B-C chain (Fig. 3.21). At higher pressures, the chain bends even more until the lattice of the B_4C single crystal is irreversibly distorted. It has been suggested that the central B atom of the chain bonds with the neighboring atoms in the icosahedra forming a higher energy structure. The release of this energy during depressurization is probably responsible for the collapse of the BC structure and the formation of localized amorphization [177].

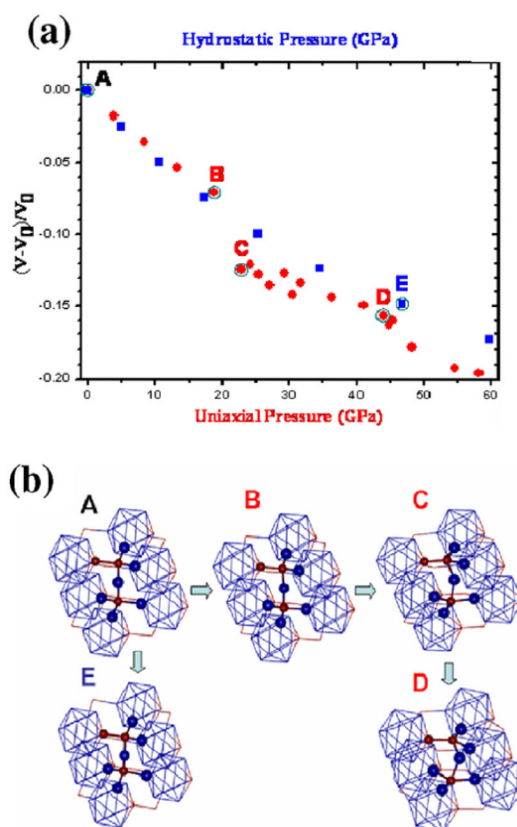


Figure 3.21. First principles simulation of the stabilization of $\text{B}_{11}\text{C}(\text{C-B-C})$ under hydrostatic and uniaxial compression [177]. (a) Compressed volume vs. pressure. The square data represent the volume change with hydrostatic pressure, and the circle data correspond to the volume change with uniaxial stress along the C-B-C atomic chain. (b) Atomic configurations of the B_4C unit cell at various pressures corresponding to data points in (a).

Theoretical investigation of phase stability in boron carbide polytypes at elevated pressures was conducted by Fanchini *et al.* [135]. The Gibbs' free energy for the considered boron carbide polytypes were calculated under increasing hydrostatic pressure at room temperature. The results showed that the energetic barrier for shock

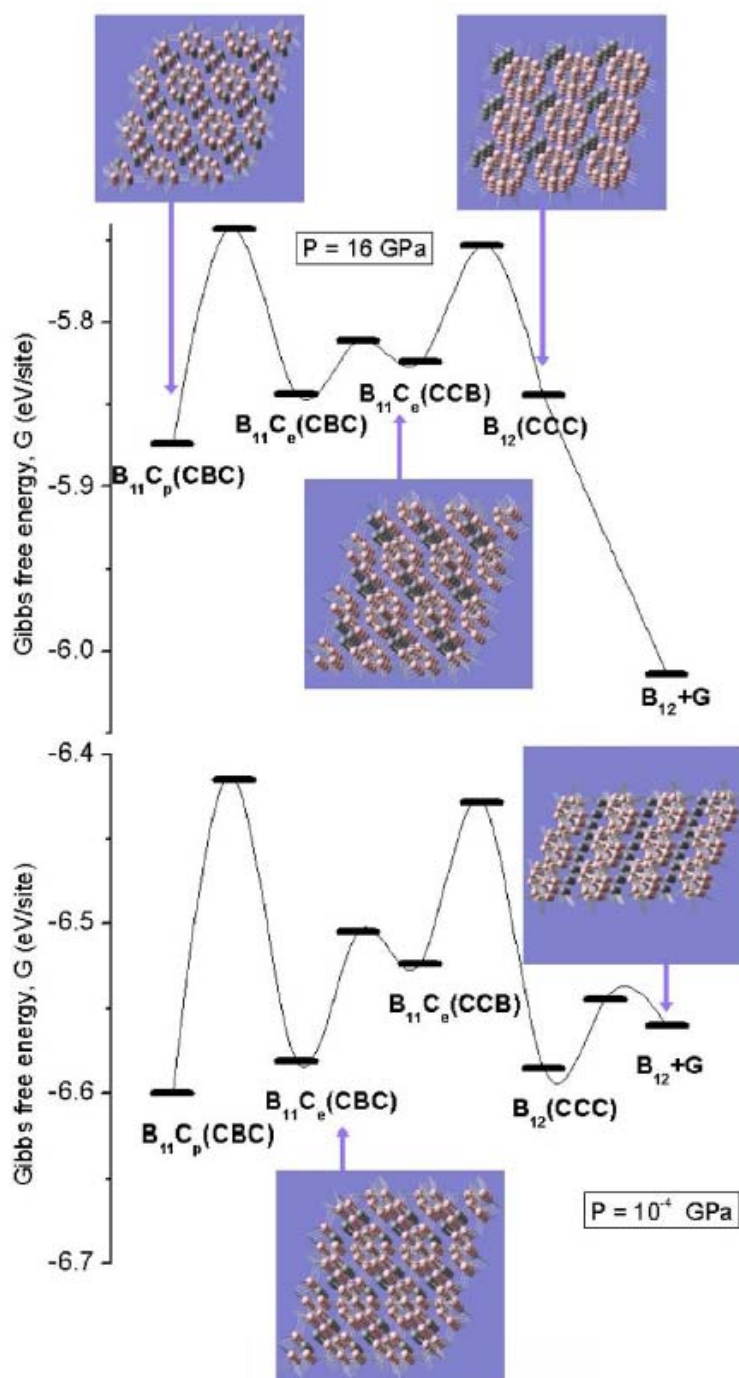


Figure 3.22. Diagrams of the steps proposed by Fanchini *et al.* [135] required to transform $B_{11}C_p(C-B-C)$ into B_{12} and graphite at 10^{-4} GPa and 16 GPa. The transformation steps involve migration of C atom in the icosahedron from a polar to an equatorial site [$B_{11}C_p(C-B-C)$ to $B_{11}C_e(C-B-C)$]; migration of the B atom in the chain from the central to a boundary site [$B_{11}C_p(C-B-C)$ to $B_{11}C_e(B-C-C)$]; swapping of the equatorial icosahedral C atom with the boundary B atom in the chain [$B_{11}C_e(B-C-C)$ to $B_{12}(C-C-C)$]; coalescence of the obtained (CCC) chains along the (113) planes, through a rotation of their axis around the [001] direction.

amorphization of boron carbide is by far the lowest for the B12(C-C-C) polytype, which was found to be unstable at 6-7 GPa during hydrostatic loading. The collapse of the B12(C-C-C) polytype leads to segregation of B12 icosahedra and amorphous carbon in the form of 2-3 nm wide bands along the (113) lattice direction, in excellent agreement with the previous transmission electron microscopy results [93]. An example of the most energetically favored transformation paths of B11C_p(C-B-C) polytype into B12 icosahedra and graphitic carbon is schematically shown in Fig. 3.22 for two different values of hydrostatic pressure.

Further detailed theoretical studies on the hardness of the BC structures were recently conducted [178]. Results show that although B11(CBC) phase of B₄C is the most stable and has the highest bulk modulus at atmospheric pressure the rhombohedral structure of B12(CCC) is by far the hardest. In addition novel hypothetically stable phases are proposed to explain conflicts among experimental results.

CHAPTER 4

FABRICATION OF THIN FILMS USING MAGNETRON SPUTTERING

4.1 Vacuum science and impact on films properties

Most thin film deposition techniques, with the exception of electro-chemical deposition, require either a vacuum or a kind of reduced-pressure environment. Vacuum science studies the kinetic theory of gases in rarefied state in terms of molecular velocity, contamination time, gas flow regime, etc. Evacuated spaces are usually populated by uncharged gas atoms and molecules, but in addition to these, electrons and ionized gas species are present in the more complex plasmas. In a closed system atoms and molecules undergo an animated motion but their concentration and pressure is uniform throughout because there is not a net flow of gas past any arbitrary plane in the system. If the system is opened by attaching pumps to it, net gas transport does occur even though individual gas molecules continue to locally execute the same random motion. With time however pressure gradients develop in the system as working chambers are evacuated to low pressures. Many limits occur to reach high vacuum level.

Here some milestones of the kinetic theory of gas are presented (for detailed analysis see [179]). Considering a motion of gas particles in a vessel, it is found that the number of collisions between molecules-molecules and molecules-wall of the vessel depends on the concentration or pressure of the gas. Under ideal hypothesis of rigid spherical gas particles, absence of repulsive and attractive forces, random motion and elastic collision, it is possible to evaluate the steady-state molecular velocity distribution by the well-known Maxwell-Boltzmann's formula:

$$f(v) = \frac{1}{n} \frac{dn}{dv} = \frac{4}{\sqrt{\pi}} \left(\frac{M}{2RT} \right)^{\left(\frac{3}{2}\right)} v^2 \exp\left(\frac{-Mv^2}{2RT} \right) \quad (4.1)$$

where $f(v)$ is the fractional number of molecules, n is the number of molecules per unit volume in the velocity range $v + dv$, M is the molecular weight and T the absolute temperature. The molecules cannot have neither zero nor infinite velocity, rather the most probable molecular velocity is realized at the maximum value of $f(v)$ and simply depends on the molecular weight of the gas particles and the temperature $\bar{v} = \sqrt{2RT}/M$.

Other important formulas describe the flow rate Φ of a gas escaping the vessel through a hole within a region where the pressure is zero and the rate (Φ_A) at which the particle leave the area A of the hole:

$$\Phi = 3.513 \times 10^{22} \frac{P}{\sqrt{MT}} \quad \text{Molecules/cm}^2 \cdot \text{s} \quad (4.2)$$

An issue of great importance when attempting to deposit or grow thin films in a very clean environment is how long it takes for a surface to be covered by a monolayer of gas molecules. The same concern arises during surface analysis of films, which is performed at very low pressures in order to minimize surface contamination arising from vacuum chamber environment. The contamination time is defined as the time required to cover a surface with 10^{15} atoms/cm², essentially the inverse of the impingement flux:

$$t_c = \frac{2.85 \times 10^{-8}}{P} \sqrt{MT} \quad \text{s} \quad (4.3)$$

A schematic of the ways the system affects gas density, mean free path, incidence rate, and monolayer formation time is displayed in Fig. 4.1.

The film properties strongly depend on the deposition conditions. It is possible to define at least four main factors [180] responsible for the quality and physical

characteristic of the deposited film: (i) Substrate surface condition before and after cleaning (surface morphology, roughness, surface chemistry and contaminants, presence of preferential nucleation sites, outgasing, surface stability, substrate mechanical properties, etc.); (ii) Deposition process and system geometry (angle of incidence distribution of the depositing flux, substrate temperature, deposition rate, gaseous contamination, concurrent energetic particle bombardment); (iii) Film growth on the substrate surface (condensation and nucleation of the arriving atoms, interface formation, flaw generation, surface mobility of the depositing atoms, growth morphology of the film, gas entrapment, reaction with the deposition ambient, changes in the film properties during deposition); and (iv) Postdeposition processing and reactions (chemical reaction of the film surface with the ambient, subsequent processing, thermal or mechanical cycling, corrosion, interfacial degradation, overcoating, etc.). In order to have reproducible films all these factor must be reproducible. Deposition rate together with deposition time determine the film growth and the total amount of deposited material.

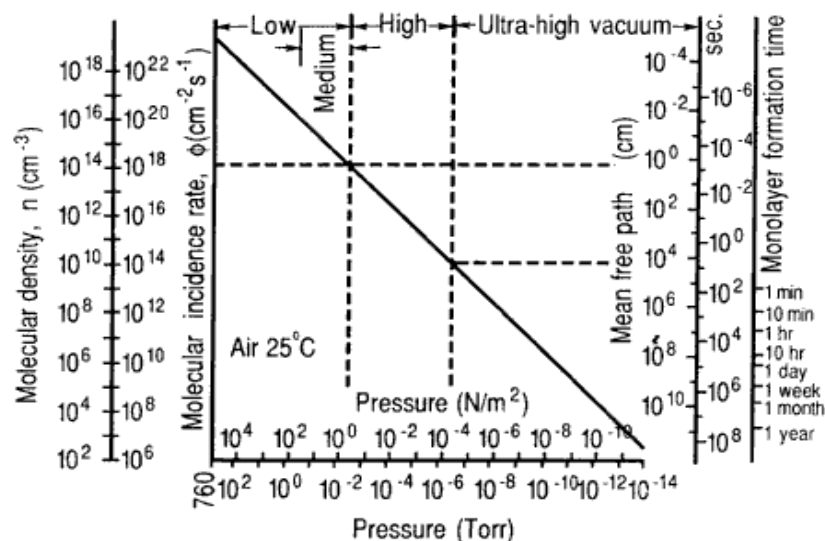


Figure 4.1. Density, mean free path, incidence rate, and monolayer formation versus pressure [179].

Specifically, the gas pressure greatly affects the stresses in the film; for example, if the pressure is low the film can have a high compressive stress while if the pressure is higher, the film can be under tensile stress [181]. Pressure is a very important parameter because it determines the thermalization of energetic particles in the system. It is possible to change the pressure during deposition by varying the gas flow rate; a high gas flow rate is often used for sweeping the contaminants from the chamber.

The substrate temperature can affect the film during deposition in different ways. In metal films, a large intrinsic tensile stress due to annealing and shrinkage of disordered material behind the advanced surface of the growing film has been observed. The magnitude of stress reflects the amount of disorder present on the surface before it is covered by a successive coating layer. Recrystallization of the film at high substrate temperature T_s occurs at a rate that follows the Arrhenius law:

$$r \propto \nu_0 \exp(E_r/RT_s) \quad (4.4)$$

where ν_0 is the vibrational frequency factor and E is the activation energy. The conclusion is that surface diffusion of vacancies most likely governs the temperature dependence of the film stresses by removing the structural disorder at the surface of the metallic film. On the other hand, for semiconductors, when the stress in the film arise, the thermally activated dislocations move through the material and exponentially increase in quantities, originating a rapid strain relaxation and creep formation with final drop of film stress.

The substrate temperature, as well as the substrate morphology, determines the nucleation and the condensation of the impinging atoms (Fig. 4.2) and hence the final film growth (Fig. 4.3). During nucleation, atoms condense on a surface loosing kinetic

energy and bonding to other atoms, and the preferential nucleation sites are lattice defects, atomic steps, impurities, etc. If the resulting atom-atom interaction is strong (metallic or electrostatic bonds), the surface mobility is low and each atomic surface can act as a nucleation site. The nucleation density (number of nuclei per unit area) has to be high in order to have dense films with a good contact with the surface. Before

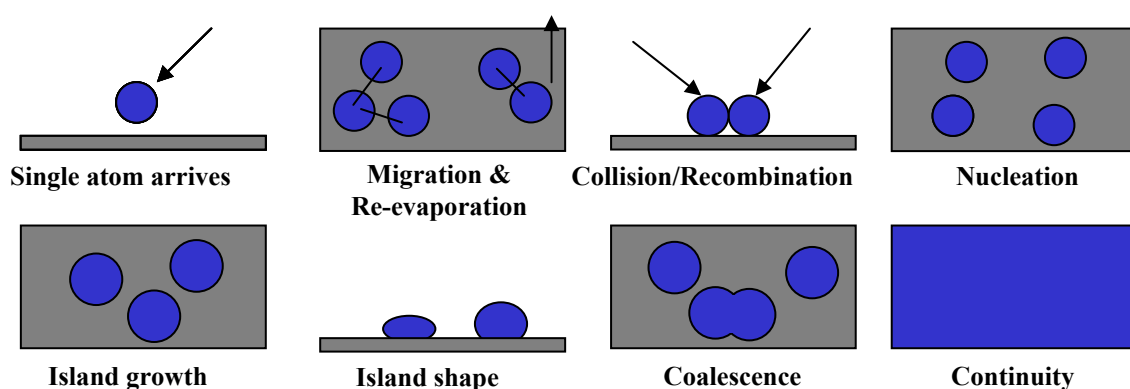


Figure 4.2. Schematic of a film growth process through island growth.

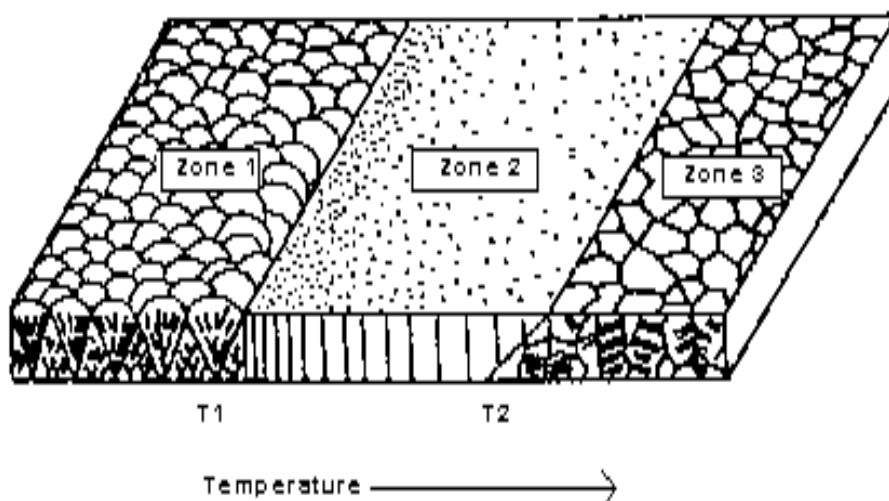


Figure 4.3. Effect of temperature and gas pressure on film microstructure. Porous structure (voids and crystallites), densely packed grains, columnar grain and recrystallized grain structure are observed.

coalescence, the nuclei can have a liquid-like behavior that allows them to rotate and align crystallographically, giving each other an oriented overgrowth. Agglomeration of nuclei occurs when the temperature is high enough to permit atomic diffusion and, if the interaction between impinging atoms and substrate is strong, the crystallographic orientation of the substrate will influence the preferential crystallographic direction of the nuclei [182]. If instead the deposition occurs with rapid quenching, bond saturation, limited diffusion and lack of substrate influence, the deposited material will be amorphous. Uncovered areas of the surface are called pinholes, and they can be created by geometrical shadowing during deposition or after deposition by lack of adhesion (pinhole flaking). Also, the angle of incident impinging atoms and the shape of the deposition source can affect the final physical and morphological properties of the coatings.

4.2 Sputtering deposition technique

Sputtering deposition technique is a physical vapor deposition process (PVD), in which the source of the depositing atoms is a surface (target) being sputtered. The sputtering is performed by applying a high voltage across a low-pressure gas (usually argon at about 5 mTorr) to create plasma, which consists of electrons and gas ions in a high-energy state. This is sometimes called a "glow discharge" process because the plasma emits a colorful halo of light (Fig. 4.4). During sputtering, energized plasma ions strike the target, composed of the desired coating material, and cause atoms from that target to be ejected with enough energy to travel to, and bond with, the substrate. For an efficient momentum transfer it is preferable to use gas with the same atomic weight of the target, so instead of

using argon it would be better to use neon for sputtering light elements and krypton or xenon for the heavy elements. Reactive gases can also be used to sputter compounds. The compound can be formed on the target surface, in-flight or on the substrate depending on the process parameters. The sputtered ions can ballistically fly from the target in straight line and energetically impact the substrate or the vacuum chamber causing re-sputtering. When the working pressure is higher, the ionized particles collide with the gas atoms and impact the substrate or vacuum chamber with lower energy. The entire range, from ballistic high energy impact to the low energy thermalized motion, is accessible by changing the background gas pressure. The resulting films from this atomistic deposition process can range from single crystal to amorphous, dense to less dense, pure to impure, thin (few atomic layers) to thick (several microns) coatings.

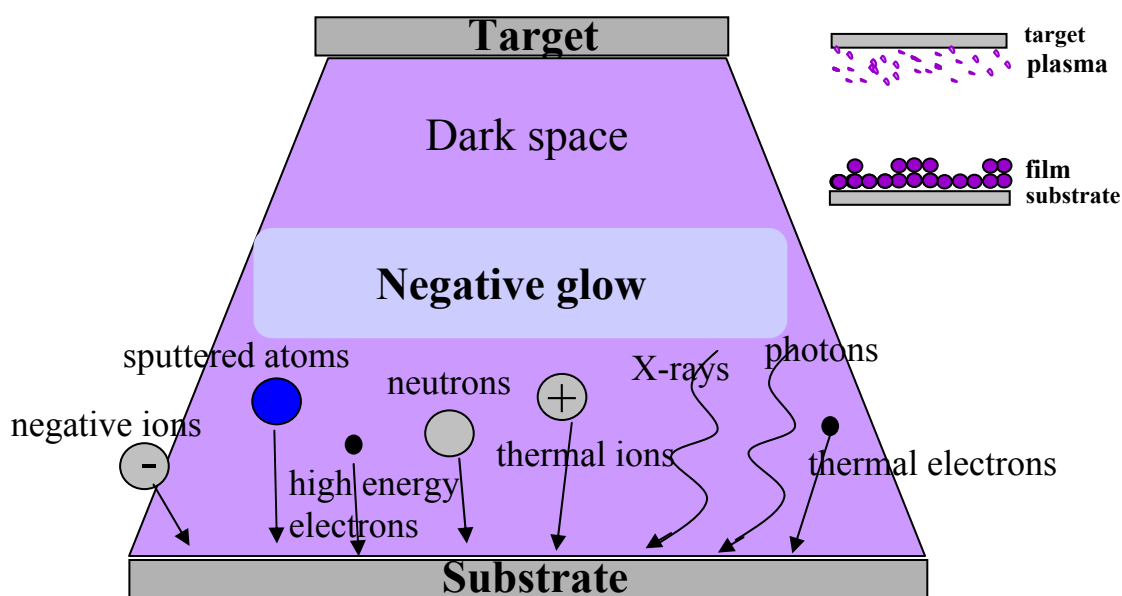


Figure 4.4. Schematic of energized plasma during sputtering (glow discharge). Upper insert shows a simplified model of film deposition.

The first sputtered deposition of films was reported by Wright in 1877 [180], and it was feasible because only a relatively poor vacuum is needed for sputtering deposition. However, this technique was not widely used in industry until the development of the vaporization source and the advent of the first planar magnetron sputtering with Chapin in the 1974 [180].

The physical properties of the sputtered films greatly depend on the chosen sputtering conditions such as substrate temperature, substrate bias, substrate morphology, working pressure, gas flow rate, etc. Unfortunately, it is impossible to control the plasma condition during sputtering and several critical situations can affect the quality of the deposition. For instance, contamination occurs very easily and cleaning procedures, such as cleaning the substrates and the chamber by pre-sputtering, are very important steps. It has been already mentioned that working with ultra high vacuum helps to reduce contamination problems. Plasma related contamination can be caused by desorption of water vapor, photodesorption, and heating of the surface due to radiation and recombination. Inert gases are generally used to desorb water vapor, and instead reactive gases such as oxygen and hydrogen are used to chemically react and volatilize contaminants such as hydrocarbons.

When high energy neutrals are reflected by the cathode or are formed by charge exchange process, sputtered contamination in undesired places can occur. Finally, it is possible that the contamination comes from the deposition system itself when radiant heating increases desorption of species from vacuum surface and material in the system. Contamination and water desorption can lead to the flake-off of the film build up.

Another relevant problem during sputtering deposition is the arcing effect. Arcs

can vaporize material and generate particulates in the plasma system. Arcing occurs when a potential difference has been established due to the plasma condition. Arcing is particularly severe when depositing electrically insulating and poorly conducting films, but it can be minimized using direct current (DC) or radio frequency (RF) power source.

4.3 Sputtering configurations

In the most common configurations of plasma-based sputtering, the positive ions present in the plasma are accelerated to the target which is at a negative potential with respect to the plasma. At low pressure, the ions reach the target surface with an energy given by the potential drop between the surface and the point in the electric field where the ion is formed. At higher pressures, the ions suffer physical collisions and charge exchange collisions so there is a spectrum of energies of the ions and neutrals bombarding the target surface.

The oldest sputtering method is the DC sputtering (Planar Diode configuration) where the cathode electrode is the sputtering target and the substrate is placed on the anode which is often at ground potential. The applied potential appears across a region very near to the cathode surface. To establish a cold cathode DC diode discharge in argon, the gas pressure must be greater than about 10 mTorr and the plasma generation region is about one centimeter in width. The mean energy of the bombarding species is often less than 1/3 of the applied potential [183]. Secondary high energy electrons come from the target and can bombard surfaces in the chamber resulting in heating which can be undesirable. The DC discharge can be sustained at high argon gas pressure that causes thermalization of the sputtered atoms which can be sputtered back. The cathode (target)

has to be conductive because an insulating surface would prevent the ion bombardment; moreover the high voltage could lead to arcing and harm the target.

An improvement of the DC sputtering has been obtained by applying an alternative current (AC) to the system. In this way the positive charge stays in the plasma zone and does not accumulate on the cathode, helping sustain higher voltages. In AC sputtering the potential on the target is periodically reversed. At frequency below about 50 kHz the ions have enough mobility so that a DC diode-like discharge can be formed alternatively on each electrode. The substrate, chamber walls or another sputtering target can be used as the counterelectrode. In asymmetrical AC sputtering, the counterelectrode is the substrate so the depositing film is periodically backsputtered to enhance film purity. This sputtering configuration is used mostly for insulating target, even though the deposition of the insulating film on the chamber walls can cause the anode area to change. A dual target configuration, where one clean target works as clean anode, can solve the “disappearing anode” effect.

At frequency above 50 KHz, the ions do not have enough mobility to allow establishing a DC diode-like discharge and the applied potential is felt throughout the space between the electrodes. The electrons acquire sufficient energy to cause ionizing collisions and thus the plasma generation takes place between the electrodes. RF frequencies used for sputtered deposition are in the range of 0.5-30 MHz. RF sputtering can be performed at low gas pressure (<1 mTorr). Since the target is capacitively coupled to the plasma it makes no difference whether the target surface is electrically conductive or insulating although for insulating target the sputtering rate is low. Another disadvantage in RF sputtering of a dielectric target is the possibility to fracture it if high

power levels are used. The reason why it happens is that most insulating materials have poor thermal conductivity, high coefficient of thermal expansion and are usually brittle.

By the application of a magnetic field in the sputtering system (magnetron sputtering) it is possible to form a dense plasma near the cathode at low pressures so that ions can be accelerated from the plasma to the cathode without loss of energy due to physical and charge-exchange collisions. This allows a high sputtering rate with a lower potential on the target than with the DC diode configuration. The most common magnetron source is the planar magnetron where the sputter-erosion path is a closed or elongated circle (“racetrack”) on a flat surface. The main disadvantage of the planar magnetron configuration is that the plasma is not uniform over the target surface. Therefore, the deposition pattern is dependent on the position of the substrate with respect to the target and also the target utilization is not uniform. The magnetic field in magnetron sputtering can be formed using permanent magnets or electromagnetics or a combination of the two; they can be arranged in different ways creating different magnetic field shapes and tunable current flow [184]. Another disadvantage of the magnetron sputtering is that the plasma is confined near the cathode and is not available to activate reactive gases near the substrate for reactive sputter deposition. This problem can be overcome by applying an RF bias to the cathode along with the DC potential, to generate plasma away from the cathode, or by having auxiliary plasma near the substrate surface. In general, it is called balanced magnetron, the configuration characterized by magnetic “lines of force” which remain close to the target surface so that the plasma is strongly confined to this area. Unbalanced magnetron instead is characterized by magnetic “lines of force” which extend further out of the chamber.

4.4 Experimental goals and research outline

This research aims at understanding properties and capabilities of boron carbide-based materials for many potential applications such as hard coatings and ballistic impact shields. Although boron carbide possesses the highest dynamic elasticity among ceramic materials, it shows an anomalous glass-like behaviour at high velocity impacts. The focus of our attention is to understand and adjust the mechanical response of boron carbide by investigating the chemistry, microstructure and morphology of boron carbide-based thin films. It has already been shown that the crystallographic structure of boron carbide films depends on carbon content [185].

Calculations [135] suggest that a specific polytype, B12(C-C-C), is responsible for failure of boron carbide at lower than expected impact pressure of 20-23 GPa. Further calculations showed that adding silicon to boron carbide eliminates the presence of the unwanted B12(C-C-C) polytype. In addition, a low concentration silicon doping would increase HEL of BC up to 40 GPa, one of the highest values ever found in solids, without changing the elastic constants of the pristine boron carbide. New theoretical simulations suggest that the Gibbs free energy of silicon-doped boron carbide is lower (energetically favored) than the energy of undoped boron carbide. These Si-containing BC phases are metastable and should be produced at experimental conditions far from equilibrium. The difference in Gibbs free energy between the B11C_p(C-B-C) and B12(C-C-C) polytypes with respect to the Si doped structures B11C_(1-y, p)Si_(y, p)(C-B-C) and B12(C-Si_yC_(1-y)-C) is shown in Fig. 4.5.

Cutting edge technology such as radio frequency magnetron sputtering has been

used for the synthesis of boron carbide-based films and then for incorporating Si as a dopant in the BC system. Even though thin film coatings are not very practical for armor applications, RF sputtering deposition allows us to achieve a non-equilibrium phase by creating B, C, Si plasma and an out-of-equilibrium quenching. In this way we plan to obtain Si-BC systems, which are metastable, without forming SiC by-products.

The composition, structure and physical properties of the thin films can be controlled by adjusting the plasma parameters, such as the RF power, substrate bias, substrate temperature and Ar pressure, distance between the target and the substrate [186-195]. These external parameters control the plasma properties such as ion charge state, ion flux and ion energy which will affect the type of BC phase condensed. Preliminary

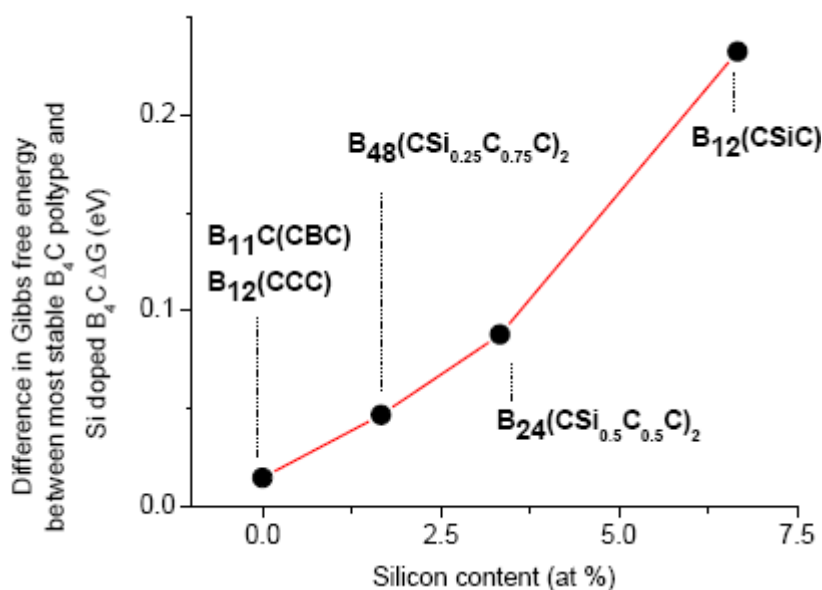


Figure 4.5. Gibbs free energy of the B₁₁C_p(C-B-C) and B₁₂(C-C-C) polytypes as a function of silicon atoms concentration. It can be observed that the difference in Gibbs free energy between the stable polytype, B₁₁C_(1-y,p)Si_(y,p)(C-B-C) and the most energetically favored minority polytype, B₁₂(C-Si_yC_(1-y)-C) increase with the silicon content. Hence, silicon-containing boron carbide is less affected by disorder than the undoped one.

experiments show the ability to deposit metastable phases achieving different physical properties by tuning the sputtering parameters.

The sputtered BC films have been characterized by standard x-ray diffraction, Raman, FTIR spectroscopy for molecular and phase analysis and ellipsometry for optical analysis. Specifically, Raman and FTIR spectroscopy will provide information regarding the phonon states in boron carbide, the presence of excess carbon and any disorder in the BC films. Ellipsometry has been used to measure the optical properties of our BC films; since the absorption edge is polytype dependent, varying from 2.3 eV to 3.3 eV, the absorption spectra obtained by ellipsometry will also provide information regarding the presence and abundance of a specific polytype.

Moreover, x-ray photoelectron and Rutherford backscattering spectroscopy have been used for full chemical characterization of the films; scanning electron microscopy (SEM) and atomic force microscopy (AFM) have been used for morphological and topographical study. Finally, transmission electron microscopy (TEM) and electron energy loss spectroscopy (EELS) have been used for detailed structural investigation and evaluation of the fraction of the sp^2 and sp^3 bonding, which is expected to increase with the incorporation of silicon in the boron carbide phase.

4.5 Results and discussion

BC and BC:Si films were deposited using RF magnetron sputtering from hot-pressed B₄C polycrystalline target with Si pieces placed on the preferentially eroded zone in a pure argon atmosphere. The deposition experiments aimed to investigate how the substrate bias and the substrate temperature can affect the stoichiometry and the mechanical

properties of BC films. The RF magnetron systems used for these experiments are schematically represented in Fig. 4.6.

The deposition of BC compounds presents several problems still unresolved, such as the temperature effect on the crystallinity and stoichiometry of BC, the control of the chemical composition and the control of the film thickness during deposition. Another severe problem is the low surface adhesion between boron carbide and different substrates such as glass and silicon.

First we discuss the deposition of BC (Si free) films on silicon and glass substrates at zero bias and at different temperatures (RT, 700 °C, 900 °C, 950 °C and

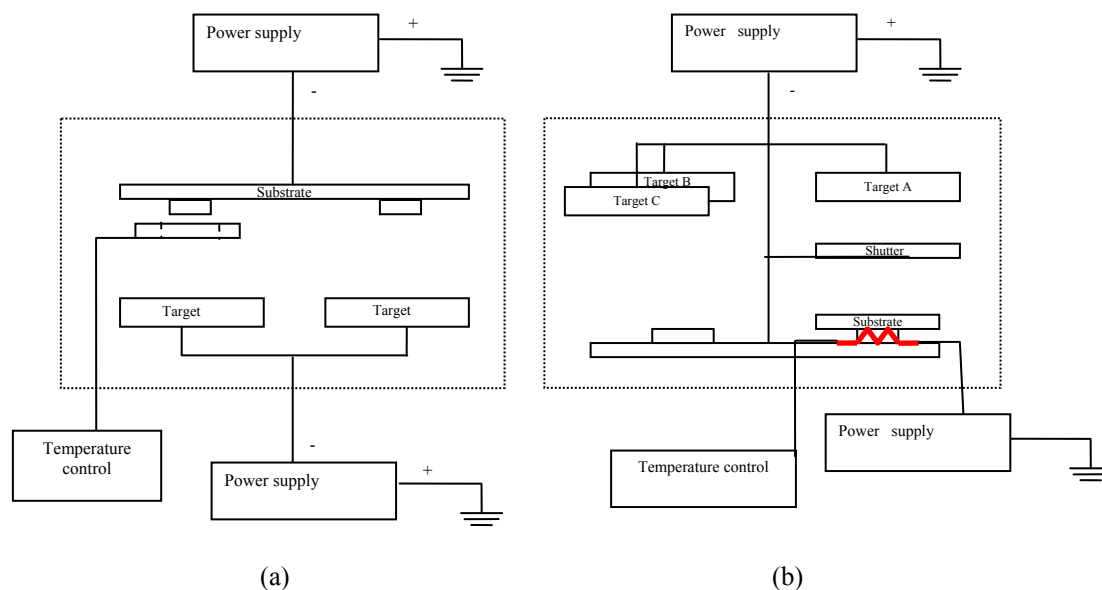


Figure 4.6. (a) Schematic of RF magnetron sputtering system belonging to University of Coimbra. Two RF power supplies are attached to the target and substrate respectively, two target positions are available and the sample holder disk is rotational. The sputtering chamber is connected with a mechanical and turbo pump able to achieve a ultra high vacuum (10^{-4} Torr). A metal resistance can be introduced as heater to sputter at high temperature. (b) Schematic of the RF magnetron sputtering system belonging to Rutgers University. Only one power supply is applied to the target, three targets are available, sample holder and shutter are both rotational. A simple heater was designed to perform high temperature deposition up to 500 °C.

1000 °C). All depositions were conducted using the sputtering apparatus belonging to University of Coimbra (Fig. 4.6a); all experiments were run in a clean room to reduce the risk of contamination and under controlled environment (controlled temperature, humidity, etc.). Sputtering conditions were good with an ultimate vacuum better than 5×10^{-6} Torr and a deposition pressure close to 5×10^{-3} Torr and 450 W power were applied to the BC target. Even though experimental conditions were ideal, a peeling-off of the film build-up was observed. A representative set of BC films sputtered is shown in Fig. 4.7.

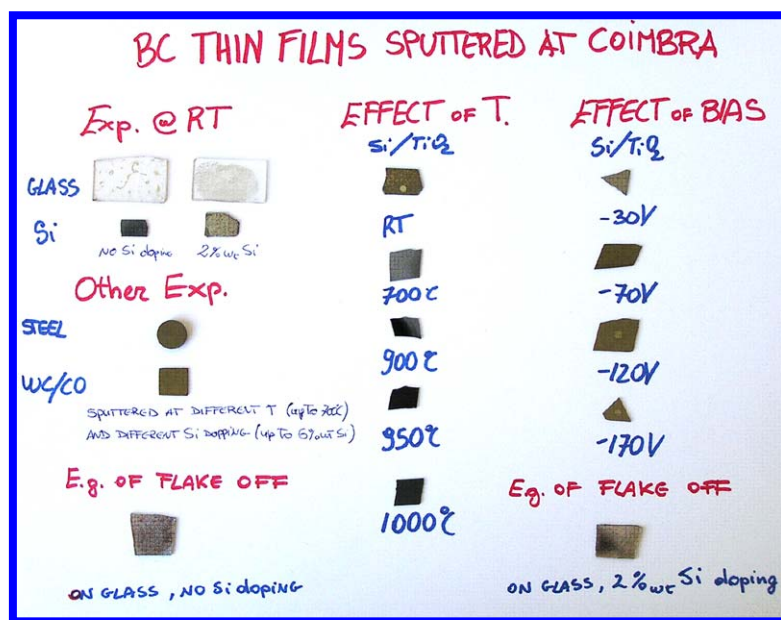


Figure 4.7. Set of sputtering deposition experiments performed at University of Coimbra. BC thin films were obtained by varying substrate bias from -30 to -170 V negative bias. Other experiments were carried out at zero bias but they were annealed at high temperature (up to 1000 °C) after deposition. Many films flaked off because of the weak adhesion between film and substrate.

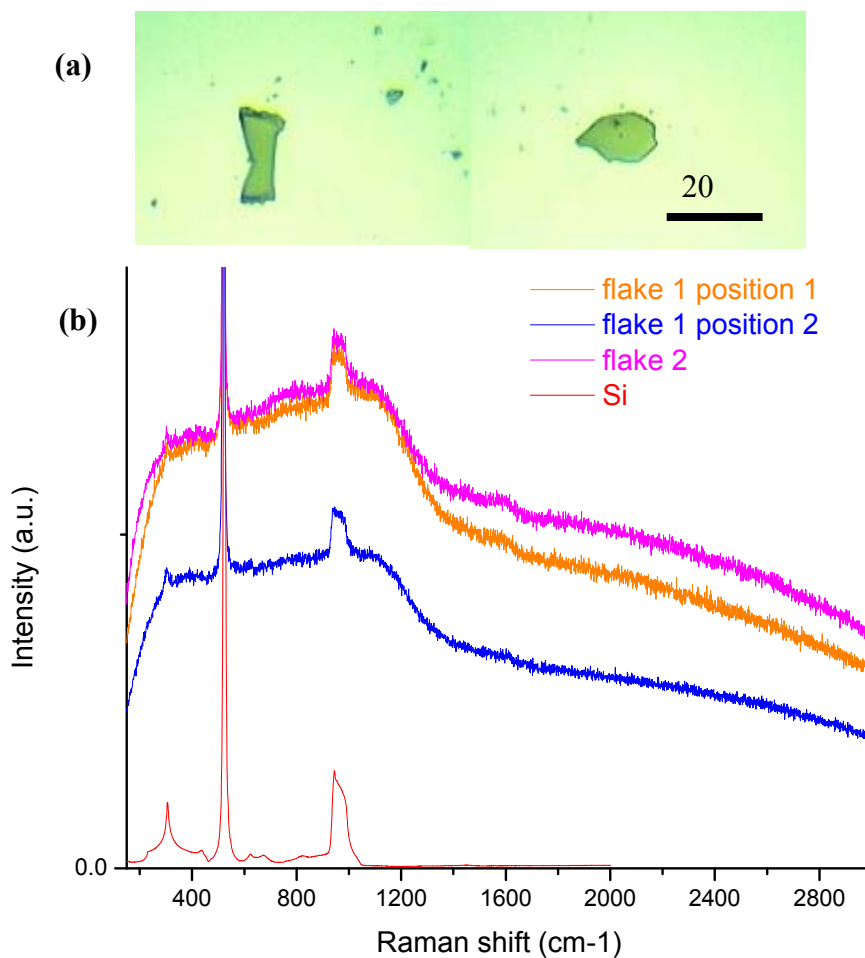


Figure 4.8. (a) Optical microscopy images of flaked BC film deposited at zero bias and 700 °C. (b) Raman spectra showing broad features from 200 to 1200 cm^{-1} , characteristic of *a*-BC. Data are in agreement with recent publications.

The BC flakes obtained at 700 °C were observed under micro Raman revealing their amorphous nature. Raman spectrum (Fig. 4.8) shows broad peaks extending from 200 cm^{-1} to 1200 cm^{-1} ; this is the typical fingerprint of amorphous boron carbide (*a*-BC). Results are in agreement with recent data reported in literature presented in Fig. 4.9 [196, 197]. The narrow peaks at 520 cm^{-1} and around 900 cm^{-1} are not attributable to any boron carbide crystallization, but they are only the first and second order peak of the silicon substrate indicating that the penetration depth of the deposited *a*-BC is larger than the

thickness of the deposited films which are expected to vary from 1.5 to 2 μm after 2 hour deposition.

BC (Si free) films obtained at higher temperature, up to 1000 $^{\circ}\text{C}$, do not show the presence of any crystalline BC phase in the Raman spectra. On the contrary, by increasing the substrate temperature, many large carbon inclusions are observed under micro-Raman technique (Fig. 4.10).

In summary, only *a*-BC was sputtered at all temperatures and the film/substrate adhesion was so weak that the coating films peeled off in *a*-BC flakes while the remaining attached material on the silicon substrate (probably a few atomic layers) contained only graphitic carbon, further promoting film delamination.

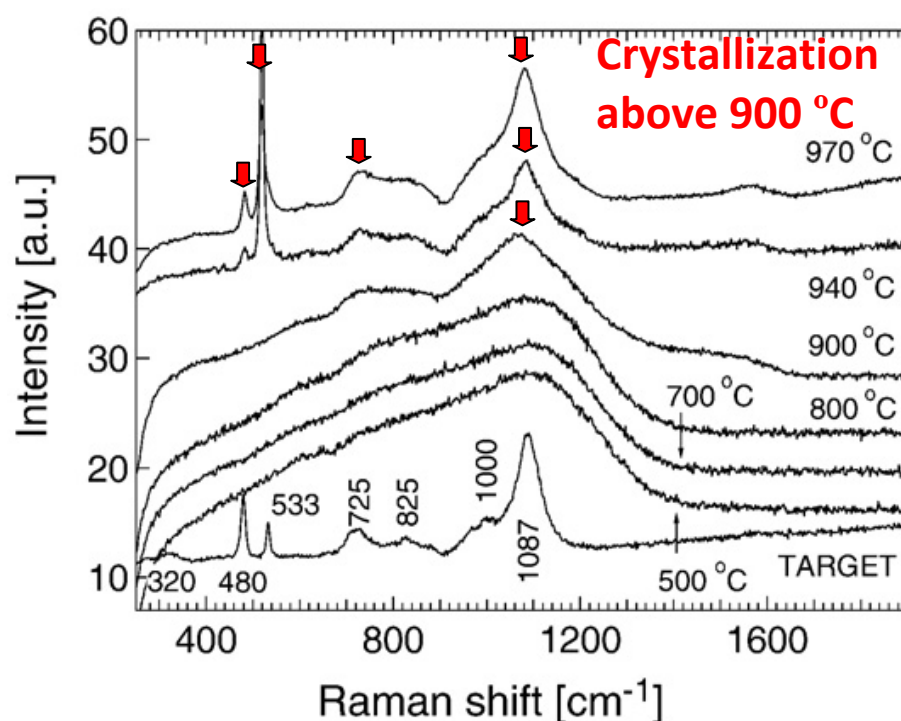


Figure 4.9. Raman spectra for films deposited on grounded substrate at temperatures of 500, 700, 800, 900, 940 and 970 $^{\circ}\text{C}$ and boron carbide target material.

Fourier transform infrared spectroscopy (FTIR) measurements were performed by mixing the *a*-BC flakes with KBr, which is transparent in IR. The results shown in Fig. 4.11 suggest that the increasing substrate temperature used during deposition did not affect the icosahedral arrangements. This observation finds confirmation also in literature [189, 198].

However, the BC flakes obtained at RT showed a transmission band centered at 1600 cm^{-1} , usually assigned to the stretching mode of the three atoms chain [199], which

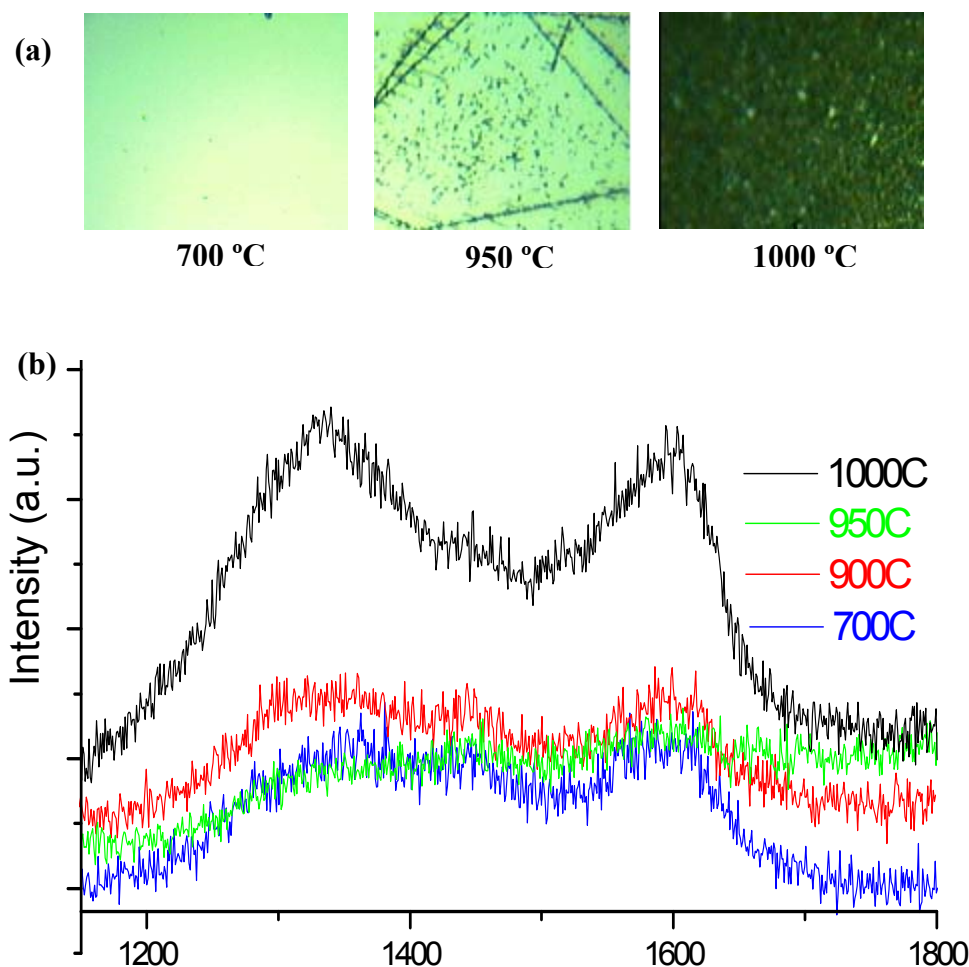


Figure 4.10. (a) Optical images and (b) Raman spectra of films sputtered at different temperatures. Carbon *D* (1330 cm^{-1}) and *G* (1580 cm^{-1}) bands are observed. No crystalline BC was formed. No boron carbide features are observed but only Si peaks belonging to the substrate.

disappear at higher temperatures. We suggest that the band around 1100 cm^{-1} is related to the icosahedra breathing mode and the transmission bands centered at 1440 cm^{-1} are

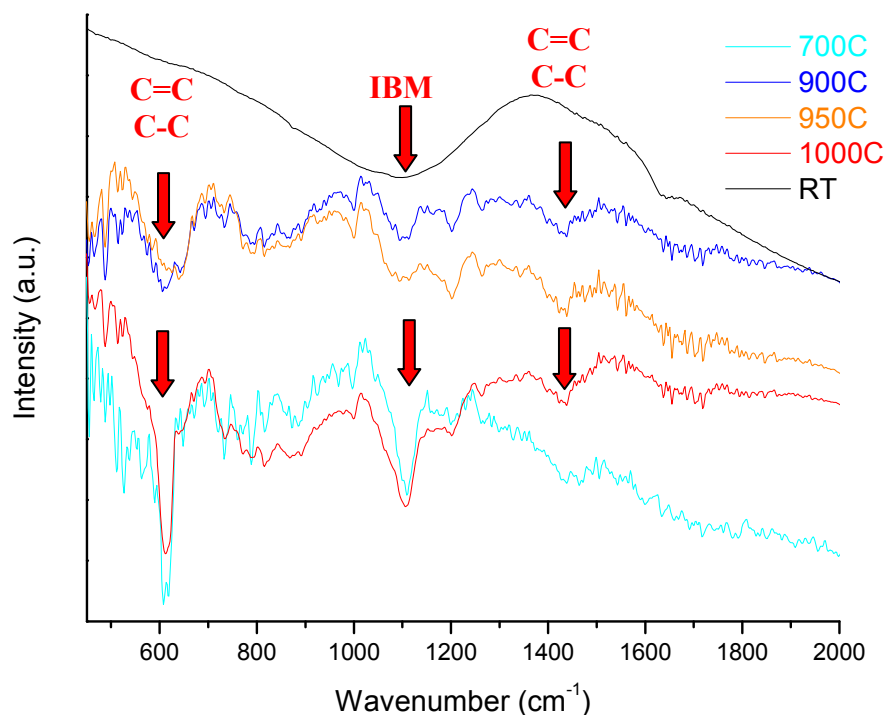


Figure 4.11. Infrared spectra showing the transmission bands for the α -BC flakes. The enhanced bands at $\sim 1100\text{ cm}^{-1}$ are probably related to the icosahedra modes, while the bands at 600 and 1440 cm^{-1} could be associated with the presence of the carbon bonds.

associated with the anti-symmetric deformation mode of the sp^2 and sp^3 carbon bonds respectively C=C and C-C [200]. Finally, the nature of the transmission peak at 620 cm^{-1} , which appears only at higher temperatures, is still not very well understood; we believe it is related to either the CH stretching mode or the presence of graphitic sp^2 -bonded carbon. This hypothesis suggests that the deposited α -BC films are probably formed by intact B_{11}C icosahedra, graphitic and amorphous carbon α -C; in particular α -C is mostly formed during high temperature sputtering depositions. Indeed, α -C is commonly found

to be formed during PVD depositions[200]. The skeleton of α -C network is made out of a mix of single, double and triple carbon bonds and CH. The deconvolution of the transmission band centered at 1440 cm^{-1} helps in indicating the type of carbon present in the films and their abundance. For instance, the transmission band for the asymmetrical vibration of sp^2 carbon in methylene group ($=\text{CH}_2$) rises at 1420 cm^{-1} , the vibration of sp^3 carbon in ($-\text{CH}_2$) rises at 1457 cm^{-1} and the vibration for sp^3 carbon in the methyl group (CH_3) is centered at 1460 cm^{-1} [200]. The ratio of sp^2 and sp^3 carbon influences the properties of thin films such as hardness, conductivity and optical band gap.

In order to improve surface adhesion, a thin layer (300 nm) of titanium Ti was grown before the film depositions. The sputtering conditions were kept constant as in the previous experiment (vacuum better than 5×10^{-6} Torr, working pressure close to 5×10^{-3} Torr), but a negative bias from 0 to -170 V was applied to the substrate.

The presence of the Ti interlayer and the application of a negative bias notably helped the adhesion strength between film and substrate. The Ti has probably favored the

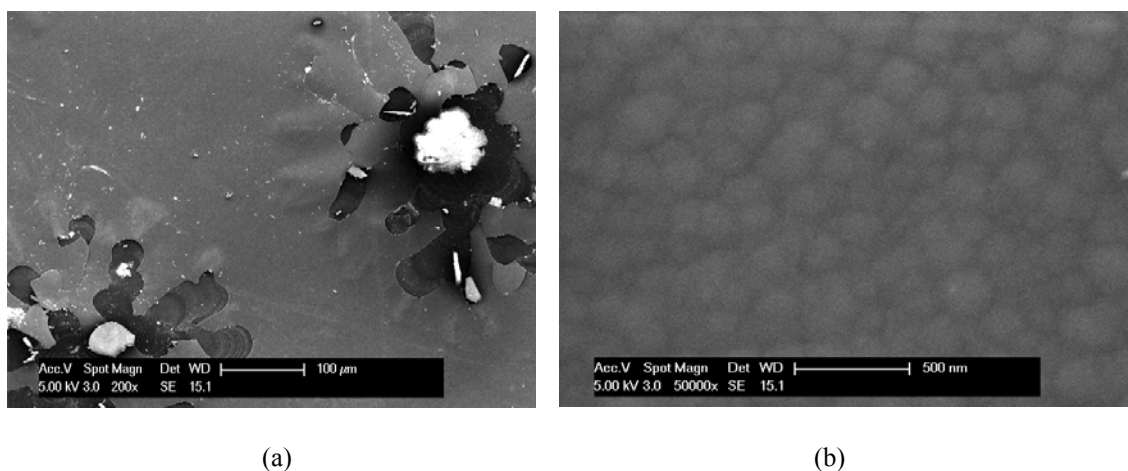


Figure 4.12. SEM images of (a) unbiased sputtered α -BC showing Ti interlayer within the delaminated area; (b) sputtered α -BC film deposited on Ti interlayer applying -170 V substrate bias, the α -BC film has a strong adhesion with the silicon substrate and shows a nanogranular morphology.

formation of chemical bonds between Ti and the B or C incoming atoms during the sputtering process; on the other hand, the application of a negative bias provided a stronger and confined ion bombarding reducing the growth rate of the film and the number of defects. While delamination is shown in the unbiased film, the BC films obtained by applying negative bias seemed to be much more compact and with a good adhesion to the silicon substrate. Scanning electron microscopy images in Fig. 4.12 suggest that the films sputtered at higher bias are very uniform and with a nanogranular structure.

Raman microspectroscopy investigation confirms that the films sputtered on top of the Ti interlayer are α -BC. Only the unbiased film flaked off and the remaining thin layer of material is mostly carbon, similarly to the results of our first set of experiments. The curves in Fig. 4.13 have been shifted in intensity scale for clarity and no structural differences were observed when varying the negative substrate bias.

X-ray diffraction pattern adds new information about the nature of the deposited films. Titanium oxide strong peaks were detected (anatase TiO_2 phase [201]) coming from the adhesion interlayer; the peaks were found shifted by 1-2 degree indicating that the TiO_2 interlayer experienced a residual tensional stress after the deposition of the BC film. Also, many low intensity sharp peaks were distinguished in the background (Fig. 4.14). Several small peaks were identified to be boron (β -B phase), and two peaks were found to be related to graphitic carbon [202]. While graphite was often observed in boron carbides and also BC powders, the presence of crystalline boron may raise several questions on the nature of amorphous boron carbide. Our XRD results reinforce the hypothesis proposed by Fanchini [135] who describes the amorphous boron carbide as an

arrangement of segregated phases involving graphitic layers along the (113) plane and displaced boron B_{12} icosahedra (cf. Fig. 3.3c). In this “sandwich” structure, blocks of boron icosahedra are periodically spaced with multilayers of graphitic carbon, and XRD should be able to detect the interplanar distances.

It is worth noting that XRD results are not necessarily in contradiction with the precedent Raman spectra. Many groups have already reviewed the Raman band of all possible boron phases, including α -boron, β -boron and amorphous boron [177, 203]. All boron phases have different features, but they all fall into the same range from 700 to 1300 cm^{-1} . The invisibility of the boron related phases in α -BC can be justified by the overlapping of the crystalline bands with the amorphous Raman features. Also, it is

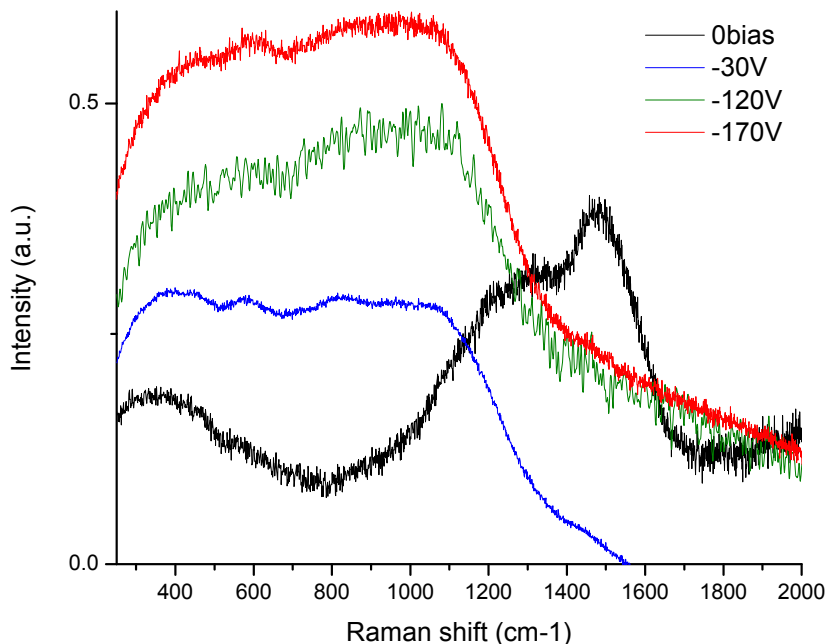


Figure 4.13. Raman spectroscopy on BC films sputtered on Ti interlayer by varying the negative substrate bias from 0 to -170 V. The unbiased film (in black) has flaked off and the remaining layer of material only shows the presence of free carbon.

possible that the Raman cross section of α -BC is much larger than the cross section of crystalline β -B; as a matter of fact, the Raman carbon signal detected from the sputtered films was also unusually weak compared with the broad amorphous bands (Fig. 4.8 and Fig. 4.13).

Once the amorphous nature of BC films has been established, the next goal is to investigate if the substrate bias has large influence on the mechanical properties of the sputtered films. Further we will study the effect of Si addition to the BC.

The application of a negative bias can change the electrical field near the substrate resulting in enhancement of the ion bombardment on the growing film, increase in

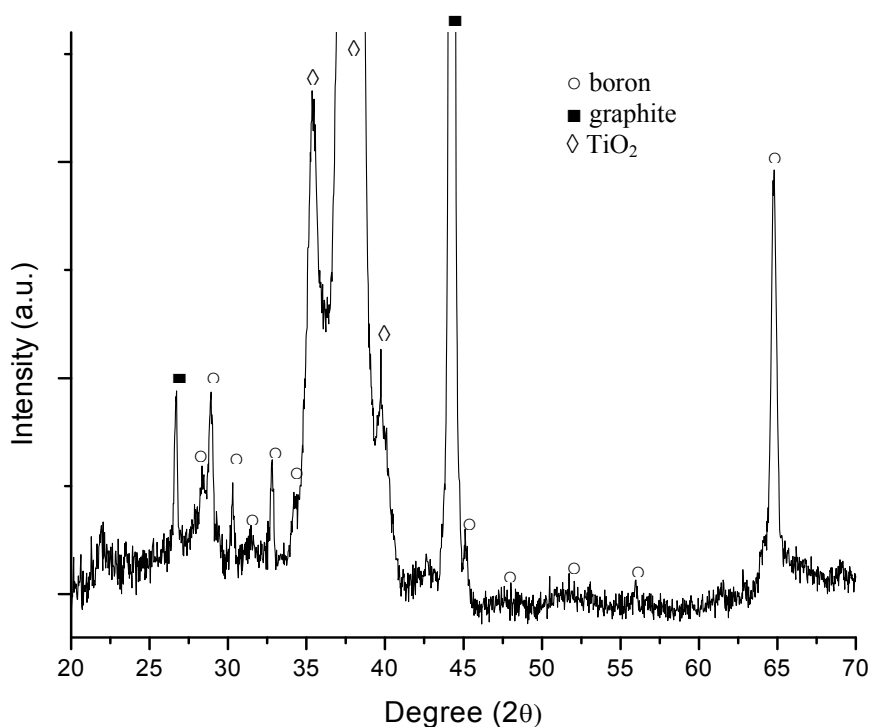


Figure 4.14. XRD pattern of a BC film sputtered on top of Ti interlayer. The film was sputtered at RT, applying a negative bias of -70 V. The TiO_2 peaks are shifted by about 1-2 degrees demonstrating that the interlayer is experiencing residual tensile stress after deposition. The small peaks are related to the presence of boron, probably β -B, and graphitic carbon.

surface mobility of the depositing species and removal of superficial defects. The effect of substrate bias on the BC film stoichiometry, deposition rate and mechanical properties has been studied and the results recently published [199]. Our films showed a drastic change in deposition rate and carbon content as soon as the negative bias was applied, but then on increase of the negative bias from 30 to 170 V had a minor effect in both the film composition and the deposition rate. These results partially agree with other published works where the BC films become boron rich at higher substrate bias leading to off-stoichiometric films with B/C ratio higher than four [204].

The evolution of the films hardness (measured by nanoindentation method using a Berkovich diamond indenter) correlated well with the chemical composition and deposition rate. The hardness for the unbiased *a*-BC film was only 8 GPa, much lower than expected, as a consequence of the presence of free carbon in the C-rich films. As the negative bias was applied, free carbon was re-sputtered and the mechanical hardness increased reaching 25 GPa and remaining constant for higher bias. These results are in contradiction with other results reported in literature [189, 196], where hardness and elastic modulus of the films were shown to decrease with the negative bias. Our results are summarized and compared with other literature data in Fig. 4.15.

The controversial results found in literature make clear that even slight difference in working sputtering deposition conditions, such as system configuration, power supplied to the target, base pressure, Ar working pressure, substrate bias and target-substrate distance can largely affect the stoichiometry and the properties of BC films.

The effect of silicon addition to the amorphous boron carbide was studied by keeping the substrate bias constant (-70 V) and increasing the content of Si from 2 to 6

wt.% through addition of small pieces of Si on the preferentially eroded zones of the BC target (area of the Si pieces varies from 20 to 95 mm²). Hardness measurements showed that a small addition of Si largely improves the mechanical properties bringing the

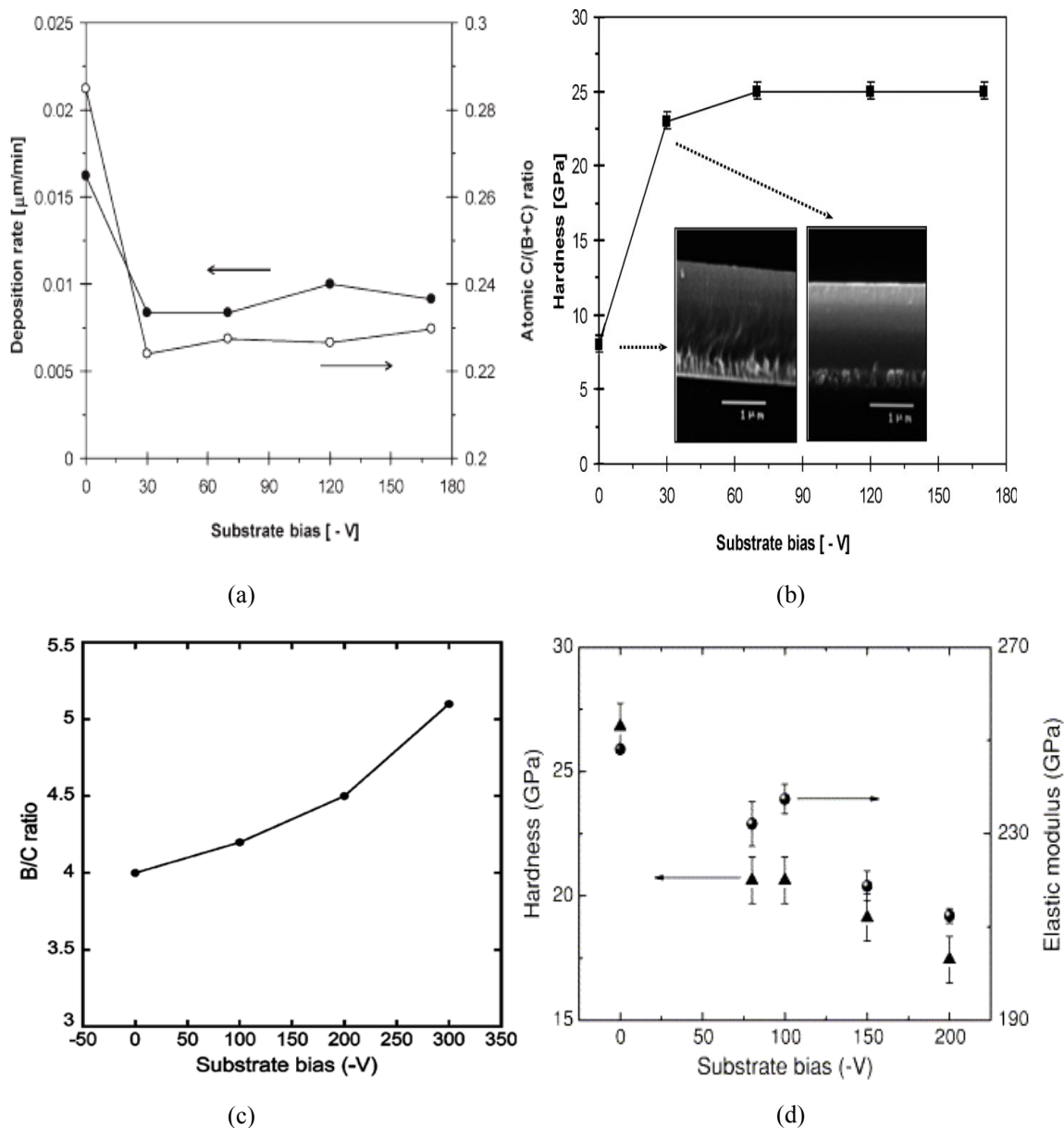


Figure 4.15. (a) Deposition rate and chemical composition of BC films as function of the negative bias. Results can be compared with literature data (Ref. [203]) in (c). (b) Hardness of deposited BC films as function of negative bias (SEM micrograph shown as an inset).

hardness value from 25 GPa of the BC (Si free) film to 30 GPa (Fig. 4.16a). The experimental observation is in agreement with the theoretical calculation of Fanchini who suggested that Si doped B_4C would help eliminating the weaker B12(CCC) polytype responsible for premature failure of boron carbide under loading.

All the samples were finally annealed up to 700 °C in order to study the thermal stability of the BC:Si films in protective environment. The evolution of the hardness shown in Fig. 4.16b indicates a general improvement of the mechanical properties after the thermal treatment. The highest hardness (37 GPa) was found to be achieved at 600 °C for a doping content of 2.5 wt.% Si. This result can be interpreted in terms of local crystallization or rearrangement of the boron icosahedra. Further, Raman investigations will clarify which position the silicon occupy in the α -BC structure and what kind of distortion the Si atoms are responsible for due to their larger size, compared to carbon.

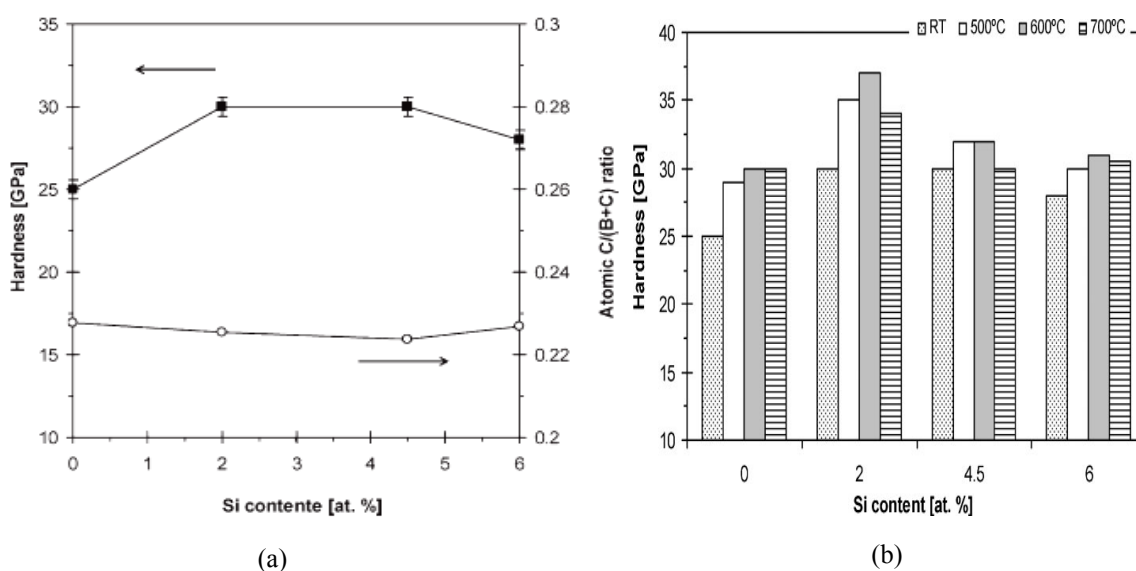


Figure 4.16. (a) Hardness and atomic C/(C+B) ratio of the as deposited BC:Si films as a function of the silicon content. (b) Evolution of the hardness of BC:Si coatings as a function of annealing temperature in protective atmosphere.

We tried to repeat a similar experiment using the RF magnetron sputtering system belonging to Rutgers, the schematic of which is shown in Fig. 4.6b. The main differences between the sputtering system located at Rutgers and the one belonging to the University of Coimbra are (i) its large size which implies a longer distance between the substrate and the target, (ii) lack of the capability to apply substrate bias, (iii) absence of a mobile shutter for pre-sputtering routine and (iv) absence of in situ heater for deposition at high

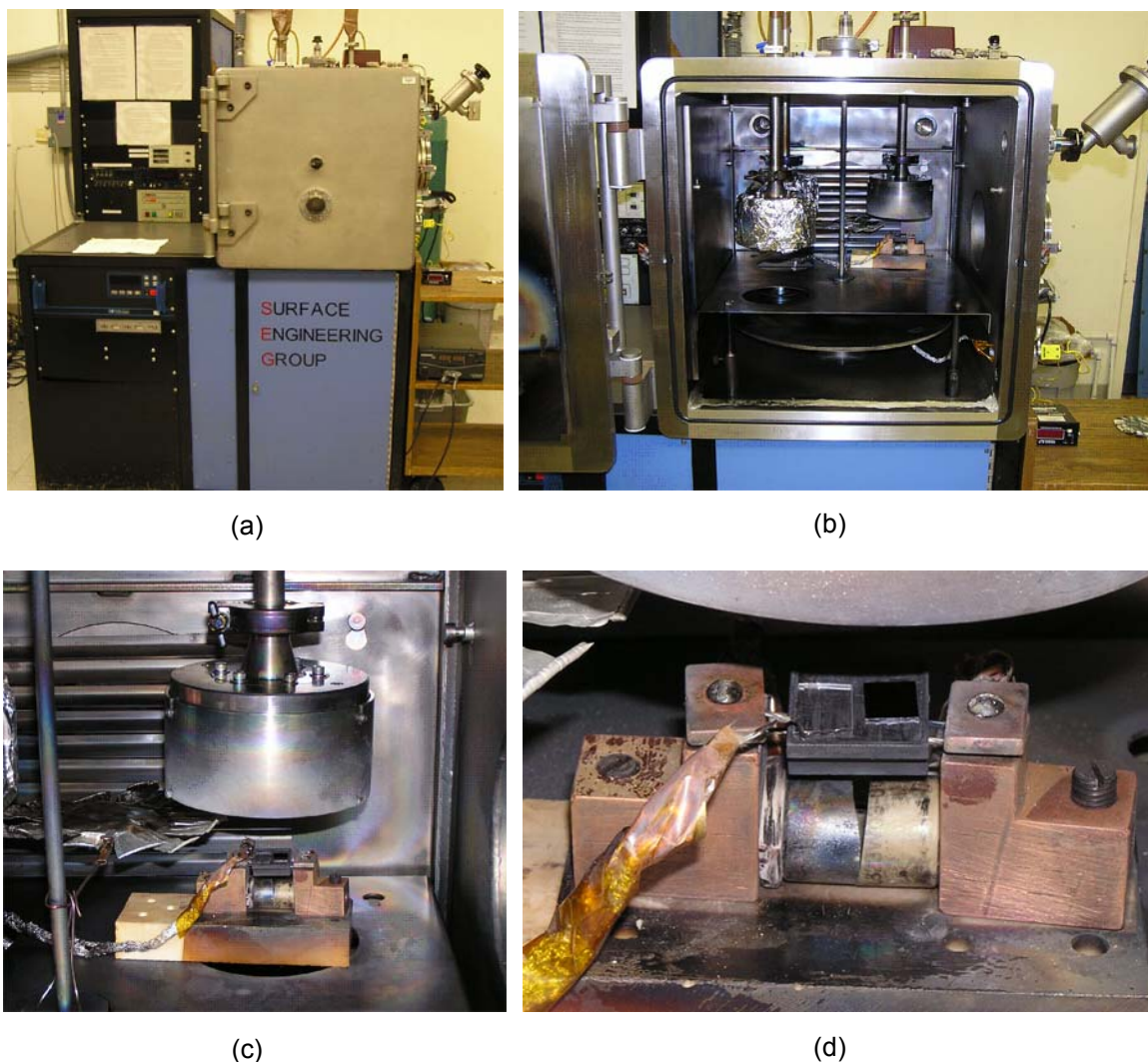


Figure 4.17. RF magnetron sputtering system belonging to Rutgers University: (a) external view, (b) open vacuum chamber, (c) close up view of target-substrate configuration, (d) designed heater.

temperatures. In Fig. 4.17, the Rutgers RF magnetron sputtering system is shown after some technical improvements: a simple rotating shutter was made out of a rigid aluminum foil, the target-substrate distance was drastically lowered by the use of an

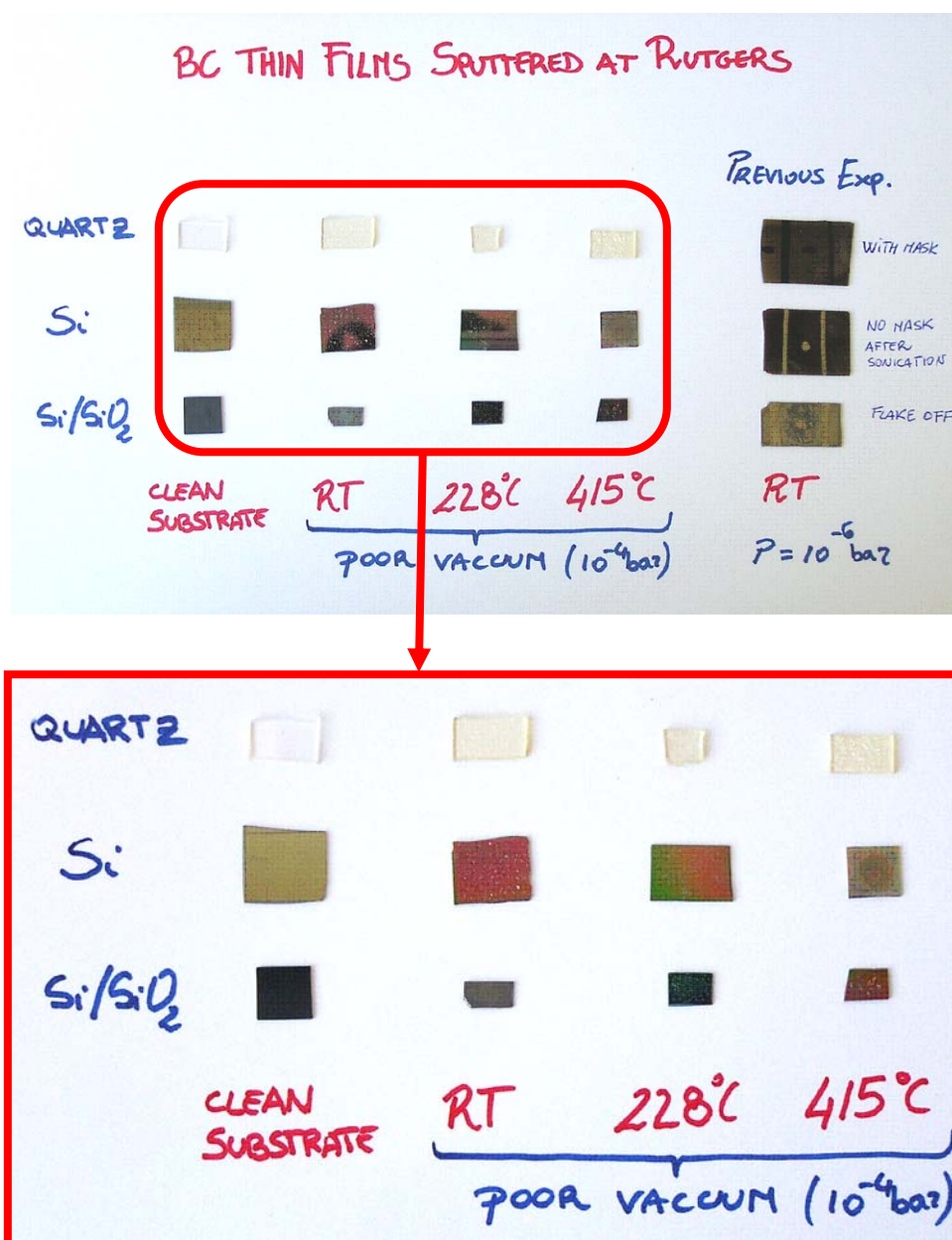


Figure 4.18. Set of sputtering deposition experiments run at Rutgers. BC thin films obtained by varying temperature are in the red box.

adjustable steel stage, a basic heater was built with two tungsten filaments connected in parallel (in order to increase their resistance) and hidden in a graphitic carbon crucible (very conductive and thermally resistant); the built-in heater and the thermocouple were connected through copper wires to a small external DC power supply. Naturally, we tried to minimize the presence of extraneous material in the sputtering chamber to avoid contamination, and we made sure that the system was always grounded after all electrical connections were set up.

As mentioned above, sputtering conditions are very critical for the quality of the coatings and finding the ideal working parameters suitable for a particular sputtering configuration and a particular desired product can take long time.

A representative set of samples sputtered with the implemented RF sputtering system is shown in Fig. 4.18.

The sputtering conditions during this study were initially very good with an ultimate vacuum of 3.75×10^{-7} Torr; the Ar flow rate used was in the range of 30-40 SCCM (standard cubic centimeters per minute) reaching a sputtering chamber pressure in the range of 8 to 14 Pa, and the maximum power applied to the hot pressed BC target was 200W. Silicon, quartz and glass substrates were cleaned by a DI water/methanol solution and sonication was used as the regular procedure. On some of the substrates, a mask was drawn by permanent marker which was removed after deposition by applying gentle sonication. Before all depositions, pre-sputtering was applied for 30 minutes while the BC deposition continued for 2 more hours. BC films deposited at RT flaked off as expected and no Raman signatures were detected except for carbon residuals and other nonsignificant contaminants. The thickness of the BC film was roughly measured by

profilometer on the edge of the removed mask and it was found to be only 50-60 nm, much lower than the expected 1 μm , confirming that the delamination problem occurred.

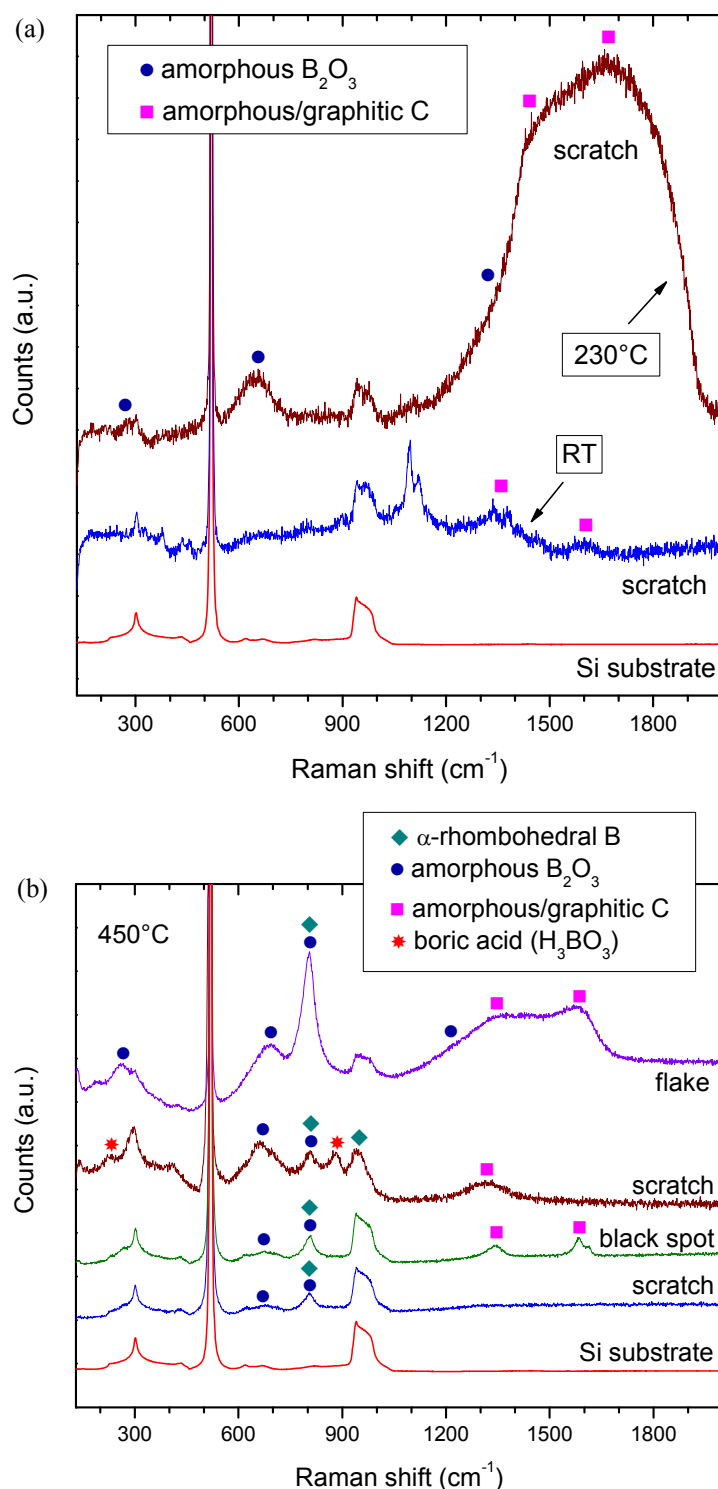


Figure 4.19. Raman spectroscopy on films sputtered at (a) RT and 230 °C and (b) 415 °C. Films were deposited by using the sputtering system implemented in Fig. 4.17. Formation of boric acid and boron oxide has been detected due to poor vacuum conditions during deposition.

The application of higher substrate temperatures negatively affected the chamber pressure, worsening the sputtering conditions. The poor vacuum conditions were lately detected because of the damage to the Penning gauge directly connected to the chamber, which was showing reasonable values. Further investigations showed that micro leaks of air were coming from the walls of the chamber; most probably our sputtering chamber was not designed for baking process and even slightly elevated temperatures lead to leakage. Once the vacuum pressure is broken during sputtering deposition, irreversible and expensive damages can also affect the turbopump, the pressure gauges and the flow rate controllers leading to the shutdown of the entire system.

Raman spectroscopy revealed that various boron phases different from boron carbide were synthesized during deposition at higher temperature (Fig. 4.19). Formation of boric acid H_3BO_3 and boron oxide B_2O_3 were detected in the films sputtered at 415 °C. The glassy boron oxide B_2O_3 is the most stable and common oxidation form of boron and the excess of oxygen due to the poor chamber vacuum conditions favored its formation in the place of boron carbide BC. Influence of oxidation on the composition and structure of boron carbide has been already investigated in term of formation of B_2O_3 layer [205] and strength degradation [206].

The boric acid H_3BO_3 is known to form very easily from the spontaneous reaction of boron and boron oxide with moisture and oxygen in air [207]. However, synthesis of such boron phase, even though important for basic physic understanding, does not currently find interesting applications.

The use of sputtering deposition technique described in this chapter allowed us to fabricate α -BC and Si doped Si:BC thin films with improved mechanical properties, but it

was not possible to synthesize crystalline BC polytypes. A further attempt to obtain crystalline boron carbide nanostructures is presented in the Chapter 5 by the use of another out-of-equilibrium method such as submerged arc-discharge.

CHAPTER 5

SYNTHESIS OF NANOSTRUCTURES USING ARC DISCHARGE

5.1 Theory of the electric arc

There are several discharge phenomena involving different parameters of electric field, current, gas pressures and plasma temperatures. Even though it is difficult to exactly define what is an electric arc, in general plasma physicists agree that the arc must be defined in terms of current and voltage drop only [208]. An electric arc is simply an electrical breakdown between two conductive electrodes, usually carbon based, through a non-conductive media such as air. A continuous discharge can be ignited by applying either a direct or an alternating current and it results in a very high temperature of the arc region where most materials can be melted or vaporized.

An electric arc is characterized by a nonlinear relationship between current and voltage. In particular, it was noticed that arc discharge devices, as well as other vacuum tube devices, exhibit a negative differential resistance effect. In other words, increasing current would result in lower voltage between the arc electrodes, which is exactly the opposite of what is expected for a simple ohmic resistor. A typical voltage versus current characteristic curve for a generic discharge between two electrodes without sharp edges or points is presented in Fig. 5.1 [209]. The I-V curve shows three major domains: the dark discharge, also called Townsend discharge, the glow discharge and the arc discharge [209]. The main difference between an arc and a glow discharge is that the density current during the arc at the cathode is very high while the drop in mechanical tension between the electrodes is very low. The uncontrolled increase in current at the cathode

during the arc with a fixed voltage can lead to destructive experiments ending with the total destruction of the arc discharge apparatus.

The temperature of the plasma components which are generated during the arc (electron, ion and neutral gas) is defined kinetically by the equation:

$$\frac{3}{2}KT = \frac{1}{2}mC^2 \quad (5.1)$$

where K is Boltzmann's constant, m is the mass of the particles and C is their mean square velocity. In the case of high-pressure arc region the plasma will reach a local thermodynamic equilibrium meaning that at each point of the plasma the temperature is different and the temperature gradient through the discharge can be significant.

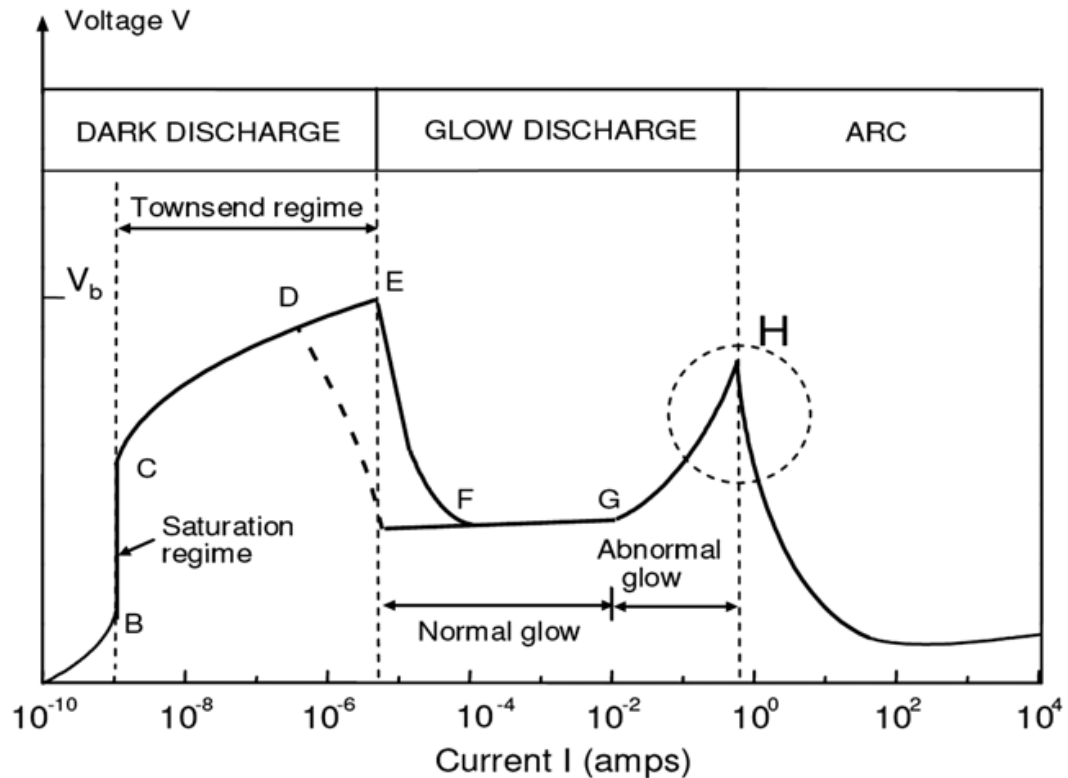


Figure 5.1. Voltage versus current characteristic of low-density plasma discharge regimes without tips or edge. The point H at about 1 Amps indicate the inversion of the slope corresponding to the transition between glow and arc discharge.

The presence of ions makes the space where they exist conductive since they are charged positively or negatively and their movement constitutes a current of electricity; therefore a better understanding of how they are produced during the arc and how they affect the potential gradient between the electrodes is required. Ions usually quickly recombine with other molecules present in the air forming again neutral atoms, but a continuous production of ions is needed during the electric arc. In general, ions can be formed in several ways such as by radio-active substances, X-rays, UV light, impact with other atoms, chemical action especially at high temperature or incandescent solid. In particular, only ionization by impact and by hot solids is involved in the arc discharge.

Ions immersed in an electric field tend to move with an accelerated velocity and eventually hit other atoms or gas molecules. When the temperature is high enough, the typical kinetic energy of ions reaches the energy required to ionize other atoms ($K_B \sim E_{\text{ionize}} = E_{\infty} - E_i$); the degree of ionization (density of the plasma) can be described as function of temperature by Saha's equation [210]:

$$\frac{N_+}{N_0} = A(K_B T)^{3/2} N_e^{-1} \exp\left(\frac{-E_i}{K_B T}\right) \quad (5.2)$$

where N_+ , N_0 and N_e are respectively the number of ions, neutral atoms and electrons per unit volume, E_i is the ionization energy for neutral atoms, K_B is the Boltzmann's constant and A is another constant correlated with the partition function, $A = 2Q_+/Q_0 \cdot (2\pi m_e)^{3/2}/h^3$.

On the other hand, at low pressure (10^{-3} Torr or so) the electrons have a long free path and their temperature exceeds considerably the temperature of the heavy molecules resulting in a more efficient exchange of energy between ions and neutral atoms. Owing to the long free path it is possible to assume that the temperature is uniform across the discharge and, in first approximation, only carrier generations induced by the hot electron

gas need to be considered [208].

The density of positive and negative ions in the space between the two electrodes where ionization occurs strongly affects the fall of potential through the arc. In the areas with only ions of one sign, the potential gradient changes rapidly causing a large voltage drop in the immediate neighborhood of the electrodes, while in the central region (historically called positive column region), it is possible to assume a gradual linear fall in potential (Fig. 5.2) [211]. A simple mathematical description for the voltage drop between the two electrodes is given by:

$$\frac{\partial^2 V}{\partial x^2} + \frac{\partial^2 V}{\partial y^2} + \frac{\partial^2 V}{\partial z^2} = -4\pi\rho \quad (5.3)$$

where ρ is the ions density. If the drop in voltage in the close vicinity of the negative cathode is sufficiently high, the positive ions will attain high velocities and will efficiently hit the surface of the cathode producing also ionization by impact. A similar ionization process can take place at the surface of the anode if the drop in potential is large enough to cause the negative ions to create new ions at the boundary. However, typically the voltage drop at the anode is always lower than that at the cathode.

5.2 The arc discharge technique

Arc discharge is a simple method introduced by Ishigami in 2000 for the continuous production of high purity multi-walled carbon nanotubes [212]. Submerged arc discharge method only requires a direct current (DC) power supply, graphitic carbon electrodes and liquid nitrogen or simply de-ionized water. This is a cheap and high yield non-vacuum method which has been widely used to produce several different carbon nanoparticles [213], carbon nanostructures such as spherical onions [214, 215], nanohorns [216, 217]

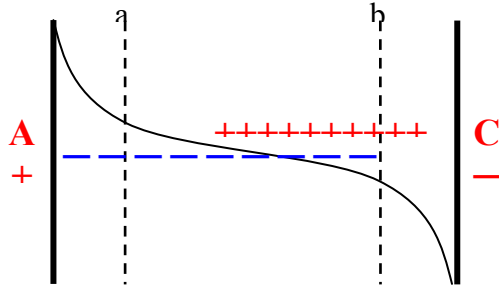


Figure 5.2. Linear fall in potential through the arc when ionization is produced in the gas between the two electrodes.

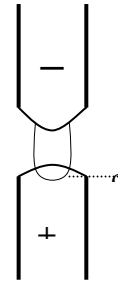


Figure 5.3. Illustration of arc discharge between two carbon electrodes. The positive anode presents a concave bright part called crater (c); the negative cathode is usually pointed and is left in darkness.

and long ribbon-like structures [218].

The arc between the two electrodes requires a low drop in potential at the cathode (as low as 5 volts) and a hot cathode in order to facilitate the emission of ions (thermionic emission) from within the solid to the surrounding gas. According to a simplified model the anodic surface is not involved in any important phenomena other than collecting the electrons produced by the cathode. The illustration in Fig. 5.3 represents a schematic of an arc discharge system between two solid carbon terminals. The positive carbon electrode (anode) has a concave part called crater while the negative carbon electrode (cathode) is often pointed. During the arc the greater part of the light comes from the crater and the cathode is left in relative darkness. Only a small area of the cathod surface originates light and it is called cathodic spot. The gas between the electrodes is also very bright and in the case of flaming arc it can be even brighter than the anodic surface. Lightning is a copious source of electrons which are liberates by the hit electrodes (photoelectric effect).

The resistance of the arc is always negative (see the characteristic curve I-V in Fig. 5.1) and strongly dependent on the vapor of the arc and the shape of the electrodes. Naturally, these conditions change every time the current through the produced arc varies.

The resistance of the arc may, then, be defined as the ratio between a small change in potential difference and the corresponding change in the current which can be expressed as the partial derivative of the potential difference with respect to the current $\partial E / \partial I$. When the electric arc is inserted as part of an electric circuit (made for instance of power supplies, passive elements, motors, etc.), the latter must meet specific requirements in order to initiate and maintain the arc [208].

The first arc ignition only occurs when a cathodic spot exists and a sufficient high voltage is provided by the power supply such that the gap becomes bridged with the arc. However, these conditions are rarely spontaneous phenomena. A spontaneous arc ignition is possible from the Paschen breakdown (similar to the Townsend breakdown in gases) when a cascade of secondary electrons is generated by the ions collisions. The potential difference V required for the arc Paschen's law can be expressed as a general function of the density of gas molecules N and then it is strongly dependent on gas pressure and temperature: $V = f(N, d)$, where d is the gap distance between the electrodes.

Most often the arc is started by motion of electrodes which are brought in contact to be later pulled apart. Electrical breakdown occurs by field emission slightly before the two electrodes touch each other. The presence of extremely high fields (of the order of 10^8 V/m) promotes the ignition of the arc and generation of local hot spots. The exact mechanism involved in the cathodic spot generation is still unknown; however it is clear

that any heating phenomena taking place during the transition phase between the glow and the arc (point H shown in Fig. 5.1) are responsible for the formation of hot spots on the cathodic surface. Among the causes of cathode heating the most likely to promote the cathodic spot and, consequently, the arc is the positive ion bombardment [208].

The maintenance of the arc and the cathodic spot is not easy due to the negative (falling) current characteristic. An arc characterized by a totally falling I-V curve will never reach a stable equilibrium because any accidental change in current would change the voltage drop enhancing the unbalance and vice versa. Stabilization of the electrical arc can be achieved by addition of a ballast resistor between the voltage source and the arc. In Figure 5.4a [209], a conventional circuit is presented, where a DC power supply delivers a constant voltage V_c and a ballast resistor R_b is connected in series. Intersection points of the load line $V = V_c - R_b I$ with the steady characteristic of the arc discharge are indicated in Fig. 5.4 as C and C' and represent the two possible stable operating points at low pressure. From a practical point of view this means that the electrical power delivered by the generator is dissipated by the resistor R_b rather than sustaining the arc

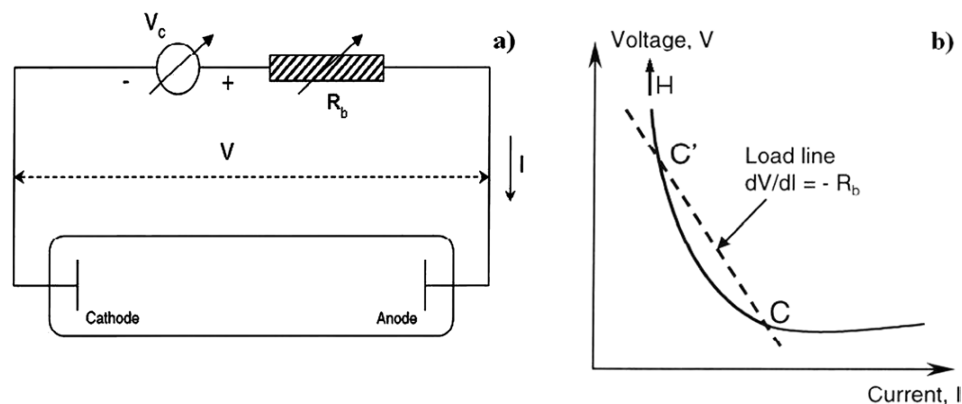


Figure 5.4. (a) Conventional circuit for dc electrical discharges in tubes. (b) Stabilization of the electric arc due to the ballast resistor R_b (C is the stable operating point).

plasma with high electron density limiting the indefinite growth of the current through the plasma. Stable arcs are instead very difficult to maintain in high pressure conditions unless some particular precaution are taken such as fast airflow to refresh the plasma [209].

Finally, it is well known that arc discharges may exhibit hysteresis. These phenomena find explanation in the temperature dependence of the plasma conductivity (cf. Eq. 5.2). When the time derivative of the current is positive, the temperature tends to lag behind with respect to the steady state value at the same current, and this results in a lower conductivity and a higher voltage [208].

5.3 Arc between graphite electrodes

It has been found that the characteristic curve I-V for an arc between solid carbon electrodes depends on the length of the arc and on the shape of the terminals. In particular, the potential difference between the electrodes can be described by the following empirical equation given by Ayrton [211]:

$$V = 38.88 + 2.07I + \frac{11.66 + 10.54I}{I} \quad (5.4)$$

where V is the potential expressed in Volts, I is the current in Amps and l is the length of the arc in millimeters. As shown in Fig. 5.1, the drop potential in the arc discharge area is inversely proportional to the current while the voltage linearly increases with the increasing of the arc length. However Ayrton's equation can predict the drop in potential only for short arcs (up to 6 mm) between flat terminals; conversely, cored carbon electrodes cannot be expressed by a simple equation. Similarly, there are equations to describe the rapid potential drop at a solid carbon anode V_a and cathode V_c [211]:

$$V_a = 31.28 + \frac{9 + 3.1I}{I} \quad \text{and} \quad V_c = 7.6 + \frac{13.6}{I} \quad (5.5)$$

where the drop at the anode is greater than that at the cathode.

As mentioned above, vapor temperature greatly affects the nature of the arc; however, there is no exact method to determine it. In the case of graphitic carbon electrodes, equations concerning the thermal radiation from black bodies can be used to approximately determine the arc temperature from the color of the emitted light. The theoretical Boltzmann's law allows calculating the black body's thermodynamic temperature T from the radiant flux J (total radiation energy per surface area) emitted from the black body: $J(\lambda, T) = cT^4$, where c is a constant function of the wavelength λ of the emitted light. Boltzmann's law derives from an approximation of the well-known Wein's and Planck's laws:

$$J = \frac{c_1}{e^{\frac{c_2}{\lambda T}} \lambda^5} \quad \text{Wein's law (valid for } hc/\lambda \gg k_B T) \quad (5.6)$$

$$J = \frac{c_1}{e^{\frac{c_2}{\lambda T}} \lambda^5 - 1} \quad \text{Planck's law (valid for small } \lambda, \text{ high frequency),} \quad (5.7)$$

with J representing the amount of energy, and c_1 and c_2 constants.

When the light reaches the thermal equilibrium, the temperature of the graphitic carbon electrode (black body) and the surrounding gas is the same. Varying the experimental method (photometric, calorimetric etc.) and theoretical formula used, the arc temperature was found to range between 3900 and 4000 K. Further studies showed that arc temperature also varies with applied current and gas pressure [208].

Another parameter strongly dependent on the current is the size of the anode crater. Empirical formulas suggest that the size of the crater r at the positive carbon anode

is linearly increasing with the current I : $r = a + bI$, where a and b are constants. However, different results were found when cored carbons were used and different arc lengths were considered [208]. The consumption of the carbon electrodes during an arc discharge in air is principally due to the oxidation with a rate of about 1 inch per hour but it can be reduced by controlling the amount of air.

5.4 Arc between substances other than carbon

For many years it was generally believed that carbon was the best material to use as electrode since it can be raised at the highest temperature without being melted. The fact is that many other types of terminals can be used to ameliorate the arc performance and efficiency. For instance, the flaming arc, arcs between oxides or between metals require a lower voltage for the same current and length than the carbon arc, and they all give more light for the same amount of energy.

Electrodes used for the flaming arc are made of cored hard carbons filled with a fine mixture of carbon and salts, especially nitrates and chlorides that produce high luminosity. In the flaming arcs the greater part of the light usually comes from the vapor and lasts much longer than carbon arc. The outer cylinder of carbon protects the salt from rapid consumption and gives the necessary conductivity to the electrode. However, the resistance of such cored carbons is higher than that of solid carbons. Also, the drop in potential at the anode is lowered by the presence of the salts and the flaming arc can be initiated at very low voltage [211]. Depending on the salts used, the flaming vapors can emit different intensity of light with different colors (e.g., white, yellow flaming arcs).

Arcs between metals were found not to be particularly advantageous because they

give much less light and terminals are consumed more quickly than carbons. Even though metal electrodes facilitate the arc ignition the conductivity of the vapor between the terminals fell rapidly after the removal of the impressed voltage. Another complication is that the relationship between potential difference and experimental conditions (current, arc length, electrodes cooling, size and configuration of terminals, etc.) are very complicated. It is not possible, then, to describe the arc between metals with a simple function like Eq. 5.4 commonly used for the carbon arc. Experimental work with iron electrodes [211] has shown that there are two different forms of metallic arcs: the quiet arc occurring in absence of sounds and light, and the hissing arc during which a sudden increase in current and decrease in potential difference makes the vapor near the anode very luminous and the arc noisy. Measurements have shown, however, that the anode drop is always much smaller than in carbon while the cathode drop is similar; in conclusion, metal arc requires less voltage.

Arcs between oxides have been studied as well [211]. Generally, oxides are non-conductors at ordinary temperatures and an auxiliary arc can be used to heat the electrodes and make them conductors. An interesting finding is that the oxides with lower melting point usually require smaller applied voltage and that for very short arc length the voltage is independent of the current. For higher arc distance, instead, the universal characteristic I-V curve is still valid and the general Ayrton equation (Eq. 5.4) for carbons can still describe the potential drop. One of the most important arcs between oxides is the magnetite arc where the cathode is magnetite (Fe_3O_4) and the anode is copper. In particular Fe_3O_4 gives off a very luminous vapor while the copper rapidly dissipates the heat keeping the anode cold and increasing the efficiency. Similar

characteristics can be found for an arc between carbides and copper.

When an arc is initiated between non-similar electrodes, the nature of the two substances needs to be considered. For instance, the current will flow more easily in one direction depending on the conductivity of the electrodes vapor, the tendency to oxidize, the temperature of the terminals, etc. Moreover, it is indispensable to keep always hot the cathodic spot, meaning that a metal cathode with high thermal dissipation and materials easy to vaporize are not ideal for a high efficiency arc.

5.5 Experimental goals and outline

Boron carbide nanostructures possess unusually high thermal conductivity values [219]. Fabrication of such BC nanostructures could open new route to novel applications.

Arc discharge technique enables high yield synthesis of nanomaterials in non-equilibrium conditions. Submerged arc does not require expensive vacuum systems and the products usually contain a minimum amount of contaminants. Moreover, the submerged arc is an ideal environment for rapid quenching of hot vapor emitted by the discharge, making it conducive for the formation of nanomaterials. This technique has mostly been used for fabrication of carbon nanostructures, but it has been shown that it can also produce nanostructures from materials other than carbon [220]. The type of nanoparticles generated by arc discharge can ideally be controlled by controlling the quenching conditions and varying the pressure of the liquid [221].

Our goal here is to find and optimize the experimental parameters s in terms of electrodes, current and arc media. As explained in Chapter 4, we aim at the production of BC polytypes and Si:BC metastable phases.

All arc discharge experiments were conducted at atmospheric pressure in a stainless steel container where two electrodes were submerged in about 2000 cm³ of liquid nitrogen, de-ionized water, or inert gas. The schematic and a photo of the actual experimental setup are shown in Fig. 5.5. The anode was attached at a manual drive system allowing control of the distance between the electrodes. The cathode-anode gap was kept at around 1 mm to maintain a stable discharge and the arc was ignited by mechanical touching of electrodes followed by their immediate separation. Continuous DC current was applied to the electrodes ranging from 10 Amps to 50 Amps by a welder

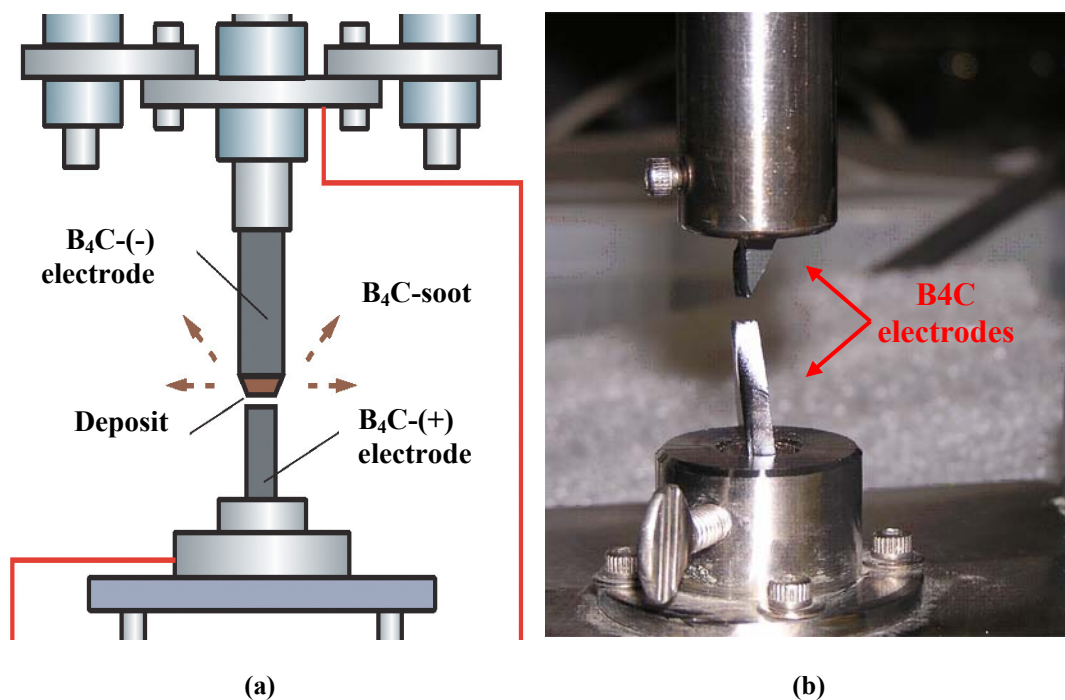


Figure 5.5. Instrumental set up for the submerged arc discharge experiment: (a) schematic, (b) a photo of an actual setup. The boron carbide electrodes are obtained from hot pressed BC pieces, the ends of the electrodes are sharpened in order to promote the formation of the arc between them. The electrodes are submerged in liquid nitrogen/de-ionized water or inert gas and DC current is applied to them while the distance between the BC sharp points is slowly lowered until the anode touches the cathode to initiate an electric arc.

power supply (Miller Thunderbolt XL), while the voltage was kept constant at 25 V. Products were finally collected and analyzed by Raman spectroscopy, X-ray diffraction, scanning electron microscopy (SEM), transmission electron microscopy (TEM) and electron energy loss spectroscopy (EELS).

5.6 Results and discussion

A first set of experiments was carried out by using a hollow graphitic carbon anode filled with commercial B_4C micro powder and a solid graphitic carbon cathode. The electrodes were submerged in liquid nitrogen to allow a fast quenching and hopefully formation of out-of-equilibrium BC nanostructures. The arc was initiated by applying a DC current (50 Amps) and the arcing time was 5-6 s. The products (soot) were collected at the bottom and on the walls of the steel recipient by adding de-ionized water. Then, the soot was dispersed in water and the solution was left in a small beaker waiting for sedimentation. Simply using the gravitational force, it was possible to separate two different phases, one settling at the bottom of the dispersion and the other one remaining floating on the water

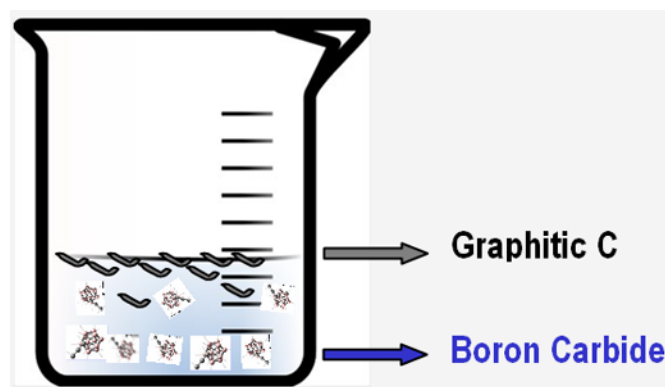


Figure 5.6. A method based on specific gravity of the different nanostructures has been developed to self-separate the various types of nanostructures.

surface. This simple easy phase separation method is illustrated in Fig. 5.6. Products in suspension were collected using a pipette and deposited either on silicon substrates or on the TEM holey carbon grids for further analysis.

First, Raman analysis was performed to identify the chemical composition and the molecular structure of the arc discharge products. Several samples have been selected from the boron carbide aqueous dispersion at different height (from the upper part and from the bottom of the solution) and then deposited on silicon wafers. In Fig. 5.7, characteristic BC Raman peaks at low frequencies around $\sim 300\text{ cm}^{-1}$ and 500 cm^{-1} and at high frequencies from 600 cm^{-1} to 1200 cm^{-1} confirm the successful synthesis of BC with

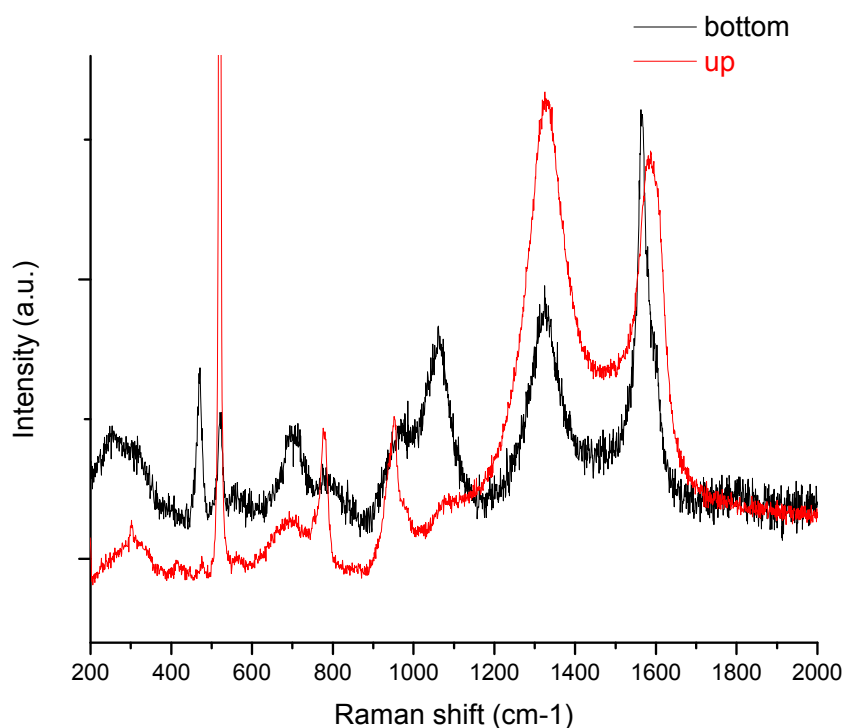


Figure 5.7. Raman spectra of boron carbide soot obtained by submerged arc discharge between two graphitic electrodes. For the bottom part of the solution (black line), BC peaks already discussed in Chapter 4 are present. For the upper part of the solution (red line), larger amounts of carbon (*D* and *G* peaks) are detected. Peaks at $\sim 520\text{ cm}^{-1}$ and 900 cm^{-1} come from Si substrate.

no contaminants. However, it is evident that the amount of carbon greatly increases for the powder floating in the upper part of the boron carbide aqueous dispersion. This result can be expected since graphitic carbon flakes have higher surface area than more compact BC particles and as such tend to float on the surface of aqueous dispersion.

XRD measurements were also collected for the same set of samples; in addition, a small amount of soot was found and collected from the outside walls of the reactor. Spectra are reported in Fig. 5.8 and show boron carbide and graphitic carbon peaks present in the sample collected from the bottom part of the solution, whereas carbon peaks are much more prominent in the upper part of the dispersion and for the soot collected outside of the recipient, in agreement with Raman analysis [222].

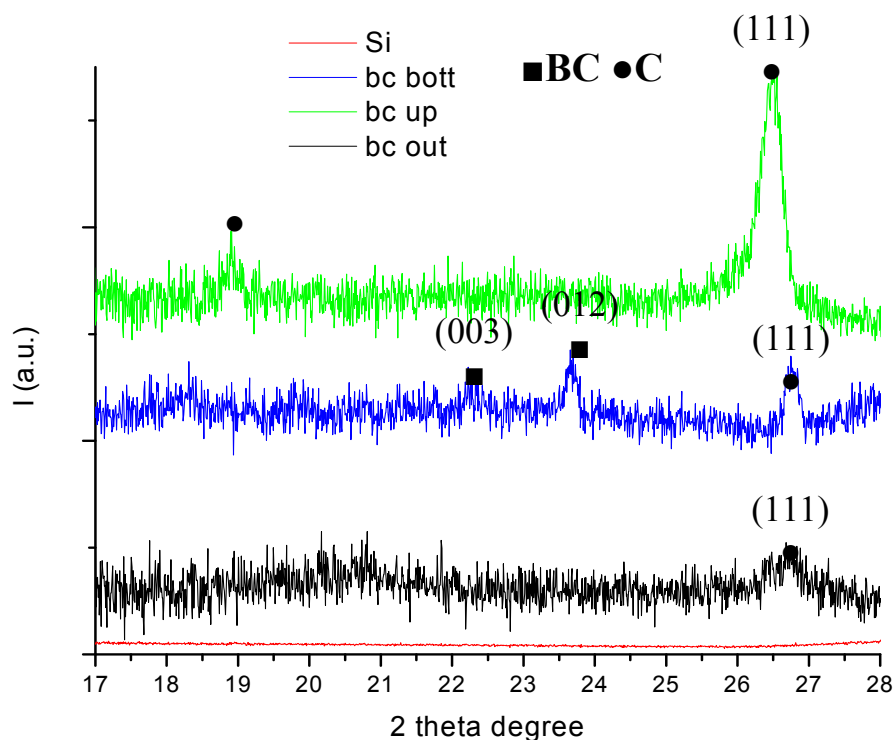


Figure 5.8. XRD spectra of boron carbide soot obtained by submerged arc discharge between two graphitic electrodes. BC (squares) and C peaks (circles) indicate the presence of crystalline BC deposited on the bottom of the recipient and mostly graphitic carbon in the upper part of the beaker.

SEM images of the collected soot produced in liquid nitrogen are shown in Fig. 5.9. A variety of nanostructures were found to coexist in the soot: spherical nanograins, isolated and entangled nanotubes, flat nanoribbons, and rigid nanorod structures.

Closer examination of these nanostructures by TEM revealed clearly their crystalline nature. TEM samples were prepared by depositing a few drops of boron carbide aqueous dispersion on the holey carbon grid with subsequent drying in air. In Fig. 5.10a and Fig. 5.10b, features of nanotubes are shown respectively at low and high magnification. In the high magnification image of Fig. 5.10b, it is possible to distinguish multi-walled nanotube structures, while in Fig. 5.10c, a close-up view on the spherical granular structure already seen under SEM is shown. In order to understand the chemical composition of the observed nanostructures, EELS measurements were performed on the

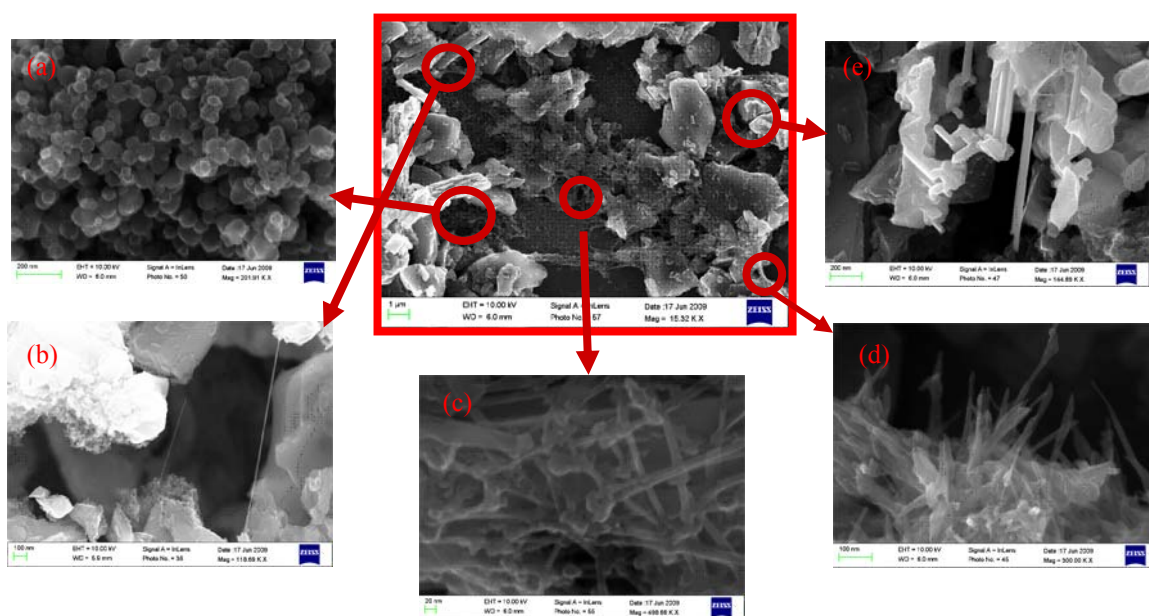
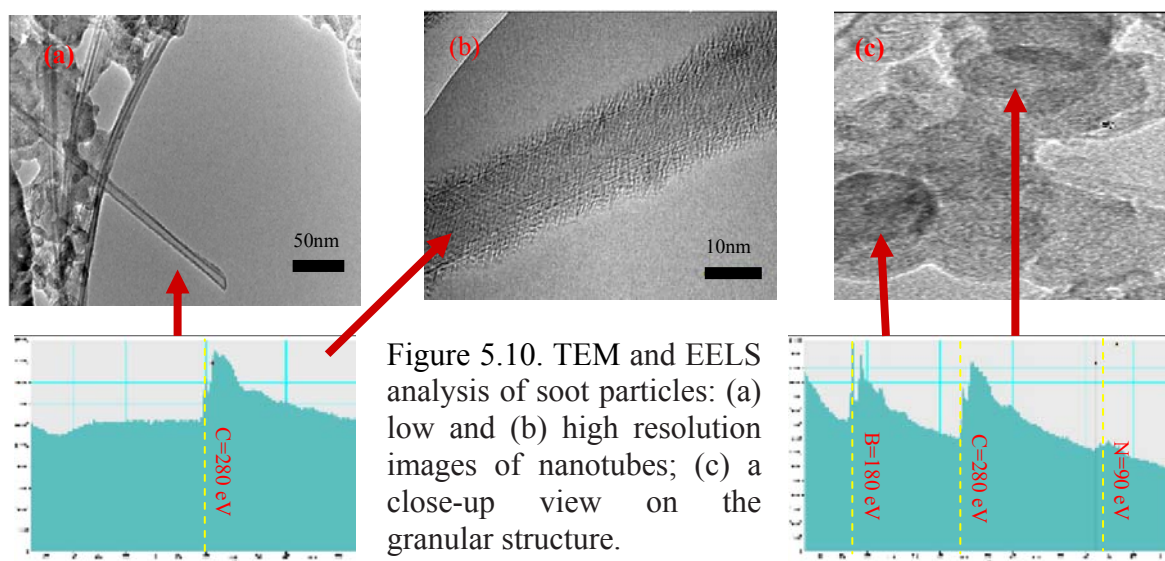


Figure 5.9. SEM images of collected soot performed obtained at an accelerating voltage of 10 kV and a working distance of 6 mm. Different nanostructures were formed during the arc discharge in liquid nitrogen: (a) nanograins, (b,c) nanotubes, (d) nanoribbons, and (e) rigid nanorods. The image in the center shows a low magnification image.



local area shown in Fig. 5.10a-c. EELS spectra indicate that such nanostructures are mostly carbon based; also trace of nitrogen trapped in gaseous form was found.

It is reasonable to conclude that during the arc discharge between graphitic terminals only carbon nanostructures have been formed during the fast quenching in liquid nitrogen because they are much more stable than any other boron carbide structures.

New set of experiments using pure hot pressed stoichiometric B_4C electrodes was set up (Fig. 5.5). This time the arc was initiated applying lower current (10-20 Amps) and different media were explored to submerge the terminals and quench the products. In particular, arc discharge experiments were performed in liquid nitrogen, de-ionized (DI) water, and inert gas such as argon (Ar). As before, the soot accumulated on the bottom of the reactor, on the walls and in proximity of the electrodes was washed out with DI water and collected by pipette. Finally, the dispersion was deposited on the silicon substrate and dried in air.

When B_4C solid electrodes were submerged in DI water, the product collected

from the bottom and the walls of the recipient was made of different phases. Raman spectra in Fig. 5.11 show the formation of boron carbide structures and carbon nanotubes (splitting of the *G* band and the presence of RBM modes). Under optical microscope, carbon nanotubes appear as small black spots while the boron carbide has a dark-grey color (inset in Fig. 5.11). Formation of unwanted carbon nanotubes could be expected due to their high stability in water, the reactive environment and the slow quenching.

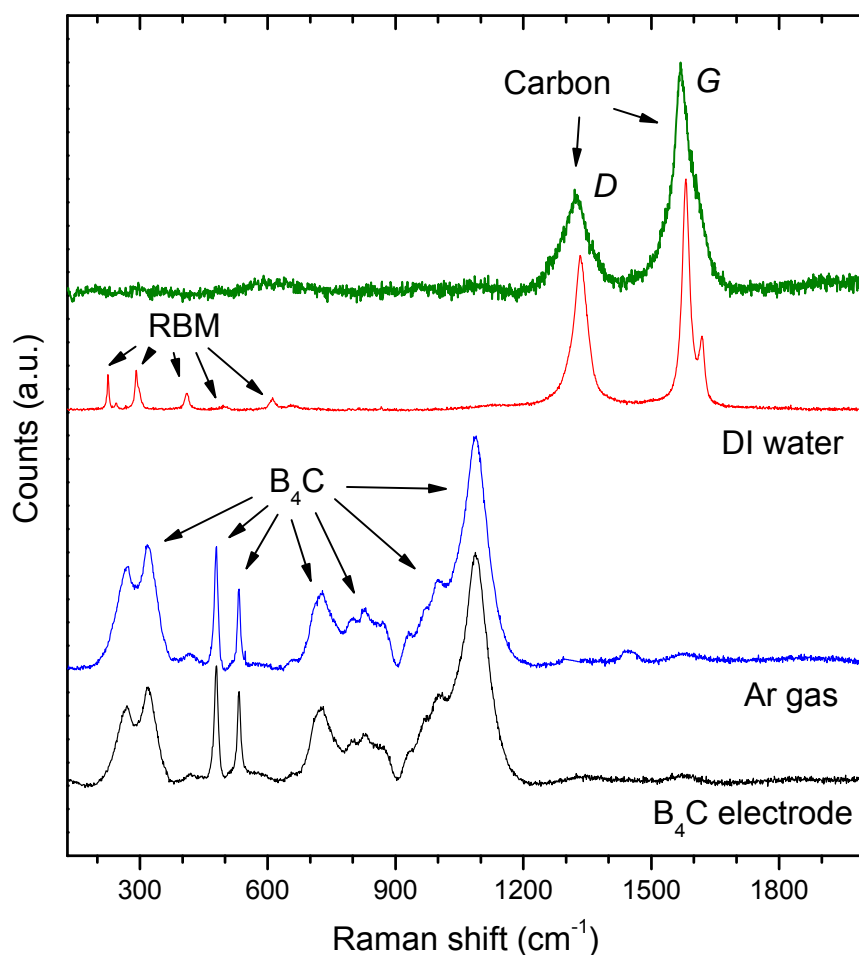


Figure 5.11. Raman spectra of boron carbide soot obtained by arc discharge between two B₄C electrodes submerged in DI water (red and green lines) and Ar gas (blue line). The spectrum of a B₄C electrode is also shown for reference (black line). Inset shows an optical image of the soot for a DI water submerged experiment.

Finally, boron carbide was created during the arc discharge between B_4C solid electrodes submerged in inert Ar gas. In this case, no contaminants or carbon nanotubes were found during the Raman analysis (Fig. 5.11). However two main problems must be addressed: during this experiment, the arc was very unstable and the electrodes were seriously damaged breaking apart; the produced soot was difficult to collect because the reactor was not sealed and the produced powder was very volatile in air. In conclusion, arc discharge between B_4C submerged in Ar gas seems to be a promising method but many implementations for the reactor need to be considered such as regular shape of electrodes, automatic drive system to move and control electrodes position, a sealed recipient and an efficient cooling system.

CHAPTER 6

CONCLUSION AND FUTURE WORK

In the first part of this study, the use of SWNT thin films as substrate for osteoblast cells growth has been explored. A dynamic interaction between SWNT bundles and living cells was observed during a long exposure time (31 days of implantation). *In situ* micro-Raman analysis showed a significant increase in $I(D)/I(G)$ intensity ratio of SWNT films used for cell implantation, as the exposure time increased. This indicates a higher disorder in the structure of the SWNT, such as introduction of defects, vacancies or bending of the tubes due to the cell/biological media mechanical and/or chemical interaction. Conductivity measurements were carried out on SWNT thin films before and after cells culture. Sheet resistance values were found to increase with the exposure time confirming a mechanism of cell-induced disorder, in agreement with the results of Raman spectroscopy. The possibility of a selective destruction of either metallic or semiconducting SWNTs was excluded because Raman data did not show any change in the RBM vibrational modes. Conversely, FTIR analysis revealed the presence of new absorption bands for the SWNTs exposed to the cells, probably associated with the substitution of benzene rings, formation of new covalent bonds and adsorption of CO on the SWNT surface indicating that a covalent functionalization of the SWNTs has occurred.

High resolution TEM images confirmed the destructive action of living cells on the SWNTs. The walls of the SWNT bundles already after 15 days of cell exposure appeared much damaged. Destruction and covalent functionalization of SWNTs by

biological cells/biological media system are two valid routes to reduce the risk of cytotoxicity during cell implantation. In conclusion, this study reports valuable basic information on the interaction of living osteoblast cells and SWNT bundles suggesting a dynamic mechanism of cell induced-disorder and chemical functionalization which could eventually lead to the total biodegradation of SWNTs and safe utilization in tissue-engineering bioapplications.

In the second part of this study the successful deposition of high quality Si free and Si doped amorphous boron carbide films was demonstrated. The α -BC and Si:BC thin films obtained using the sputtering configuration belonging to University of Coimbra address many scientific applications. Amorphous BC films offer more advantages than crystalline BC structures in terms of flexibility and wide range of applicability. For example, morphologically uniform and chemically homogeneous BC and BC:Si films allow post-deposition annealing treatment with the advantage of controlling crystallization and achieving specific desired physical properties. Also, it is possible to use amorphous BC films as tunable substrates for promoting the epitaxial growth of other crystals. While structural and mechanical characterization of the amorphous boron carbide films has been already discussed in our previous experimental section (Chapter 4), a detailed study of optical and electronic properties of the sputtered films is needed. We suggest addressing this goal by additional ellipsometry and photoluminescence investigation.

The unwanted formation of boric acid and boron oxide during the deposition at high temperature does not find technical applications at the moment. However, the sputtered films can be still used for fundamental studies. For example, special attention

was given to the change in structural and electronic properties of carbon doped β -rhombohedral boron [223]; we could attempt to dope and anneal in furnace our boron rich films with carbon and observe by Raman spectroscopy any structural changes that might occur. It would be interesting to correlate the structural and electronic changes with the substitution of carbon atoms for boron sites.

Finally, novel nanostructures of boron carbide (nominally B_4C) were synthesized using the submerged arc discharge method [213, 215, 217]. The discharge in liquid nitrogen was created between two graphite electrodes, one of which (the anode) was filled with microscopic boron carbide. Scanning electron microscopy studies revealed a wealth of novel nanoarchitectures such as nanowires, nanorods, spherical nanoparticles, and ribbon-like structures in the as-fabricated material. Transmission electron microscopy, Raman and infrared spectroscopy analyses confirmed that the detected nanostructures are comprised of boron carbide. A method based on specific gravity of the different nanostructures has been developed to self-separate the various types of nanostructures. As future work, a study of the electronic properties of these different boron carbide nanostructures by conductivity, photoluminescence, and thermal conductance measurements, could open new routes to novel applications.

BIBLIOGRAPHY

1. Pierson HO. Handbook of carbon, graphite, diamond, and fullerenes: Properties, processing and applications. Park Ridge: Noyes Publications, 1993.
2. Bethune DS, Klang CH, de Vries MS, Gorman G, Savoy R, Vazquez J, Beyers R. Cobalt-catalysed growth of carbon nanotubes with single-atomic-layer walls. *Nature* 1993;363:605.
3. Iijima S, Ichihashi T. Single-shell carbon nanotubes of 1-nm diameter. *Nature* 1993;363:603.
4. Han J. Structures and properties of carbon nanotubes. In: Meyyappan M, editor. Carbon nanotubes: Science and applications. New York: CRC Press, 2005. p.1.
5. Iijima S. Helical microtubules of graphitic carbon. *Nature* 1991;354:56.
6. Dresselhaus M, Dresselhaus G, Eklund P. Science of fullerenes and carbon nanotubes. San Diego: Academic Press, 1996.
7. Iijima S, Ichihashi T, Ando Y. Pentagons, heptagons and negative curvature in graphite microtubule growth. *Nature* 1992;356:776.
8. Satishkumar BC, John Thomas P, Govindaraj A, Rao CNR. Y-junction carbon nanotubes. *Applied Physics Letters* 2000;77:2530.
9. Zhong DY, Liu S, Wang EG. Patterned growth of coiled carbon nanotubes by a template-assisted technique. *Applied Physics Letters* 2003;83:4423.
10. Kim P, Odom TW, Huang J-L, Lieber CM. Electronic density of states of atomically resolved single-walled carbon nanotubes: Van Hove singularities and end states. *Physical Review Letters* 1999;82:1225.
11. Han J, Anantram MP, Jaffe RL, Kong J, Dai H. Observation and modeling of single-wall carbon nanotube bend junctions. *Physical Review B* 1998;57:14983.
12. Liu J, Dai H, Hafner JH, Colbert DT, Smalley RE, Tans SJ, Dekker C. Fullerene 'crop circles'. *Nature* 1997;385:780.
13. Hamada N, Sawada S-i, Oshiyama A. New one-dimensional conductors: Graphitic microtubules. *Physical Review Letters* 1992;68:1579.
14. Saito R, Fujita M, Dresselhaus G, Dresselhaus MS. Electronic structure of graphene tubules based on C60. *Physical Review B* 1992;46:1804.
15. Tanaka K, Okada M, Huang Y. Electronic structure of single-walled carbon nanotubes. In: Tanaka K, Yamabe T, Fukui K, editors. The science and technology of carbon nanotubes. New York: Elsevier, 1999. p.40.
16. Delaney P, Joon Choi H, Ihm J, Louie SG, Cohen ML. Broken symmetry and pseudogaps in ropes of carbon nanotubes. *Physical Review B* 1999;60:7899.
17. Ouyang M, Huang J-L, Cheung CL, Lieber CM. Energy gaps in "metallic" single-walled carbon nanotubes. *Science* 2001;27:702.
18. White CT, Robertson DH, Mintmire JW. Helical and rotational symmetries of nanoscale graphitic tubules. *Physical Review B* 1993;47:5485.
19. Yorikawa H, Muramatsu S. Electronic properties of semiconducting graphitic microtubules. *Physical Review B* 1994;50:12203.
20. Dai H, Wong EW, Lieber CM. Probing electrical transport in nanomaterials: Conductivity of individual carbon nanotubes *Science* 1996;272:523.

21. Soh HT, Quate CF, Morpurgo AF, Marcus CM, Kong J, Dai HJ. Integrated nanotube circuits: Controlled growth and ohmic contacting of single-walled carbon nanotubes. *Applied Physics Letters* 1999;75:627.
22. Hagen A, Hertel T. Quantitative analysis of optical spectra from individual single-wall carbon nanotubes. *Nano Letters* 2003;3:383.
23. Rao AM, Richter E, Bandow S, Chase B, Eklund PC, Williams KA, Fang S, Subbaswamy KR, Menon M, Thess A, Smalley RE, Dresselhaus G, Dresselhaus MS. Diameter-selective Raman scattering from vibrational modes in carbon nanotubes. *Science* 1997;275:187.
24. Saito R, Takeya T, Kimura T, Dresselhaus G, Dresselhaus MS. Raman intensity of single-wall carbon nanotubes. *Physical Review B* 1998;57:4145.
25. Saito R, Dresselhaus G, Dresselhaus MS. Phonon structure and Raman effect of single-walled carbon nanotubes. In: Tanaka K, Yamabe T, Fukui K, editors. *The science and technology of carbon nanotubes*. New York: Elsevier, 1999. p.51.
26. Alon OE. Number of Raman- and infrared-active vibrations in single-walled carbon nanotubes. *Physical Review B* 2001;63:201403.
27. Damen TC, Porto SPS, Tell B. Raman effect in zinc oxide. *Physical Review* 1966;142:570.
28. Popov VN, Lambin P. Vibrational and related properties of carbon nanotubes. In: Popov VN, Lambin P, editors. *Carbon nanotubes*. Amsterdam: Springer Netherlands, 2006. p.69.
29. Poncharal P, Wang ZL, Ugarte D, de Heer WA. Electrostatic deflections and electromechanical resonances of carbon nanotubes. *Science* 1999;283:1513.
30. Treacy MMJ, Ebbesen TW, Gibson JM. Exceptionally high Young's modulus observed for individual carbon nanotubes. *Nature* 1996;381:678.
31. Wong EW, Sheehan PE, Lieber CM. Nanobeam mechanics: Elasticity, strength, and toughness of nanorods and nanotubes. *Science* 1997;277:1971.
32. Lu JP, Han J. Carbon nanotubes and nanotube-based nano devices *International Journal of High Speed Electronics and Systems* 1998;9:101.
33. Hone J, Batlogg B, Benes Z, Johnson AT, Fischer JE. Quantized phonon spectrum of single-wall carbon nanotubes. *Science* 2000;289:1730.
34. Yi W, Lu L, Dian-lin Z, Pan ZW, Xie SS. Linear specific heat of carbon nanotubes. *Physical Review B* 1999;59:R9015.
35. Hone J, Whitney M, Piskoti C, Zettl A. Thermal conductivity of single-walled carbon nanotubes. *Physical Review B* 1999;59:R2514.
36. Ajayan PM, Ebbesen TW, Ichihashi T, Iijima S, Tanigaki K, Hiura H. Opening carbon nanotubes with oxygen and implications for filling. *Nature* 1993;362:522.
37. Hiura H, Ebbesen TW, Tanigaki K. Opening and purification of carbon nanotubes in high yields. *Advanced Materials* 1995;7:275.
38. Tsang SC, Chen YK, Harris PJF, Green MLH. A simple chemical method of opening and filling carbon nanotubes. *Nature* 1994;372:159.
39. Ajayan PM, Stephan O, Redlich P, Colliex C. Carbon nanotubes as removable templates for metal-oxide nanocomposites and nanostructures. *Nature* 1995;375:564.
40. Dujardin E, Ebbesen TW, Hiura H, Tanigaki K. Capillarity and wetting of carbon nanotubes. *Science* 1994;265:1850.

41. Ugarte D, Chatelain A, deHeer WA. Nanocapillarity and chemistry in carbon nanotubes. *Science* 1996;274:1897.
42. Kruger M, Widmer I, Nussbaumer T, Buitelaar M, Schonenberger C. Sensitivity of single multiwalled carbon nanotubes to the environment. *New J. Phys.* 2003;5:11.
43. Zhao JJ, Buldum A, Han J, Lu JP. Gas molecule adsorption in carbon nanotubes and nanotube bundles. *Nanotechnology* 2002;13:195.
44. Zhao JJ, Lu JP, Han J, Yang CK. Noncovalent functionalization of carbon nanotubes by aromatic organic molecules. *Applied Physics Letters* 2003;82:3746.
45. Frackowiak E, Gautier S, Gaucher H, Bonnamy S, Beguin F. Electrochemical storage of lithium multiwalled carbon nanotubes. *Carbon* 1999;37:61.
46. Liu XL, Lee C, Zhou CW, Han J. Carbon nanotube field-effect inverters. *Applied Physics Letters* 2001;79:3329.
47. Wu GT, Wang CS, Zhang XB, Yang HS, Qi ZF, He PM, Li WZ. Structure and lithium insertion properties of carbon nanotubes. *J. Electrochem. Soc.* 1999;146:1696.
48. Meyyappan M, editor *Carbon nanotubes: Science and applications*. New York: CRC Press, 2005.
49. Jiang KL, Li QQ, Fan SS. Nanotechnology: Spinning continuous carbon nanotube yarns - Carbon nanotubes weave their way into a range of imaginative macroscopic applications. *Nature* 2002;419:801.
50. Benoit JM, Corraze B, Lefrant S, Blau WJ, Bernier P, Chauvet O. Transport properties of PMMA-carbon nanotubes composites. *Synthetic Metals* 2001;121:1215.
51. Park C, Ounaies Z, Watson KA, Crooks RE, Smith J, Lowther SE, Connell JW, Siochi EJ, Harrison JS, Clair TLS. Dispersion of single wall carbon nanotubes by in situ polymerization under sonication. *Chemical Physics Letters* 2002;364:303.
52. Sandler J, Shaffer MSP, Prasse T, Bauhofer W, Schulte K, Windle AH. Development of a dispersion process for carbon nanotubes in an epoxy matrix and the resulting electrical properties. *Polymer* 1999;40:5967.
53. Cooper CA, Ravich D, Lips D, Mayer J, Wagner HD. Distribution and alignment of carbon nanotubes and nanofibrils in a polymer matrix. *Composites Science and Technology* 2002;62:1105.
54. Haggemueller R, Zhou W, Fischer JE, Winey KI. Production and characterization of polymer nanocomposites with highly aligned single-walled carbon nanotubes. *Journal of Nanoscience and Nanotechnology* 2003;3:105.
55. Harrison BS, Atala A. Carbon nanotube applications for tissue engineering. *Biomaterials* 2007;28:344.
56. Heller DA, Baik S, Eurell TE, Strano MS. Single-walled carbon nanotube spectroscopy in live cells: Towards long-term labels and optical sensors. *Advanced Materials* 2005;17:2793.
57. Cherukuri P, Bachilo SM, Litovsky SH, Weisman RB. Near-infrared fluorescence microscopy of single-walled carbon nanotubes in phagocytic cells. *Journal of the American Chemical Society* 2004;126:15638.
58. Shi DL, J; Wang, W; Liu, GK; He, P; Dong, ZY. Luminescent carbon nanotubes by surface functionalization. *Adv. Mater.* 2006;18:189.

59. Joseph SM, RJ; Jakobsson, E; Aluru, NR. Electrolytic transport in modified carbon nanotubes. *Nano Lett* 2003;3:1399.
60. Martin CKP. The emerging field of nanotube biotechnology. *Nat Rev Drug Discov* 2003;2:29.
61. Wang S-FS, L; Zhang, W-D; Tong Y-J. Preparation and mechanical properties of chitosan/carbon nanotubes composites. *Biomacromolecules* 2005:3067.
62. Correa-Duarte MW, N; Rojas-Chapana, J; Morsczeck, C; Thie, M; Giersig, M. Fabrication and biocompatibility of carbon nanotube-based 3D networks as scaffolds for cell seeding and growth. *Nano Lett* 2004;4:2233.
63. Supronowicz PA, PM; Ullmann, KR; Arulanandam, BP; Metzger, DW; Bizios, R. Novel current-conducting composite substrates for exposing osteoblasts to alternating current stimulation. *J Biomed Mater Res* 2002;59:499.
64. Gabay TJ, E; Ben-Jacob, E; Hanein Y. Engineered selforganization of neural networks using carbon nanotube clusters. *Physica A* 2005;250:611.
65. Ding LS, J; Zhang, T; Elboudwarej, O; Jiang, H; Selegue, JP. Molecular characterization of the cytotoxic mechanism of multiwall carbon nanotubes and nano-onions on human skin fibroblast. *Nano Lett* 2005;5:2448.
66. Nel A, Xia T, Madler L, Li N. Toxic potential of materials at the nanolevel. *Science* 2006;311:622.
67. MacDonald RL, BF; Viswanathan, G; Ajayan, PM; Stegemann, JP. Collagen-carbon nanotube composite materials as scaffolds in tissue engineering. *J Biomed Mater Res* 2005;74A:489.
68. Reynolds CA, N; Beshah, K; Huber, JH; Shaber, SH; Lenkinski, RE. Gadolinium-loaded nanoparticles: new contrast agents for magnetic resonance imaging. *J Am Chem Soc* 2000;122:8940.
69. Kagan VK, Konduru NV, Feng W, Allen BL, Conroy J, Volkov Y, Vlasova V, Belikova NA, Yanamala N, Kapralov A, Tyurina Y, Shi T, Kisin E, Murray AR, Franks J, Stolz D, Gou P, Seetharaman JK, Fadeel B, Star A, Shvedova AA. Carbon nanotubes degraded by neutrophil myeloperoxidase induce less pulmonary inflammation. *Nature Nanotechnology* 2010;5:354.
70. Collins PG, Zettl A, Bando H, Thess A, Smalley RE. Nanotube nanodevice. *Science* 1997;278:100.
71. Odom TW, Huang JL, Kim P, Lieber CM. Structure and electronic properties of carbon nanotubes. *Journal of Physical Chemistry B* 2000;104:2794.
72. Baugman RH. *Science* 1990:1340.
73. Dalton AB, Collins S, Munoz E, Razal JM, Ebron VH, Ferraris JP, Coleman JN, Kim BG, Baughman RH. Super-tough carbon-nanotube fibres - These extraordinary composite fibres can be woven into electronic textiles. *Nature* 2003;423:703.
74. Yu MF, Files BS, Arepalli S, Ruoff RS. Tensile loading of ropes of single wall carbon nanotubes and their mechanical properties. *Physical Review Letters* 2000;84:5552.
75. Bockrath M, Cobden DH, McEuen PL, Chopra NG, Zettl A, Thess A, Smalley RE. Single-electron transport in ropes of carbon nanotubes. *Science* 1997;275:1922.

76. Tans SJ, Devoret MH, Dai HJ, Thess A, Smalley RE, Geerligs LJ, Dekker C. Individual single-wall carbon nanotubes as quantum wires. *Nature* 1997;386:474.
77. Martel R, Schmidt T, Shea HR, Hertel T, Avouris P. Single- and multi-wall carbon nanotube field-effect transistors. *Applied Physics Letters* 1998;73:2447.
78. Tans SJ, Devoret MH, Groeneveld RJA, Dekker C. Electron-electron correlations in carbon nanotubes. *Nature* 1998;394:761.
79. Dekker C. Carbon nanotubes as molecular quantum wires. *Physics Today* 1999;52:22.
80. Tombler TW, Zhou CW, Alexseyev L, Kong J, Dai HJ, Lei L, Jayanthi CS, Tang MJ, Wu SY. Reversible electromechanical characteristics of carbon nanotubes under local-probe manipulation. *Nature* 2000;405:769.
81. Cao Q, Rogers JA. Ultrathin films of single-walled carbon nanotubes for electronics and sensors: A review of fundamental and applied aspects. *Advanced Materials* 2009;21:29.
82. Hwang ES, Cao CF, Hong SH, Jung HJ, Cha CY, Choi JB, Kim YJ, Baik S. The DNA hybridization assay using single-walled carbon nanotubes as ultrasensitive, long-term optical labels. *Nanotechnology* 2006;17:3442.
83. Krishna CM, Sockalingum GD, Kegelaar G, Rubin S, Kartha VB, Manfait M. Micro-Raman spectroscopy of mixed cancer cell populations. *Vibrational Spectroscopy* 2005;38:95.
84. Nottingher I. Raman Spectroscopy cell-based Biosensors. *Sensors* 2007;7:1343.
85. Hu H, Ni YC, Montana V, Haddon RC, Parpura V. Chemically functionalized carbon nanotubes as substrates for neuronal growth. *Nano Letters* 2004;4:507.
86. Kalbacova M, Kalbac M, Dunsch L, Kataura H, Hempel U. The study of the interaction of human mesenchymal stem cells and monocytes/macrophages with single-walled carbon nanotube films. *Physica Status Solidi B-Basic Solid State Physics* 2006;243:3514.
87. Usui Y, Aoki K, Narita N, Murakami N, Nakamura I, Nakamura K, Ishigaki N, Yamazaki H, Horiuchi H, Kato H, Taruta S, Kim YA, Endo M, Saito N. Carbon nanotubes with high bone-tissue compatibility and bone-formation acceleration effects. *Small* 2008;4:240.
88. Manna SK, Sarkar S, Barr J, Wise K, Barrera EV, Jejelowo O, Rice-Ficht AC, Ramesh GT. Single-walled carbon nanotube induces oxidative stress and activates nuclear transcription factor-kappa B in human keratinocytes. *Nano Letters* 2005;5:1676.
89. Yehia H, Draper R, Mikoryak C, Walker EK, Bajaj P, Musselman IH, Daigrepont M, Dieckmann GR, Pantano P. Single-walled carbon nanotube interactions with HeLa cells. *Journal of Nanobiotechnology* 2007;5.
90. Zhang D, Yi C, Zhang J, Chen Y, Yao X, Yang M. Effects of carbon nanotubes on the proliferation and differentiation of primary osteoblasts. *Nanotechnology* 2007;18:475102.
91. Baibarac M, Baltog I, Lefrant S, Mevellec JY, Bucur C. Vibrational and photoluminescence properties of the polystyrene functionalized single-walled carbon nanotubes. *Diamond and Related Materials* 2008;17:1380.
92. Duclaux L. Review of the doping of carbon nanotubes (multiwalled and single-walled). *Carbon* 2002;40:1751.

93. Chen MW, McCauley JW, Hemker KJ. Shock-induced localized amorphization in boron carbide. *Science* 2003;299:1563.
94. Eom JY, Kwon HS, Liu J, Zhou O. Lithium insertion into purified and etched multi-walled carbon nanotubes synthesized on supported catalysts by thermal CVD. *Carbon* 2004;42:2589.
95. Chen G, Furtado CA, Kim UJ, Eklund PC. Alkali-metal-doping dynamics and anomalous lattice contraction of individual debundled carbon nanotubes. *Physical Review B* 2005;72.
96. Maurin G, Bousquet C, Henn F, Bernier P, Almairac R, Simon B. Electrochemical lithium intercalation into multiwall carbon nanotubes: a micro-Raman study. *Solid State Ionics* 2000;136:1295.
97. Dresselhaus MS, Dresselhaus G, Jorio A, Souza AG, Saito R. Raman spectroscopy on isolated single wall carbon nanotubes. *Carbon* 2002;40:2043.
98. Dresselhaus MS, Dresselhaus G, Jorio A, Souza AG, Samsonidze GG, Saito R. Science and applications of single-nanotube Raman spectroscopy. *Journal of Nanoscience and Nanotechnology* 2003;3:19.
99. Bachilo SM, Strano MS, Kittrell C, Hauge RH, Smalley RE, Weisman RB. Structure-assigned optical spectra of single-walled carbon nanotubes. *Science* 2002;298:2361.
100. Hartschuh A, Pedrosa HN, Novotny L, Krauss TD. Simultaneous fluorescence and Raman scattering from single carbon nanotubes. *Science* 2003;301:1354.
101. Cronin SB, Swan AK, Unlu MS, Goldberg BB, Dresselhaus MS, Tinkham M. Measuring the uniaxial strain of individual single-wall carbon nanotubes: Resonance Raman spectra of atomic-force-microscope modified single-wall nanotubes. *Physical Review Letters* 2004;93.
102. Dillon AC, Yudasaka M, Dresselhaus MS. Employing Raman spectroscopy to qualitatively evaluate the purity of carbon single-wall nanotube materials. *Journal of Nanoscience and Nanotechnology* 2004;4:691.
103. Eda G, Fanchini G, Kanwal A, Chhowalla M. Bundling dynamics of single walled carbon nanotubes in aqueous suspensions. *Journal of Applied Physics* 2008;103.
104. Xu YQ, Peng HQ, Hauge RH, Smalley RE. Controlled multistep purification of single-walled carbon nanotubes. *Nano Letters* 2005;5:163.
105. Tutak W, Park KH, Vasilov A, Starovoytov V, Fanchini G, Cai SQ, Partridge NC, Sesti F, Chhowalla M. Toxicity induced enhanced extracellular matrix production in osteoblastic cells cultured on single-walled carbon nanotube networks. *Nanotechnology* 2009;20.
106. van der Pauw LJ. A method of measuring specific resistivity and Hall effect of discs of arbitrary shape. *Philips Res. Repts.* 1958;13:1.
107. Parekh BB, Fanchini G, Eda G, Chhowalla M. Improved conductivity of transparent single-wall carbon nanotube thin films via stable postdeposition functionalization. *Applied Physics Letters* 2007;90.
108. Baltog I, Baibarac M, Lefrant S, Mevellec JY. Raman and FTIR studies on electro-reduction of single-walled carbon nanotube films in the presence of Li salts. *Diamond and Related Materials* 2008;17:1558.

109. Charlier JC, Ebbesen TW, Lambin P. Structural and electronic properties of pentagon-heptagon pair defects in carbon nanotubes. *Physical Review B* 1996;53:11108.
110. Choi HJ, Ihm J, Louie SG, Cohen ML. Defects, quasibound states, and quantum conductance in metallic carbon nanotubes. *Physical Review Letters* 2000;84:2917.
111. McEuen PL, Bockrath M, Cobden DH, Yoon YG, Louie SG. Disorder, pseudospins, and backscattering in carbon nanotubes. *Physical Review Letters* 1999;83:5098.
112. Nardelli MB, Yakobson BI, Bernholc J. Mechanism of strain release in carbon nanotubes. *Physical Review B* 1998;57:R4277.
113. Zhang PH, Lammert PE, Crespi VH. Plastic deformations of carbon nanotubes. *Physical Review Letters* 1998;81:5346.
114. Bockrath M, Liang WJ, Bozovic D, Hafner JH, Lieber CM, Tinkham M, Park HK. Resonant electron scattering by defects in single-walled carbon nanotubes. *Science* 2001;291:283.
115. Bozovic D, Bockrath M, Hafner JH, Lieber CM, Park H, Tinkham M. Plastic deformations in mechanically strained single-walled carbon nanotubes. *Physical Review B* 2003;67.
116. Lambin P, Fonseca A, Vigneron JP, Nagy JB, Lucas AA. Structural and electronic-properties of bent carbon nanotubes. *Chemical Physics Letters* 1995;245:85.
117. Lambin P, Lucas AA, Charlier JC. Electronic properties of carbon nanotubes containing defects. *Journal of Physics and Chemistry of Solids* 1997;58:1833.
118. Rochefort A, Avouris P, Lesage F, Salahub DR. Electrical and mechanical properties of distorted carbon nanotubes. *Physical Review B* 1999;60:13824.
119. Nardelli MB, Yakobson BI, Bernholc J. Brittle and ductile behavior in carbon nanotubes. *Physical Review Letters* 1998;81:4656.
120. Furukawa H, Ajito K, Takahashi M, Ito M. SERS and FT-IR studies of co adsorbed on underpotential deposited ag/pt electrodes. *Journal of Electroanalytical Chemistry* 1990;280:415.
121. Kam NWS, Dai HJ. Carbon nanotubes as intracellular protein transporters: Generality and biological functionality. *Journal of the American Chemical Society* 2005;127:6021.
122. Lau KC, Yap YK, Pandey R. Boron and boron carbide materials: Nanostructures and crystalline solids In: Yap YK, editor. *B-C-N nanotubes and related nanostructures*, vol. 6. New York: Springer, 2009. p.271.
123. Dole SL, Prochazka S, Doremus RH. Microstructural coarsening during sintering of boron-carbide. *Journal of the American Ceramic Society* 1989;72:958.
124. Lipp A. Boron carbide: Production, properties, application. *Technische Rundschau* 1966;7:1.
125. Radev DD, Zakhariyev Z. Structural and mechanical properties of activated sintered boron carbide-based materials. *Journal of Solid State Chemistry* 1998;137:1.
126. Thevenot F. Boron carbide - a comprehensive review. *Journal of European Ceramic Society* 1990;6:205.

127. Aselage TL, Tissot RG. Lattice-constants of boron carbides. *Journal of the American Ceramic Society* 1992;75:2207.
128. Kuhlmann U, Werheit H, Schwetz KA. Distribution of carbon atoms on the boron carbide structure elements. *Journal of Alloys and Compounds* 1992;189:249.
129. Vast N, Lazzari R, Besson JM, Baroni S, Dal Corso A. Atomic structure and vibrational properties of icosahedral α -boron and B_4C boron carbide. *Computational Materials Science* 2000;17:127.
130. Cahn RWH, P.; Kramer, E. J. Boride and Carbide Ceramics. *Materials Science and Technology*;11.
131. Kuhlmann U, Werheit H. On the microstructure of boron carbide. *Solid state communications* 1992;83:849.
132. Bylander DM, Kleinman L, Lee S. Self-consistent calculations of the energy bands and bonding properties of $B_{12}C_3$. *Physical Review B* 1990;42:1394.
133. Mauri F, Vast N, Pickard CJ. Atomic structure of icosahedral B_4C boron carbide from a first principles analysis of NMR spectra. *Physical Review Letters* 2001;87.
134. Emin D. Structure and single-phase regime of boron carbides. *Physical Review B* 1988;38:6041.
135. Fanchini G, McCauley JW, Chhowalla M. Behavior of disordered boron carbide under stress. *Physical Review Letters* 2006;97:035502.
136. Thevenot F. Sintering of boron-carbide and boron carbide silicon carbide 2-phase materials and their properties. *Journal of Nuclear Materials* 1988;152:154.
137. Tallant DR, Aselage TL, Campbell AN, Emin D. Boron carbide structure by Raman spectroscopy. *Physical Review B* 1989;40:5649.
138. Aselage TL, Tallant DR, Emin D. Isotope dependencies of Raman spectra of $B_{12}As_2$, $B_{12}P_2$, $B_{12}O_2$, and $B_{12+x}C_{3-x}$: Bonding of intericosahedral chains. *Physical Review B* 1997;56:3122.
139. Kuhlmann U, Werheit H. Raman effect of boron carbide ($B_{4.3}C$ to $B_{10.37}C$). *Journal of Alloys and Compounds* 1994;205:87.
140. Werheit H, Rotter HW, Meyer FD, Hillebrecht H, Shalamberidze SO, Abzianidze TG, Esadze GG. FT-Raman spectra of isotope-enriched boron carbide. *Journal of Solid State Chemistry* 2004;177:569.
141. Domnich V, Gogotsi Y, Trenary M, Tanaka T. Nanoindentation and Raman spectroscopy studies of boron carbide single crystals. *Applied Physics Letters* 2002;81:3783.
142. Shirai K, Emura S. Lattice vibrations and the bonding nature of boron carbide. *Journal of Physics-Condensed Matter* 1996;8:10919.
143. Werheit H, Schmechel R, Kuhlmann U, Kampen TU, Monch W, Rau A. On the reliability of the Raman spectra of boron-rich solids. *Journal of Alloys and Compounds* 1999;291:28.
144. Tallant DR, Aselage TL, Campbell AN, Emin D. Boron carbides: Evidence for molecular level disorder. *Journal of Non-Crystalline Solids* 1988;106:370.
145. Kuhlmann U, Werheit H. Improved Raman effect studies on boron-carbide ($B_{4.3}C$). *Physica Status Solidi B-Basic Research* 1993;175:85.
146. Werheit H, Au T, Schmechel R, Shalamberidze SO, Kalandadze GI, Eristavi AM. IR-Active phonons and structure elements of isotope-enriched boron carbide. *Journal of Solid State Chemistry* 2000;154:79.

147. Werheit H, Leithe-Jasper A, Tanaka T, Rotter HW, Schwetz KA. Some properties of single-crystal boron carbide. *Journal of Solid State Chemistry* 2004;177:575.
148. Casiraghi C, Ferrari AC, Robertson J. Raman spectroscopy of hydrogenated amorphous carbons. *Physical Review B* 2005;72.
149. Lespade L, Al-Jishi R, Dresselhaus MS. Model for Raman scattering from incompletely graphitized carbons. *Carbon* 1982;20:427.
150. Ferrari AC, Robertson J. Interpretation of Raman spectra of disordered and amorphous carbon. *Physical Review B* 2000;61:14095.
151. Tuinstra F, Koenig JL. Raman spectrum of graphite. *Journal of Chemical Physics* 1970;53:1126.
152. Lagrenaudie J. A study of the properties of boron. *Journal de Physique et Le Radium* 1953;14:14.
153. Lee S, Mazurowski J, Ramseyer G, Dowben PA. Characterization of boron-carbide thin-films fabricated by plasma enhanced chemical vapor-deposition from boranes. *Journal of Applied Physics* 1992;72:4925.
154. Aselage TL, Emin D, McCready SS, Duncan RV. Large enhancement of boron carbides' seebeck coefficients through vibrational softening. *Physical Review Letters* 1998;81:2316.
155. Balakrishnarajan MM, Pancharatna PD, Hoffmann R. Structure and bonding in boron carbide: The invincibility of imperfections. *New Journal of Chemistry* 2007;31:473.
156. Werheit H. Are there bipolarons in icosahedral boron-rich solids? *Journal of Physics-Condensed Matter* 2007;19:186207.
157. Werheit HDG, K.; Malkemper, W. On the metal-insulator transition of boron carbide. *Journal of the Less-Common Metals* 1981;82:152.
158. Werheit H, Binnenbruck H, Hausen A. Optical properties of boron carbide and comparison with β -rhombohedral boron. *Physica Status Solidi (b)* 1971;47:153.
159. Werheit H, Laux M, Kuhlmann U, Telle R. Optical interband transitions of boron carbide. *Physica Status Solidi (b)* 1992;172:K81.
160. Schmechel R, Werheit H, Kampen TU, Mönch W. Photoluminescence of boron carbide. *Journal of Solid State Chemistry* 2004;177:566.
161. Werheit H. On excitons and other gap states in boron carbide. *Journal of Physics-Condensed Matter* 2006;18:10655.
162. Niihara KN, A.; Hirai, T. The effect of Stoichiometry on Mechanical Properties of Boron Carbide. *Communications of the American Ceramic Society* 1984.
163. Lee M, Yoo YH. Analysis of ceramic/metal armour systems. *International Journal of Impact Engineering* 2001;25:819.
164. Kim BN, Hiraga K, Morita K, Sakka Y. A high-strain-rate superplastic ceramic. *Nature* 2001;413:288.
165. McClellan KJ, Chu F, Roper JM, Shindo I. Room temperature single crystal elastic constants of boron carbide. *Journal of Materials Science* 2001;36:3403.
166. Lemis-Petropoulos P, Kapaklis V, Peikrishvili AB, Politis C. Characterization of B_4C and LaB_6 by ultrasonics and X-rays diffraction. *International Journal of Modern Physics B* 2003;17:2781.
167. Lee H, Speyer RF. Hardness and fracture toughness of pressureless-sintered boron carbide (B_4C). *Journal of the American Ceramic Society* 2002;85:1291.

168. Dandekar DP. Shock response of boron carbide. Aberdeen Proving Ground, Aberdeen, MD: Army Research Laboratory, 2001.
169. Grady DE. Shock-wave properties of high-strength ceramics. In: Schmidt SC, Dick RD, Forbes JW, Tasker DG, editors. Shock compression of condensed matter. Amsterdam: Elsevier Science, 1992. p.455.
170. Grady DE. Shock-wave compression of brittle solids. *Mechanics of Materials* 1998;29:181.
171. Vogler TJ, Reinhart WD, Chhabildas LC. Dynamic behavior of boron carbide. *Journal of Applied Physics* 2004;95:4173.
172. Rajendran AM, Grove DJ. Modeling the shock response of silicon carbide, boron carbide and titanium diboride. *International Journal of Impact Engineering* 1996;18:611.
173. Ge D, Domnich V, Juliano T, Stach EA, Gogotsi Y. Structural damage in boron carbide under contact loading. *Acta Materialia* 2004;52:3921.
174. Yan XQ, Li WJ, Goto T, Chen MW. Raman spectroscopy of pressure-induced amorphous boron carbide. *Applied Physics Letters* 2006;88:131905.
175. Chen M, McCauley JW. Mechanical scratching induced phase transitions and reactions of boron carbide. *Journal of Applied Physics* 2006;100:123517.
176. Ghosh D, Subhash G, Lee CH, Yap YK. Strain-induced formation of carbon and boron clusters in boron carbide during dynamic indentation. *Applied Physics Letters* 2007;91.
177. Yan XQ, Tang Z, Zhang L, Guo JJ, Jin CQ, Zhang Y, Goto T, McCauley JW, Chen MW. Depressurization amorphization of single-crystal boron carbide. *Physical Review Letters* 2009;102:075505.
178. Aydin S, Simsek M. Hypothetically superhard boron carbide structures with a B₁₁C icosahedron and three-atom chain. *Physica Status Solidi B-Basic Solid State Physics* 2009;246:62.
179. Ohring M. The materials science of thin films: Deposition and structure. San Diego: Academic Press, 2002.
180. Mattox DM. Handbook of Physical Vapor Deposition (PVD) Processing, Film Formation, Adhesion, Surface, Preparation and Contamination Control. Park Ridge: Noyes Publications, 1998.
181. Hoffmann DW. Perspectives on stress in magnetron-sputtered thin films. *Journal of Vacuum Science and Technology A* 1994;12:953.
182. Heinemann K, Poppa H. Nucleation, growth and post-deposition thermally induced of gold on sapphire. *Journal of Vacuum Science and Technology* 1979;16:622.
183. Vossen JL, Cuomo JJ. Glow discharge sputter deposition. In: Vossen JL, Kern W, editors. Thin film processes. New York: Academic Press, 1978. p.11.
184. Pendolf AS. Magnetron sputtering. In: Glocker DA, Shah SI, editors. Handbook of Thin Films Process Technology. New York: Institute of Physics Publishing, 1995.
185. Conde O, Silvestre AJ, Oliveira JC. Influence of carbon content on the crystallographic structure of boron carbide films. *Surface & Coatings Technology* 2000;125:141.

186. Ahn HS, Cuong PD, Shin KH, Lee KS. Tribological behavior of sputtered boron carbide coatings and the influence of processing gas. *Wear* 2005;259:807.
187. Cuong PD, Ahn HS, Yoon ES, Shin KH. Effects of relative humidity on tribological properties of boron carbide coating against steel. *Surface & Coatings Technology* 2006;201:4230.
188. Essafti A, Ech-chamikh E, Fierro JLG. Structural and chemical analysis of amorphous B-N-C thin films deposited by RF sputtering. *Diamond and Related Materials* 2005;14:1663.
189. Jacobsohn LG, Nastasi M. Sputter-deposited boron carbide films: structural and mechanical characterization. *Surface & Coatings Technology* 2005;200:1472.
190. Jacobsohn LG, Schulze RK, da Costa M, Nastasi M. X-ray photoelectron spectroscopy investigation of boron carbide films deposited by sputtering. *Surface Science* 2004;572:418.
191. Lattemann M, Ulrich S. Investigation of structure and mechanical properties of magnetron sputtered monolayer and multilayer coatings in the ternary system Si-B-C. *Surface & Coatings Technology* 2007;201:5564.
192. Liu YS, Cheng LF, Zhang LT, Yang WB, Xu YD. Effect of carbon precursors on the microstructure and bonding state of a boron-carbon compound grown by LPCVD. *International Journal of Applied Ceramic Technology* 2008;5:305.
193. Todorovi-Markovic B, Draganic I, Vasiljevic-Radovic D, Romcevic N, Romcevic M, Dramicanin M, Markovic Z. Synthesis of amorphous boron carbide by single and multiple charged boron ions bombardment of fullerene thin films. *Applied Surface Science* 2007;253:4029.
194. Xu SM, X.; Mingren, S. Investigation of BCN films deposited at various N₂/Ar flow ratios by DC reactive magnetron sputtering. *IEEE Transaction on Plasma Science* 2006;34:1199.
195. Zhou MJ, Wong SF, Ong CW, Li Q. Microstructure and mechanical properties of B₄C films deposited by ion beam sputtering. *Thin Solid Films* 2007;516:336.
196. Kulikovskiy V, Vorlicek V, Bohac R, Ctvrtlik R, Stranyanek M, Dejneka A, Jastrabik L. Mechanical properties and structure of amorphous and crystalline B₄C films. *Diamond and Related Materials* 2009;18:27.
197. Lannin JF, Messier R. Low-frequency modes in amorphous boron-rich alloys. *Physical Review Letters* 1980;45:1119.
198. Essafti A, Ech-chamikh E, Azizan M. Structural and chemical study of a-BC, a-CN and a-BCN Thin films prepared by reactive RF sputtering. *Spectroscopy Letters* 2007;63:41:57.
199. Louro C, Oliveira JC, Chhowalla M, Cavaleiro A. Silicon effect on the hardness of RF sputtered B-C:Si amorphous films. *Plasma Processes and Polymers* 2009;6.
200. Anguita JV. IR absorption studies of a-C thin films. In: Silva SRP, editor. *Properties of Amorphous Carbon* vol. 29. London: INSPEC, 2001. p.128.
201. Thamaphat K, Limsuwan P, Ngotawornchai B. Phase characterization of TiO₂ powder by XRD and TEM. *Kasetsart Journal (Natural Sciences)* 2008;42.
202. Li ZQ, Lu CJ, Xia ZP, Zhou Y, Luo Z. X-ray diffraction patterns of graphite and turbostratic carbon. *Carbon* 2007;45:1686.

203. Aselage TL, Tallant DR. Association of broad icosahedral Raman bands with substitutional disorder in SiB_3 and boron carbide. *Physical Review B* 1998;57:2675.
204. Wu ML, Kiely JD, Klemmer T, Hsia YT, Howard K. Process-property relationship of boron carbide thin films by magnetron sputtering. *Thin Solid Films* 2004;449:120.
205. Lavrenko VA, Pomytkin AP, Kislyi PS, Grabchuk BL. Kinetics of high-temperature oxidation of boron carbide in oxygen. *Oxidation of Metals* 1976;10:85.
206. Lavrenko VA, Gogotsi YG. Influence of oxidation on the composition and structure of the surface layer of hot-pressed boron carbide. *Oxidation of Metals* 1988;29:193.
207. Arenal R, Ferrari AC, Reich S, Wirtz L, Mevellec JY, Lefrant S, Rubio A, Loiseau A. Raman spectroscopy of single-wall boron nitride nanotubes. *Nano Letters* 2006;6:1812.
208. Hoyaux MF. *Arc physics*. New York: Springer-Verlag, 1968.
209. Risacher A, Larigaldie S, Bobillot G, Marcellin JP, Picard L. Active stabilization of low-current arc discharges in atmospheric-pressure air. *Plasma Sources Science & Technology* 2007;16:200.
210. Saha MN. On a physical theory of stellar spectra. *Proceedings of the Royal Society of London. Series A, Containing Papers of a Mathematical and Physical Character* 1921;99:135.
211. Child CD. *Electric arcs*. New York: D. Van Nostrand Company, 1913.
212. Ishigami M, Cumings J, Zettl A, Chen S. A simple method for the continuous production of carbon nanotubes. *Chemical Physics Letters* 2000;319:457.
213. Sano N, Charinpanitkul T, Kanki T, Tanthapanichakoon W. Controlled synthesis of carbon nanoparticles by arc in water method with forced convective jet. *Journal of Applied Physics* 2004;96:645.
214. Sano N, Wang H, Alexandrou I, Chhowalla M, Teo KBK, Amaratunga GAJ, Iimura K. Properties of carbon onions produced by an arc discharge in water. *Journal of Applied Physics* 2002;92:2783.
215. Sano N, Wang H, Chhowalla M, Alexandrou I, Amaratunga GAJ. Nanotechnology - Synthesis of carbon 'onions' in water. *Nature* 2001;414:506.
216. Gattia DM, Antisari MV, Marazzi R. AC arc discharge synthesis of single-walled nanohorns and highly convoluted graphene sheets. *Nanotechnology* 2007;18.
217. Wang H, Chhowalla M, Sano N, Jia S, Amaratunga GAJ. Large-scale synthesis of single-walled carbon nanohorns by submerged arc. *Nanotechnology* 2004;15:546.
218. Yao MG, Liu BB, Zou YG, Wang L, Li DM, Cui T, Zou GT, Sundqvist B. Synthesis of single-wall carbon nanotubes and long nanotube ribbons with Ho/Ni as catalyst by arc discharge. *Carbon* 2005;43:2894.
219. Kim SRG, V.; Yim, SW.; Chhowalla, M. Transparent and thermally conducting nanocomposites from ultra long boron carbide NWs and PMMA. *Nature Nanotechnology* under revision.
220. Sano N, Wang HL, Chhowalla M, Alexandrou I, Amaratunga GAJ, Naito M, Kanki T. Fabrication of inorganic molybdenum disulfide fullerenes by arc in water. *Chemical Physics Letters* 2003;368:331.

221. Sano N, Naito M, Chhowalla M, Kikuchi T, Matsuda S, Iimura K, Wang HL, Kanki T, Amaratunga GAJ. Pressure effects on nanotubes formation using the submerged arc in water method. *Chemical Physics Letters* 2003;378:29.
222. Dash RK, Nikitin A, Gogotsi Y. Microporous carbon derived from boron carbide. *Microporous and Mesoporous Materials* 2004;72:203.
223. Werheit H, Kuhlmann U, Laux M, Lundstrom T. Structural and electronic properties of carbon-doped beta-rhombohedral boron. *Physica Status Solidi (b)* 1993;179:489.

CURRICULUM VITAE

Sara Reynaud

EDUCATION

- 2000-2003 B.S., Materials Science and Engineering, University of Naples “Federico II”, Naples, Italy
- 2003-2005 M.S., Materials Science and Engineering, University of Naples “Federico II”, Naples, Italy
- 2007-2010 Ph.D., Materials Science and Engineering, Rutgers University, New Brunswick, New Jersey

PROFESSIONAL EXPERIENCE

- 2005 Lab Technician, Colmegna Sud srl., Caserta, Italy
- 2006-2007 Lab Technician / Researcher, Analytical and Systems Department, Arkema Inc., King of Prussia, Pennsylvania
- 2007-2010 Graduate Research Assistant, Department of Materials Science and Engineering, Rutgers University, New Brunswick, New Jersey

PUBLICATIONS

1. S. Caserta, S. Reynaud, M. Simeone, S. Guido, Drop Deformation in Sheared Polymer Blends (*Journal of Rheology* **51**, 4:761, 2007).
2. N. Mekhilef, S. Reynaud, L. Hedhli, G. Pasquariello, Polyvinylidene Fluoride Containing Long Chain Branching for Blown Film Applications (*ANTEC*, Cincinnati, OH, 2007).
3. N. Mekhilef, L. Hedhli, S. Reynaud, G.O. Pasquariello, High Melt Strength Polyvinylidene Fluoride for Thermoforming Applications (*ANTEC*, Cincinnati, OH, 2007).
4. S. Reynaud, M. Evaristo, A. Cavaleiro, M. Chhowalla, Characterization of Amorphous BC Thin Films Fabricated by RF Sputtering (in preparation).
5. S. Reynaud, A. Avci, S. Miller, S. R. Kim, M. Chhowalla, Novel Boron Carbide Nanostructures by Arc-Discharge Method (in preparation).
6. S. Reynaud, W. Tutak, H. Yamaguchi, M. Chhowalla, Application of Carbon Nanotubes in Cellular Biochemistry: Investigation of the Effect of Cells on SWNTs (in preparation).